THE UNIVERSITY OF BIRMINGHAM

The Effect of Hydrogen on Palladium-Copper Based Membranes for Hydrogen Purification

James Raphael Warren

The Effect of Hydrogen on Palladium-Copper Membranes for Hydrogen Purification

Abstract

High purity hydrogen has several applications and is considered to be particularly important in hydrogen fuel cell technology for low carbon emissions. Palladium- based membranes are frequently used for the purification of hydrogen to >99.9999%. The current alloy most commonly used for industrial purification applications is palladium-silver. Shortcomings of this alloy include low strength and poor resistance to poisoning particularly from H_2S.

A possible solution to these problems is to use palladium-copper which also has reasonable permeability, particularly at 47 atomic% Pd. The Pd-Cu binary phase system has been studied thoroughly although the phase diagram is unclear particularly at low temperatures around the high permeability region. The ternary system of Pd-Cu-H, active in membranes, has several anomalies. In particular a shift in the phase boundary line towards the Pd-rich end at elevated pressures is noted in the literature although little work to comprehensively study this effect has been carried out. Variations between the solubility and diffusivity of f.c.c. and b.c.c. grains may also have an effect on the thermal cycling properties of the alloy ultimately leading to reduced selectivity over time. Hydrogen content through the material is thought to give a structural gradient which could strongly affect the material properties and the optimum membrane conditions during the purification process.

In the present work the effect of hydrogen on the phase balance and permeability is investigated. Initially the chemical composition and phase balance of three Pd-Cu alloys around high permeability region calculated using EDX and XRD with Topas software. Thermal cycling is then performed using in-situ XRD under both inert and hydrogenated conditions, with various overpressures. In-situ XRD results are compared with phase diagrams found in the literature. The effect of hydrogen pressure and pressure differential on the permeability of the alloy is ascertained using bespoke permeability equipment at the University of Birmingham. Where relevant, the results are compared to those found in the literature and the optimum conditions for permeability are discussed.

James Raphael Warren

Acknowledgements

I would firstly like to express my gratitude to Dr. Sean Fletcher, Dr. John Speight and Dr. David Book for their guidance and advice in undertaking this project.

Further thanks are extended to my colleagues in the Hydrogen Materials Group for their contributions during the project.

Finally, I would like to thank my family and friends, without your love and support I would not have been able to do this.

Contents

1 Introduction

1.1 The Industrial Applications of Hydrogen

Hydrogen is the most abundant element in the universe and its applications vary widely. Almost half of the hydrogen produced globally is used in the Haber process to produce ammonia (Joan Ogden). Ammonia is used as a fertiliser for agriculture; it can also be used as an industrial chemical itself as well as for the production of other useful chemicals (Joan Ogden).

The chemical and petrochemical industries use hydrogen for hydrodealkylation, hydrodesulfurization, and hydrocracking of crude oil (Joan Ogden). Hydrogen is used to upgrade the quality of viscous oil sources (Meyers). The demand for hydrogen for such processes is currently increasing due to more stringent global policies on fuel purity standards (US DoE).

Pure hydrogen is used in the chemical synthesis of other chemicals such as methanol, hydrochloric acid, hydrogen peroxide, polymers and solvents. Hydrogen is also used in the food industry for hydrogenation of fats and for manufacturing in the pharmaceutical industry (Wisegeek).

Metallurgical applications of hydrogen include its use as a reagent to reduce metal ores; in Fischer-Tropsch reactions (Nenoff). Alternatively it can be used as a shielding gas for welding and copper brazing, or as an inert gas for sintering or heat treatment of stainless steel alloys (Joan Ogden). The hydrogen disproportionation desorption recombination (HDDR) process, developed at the University of Birmingham, is used to produce magnetically coercive powder for permanent magnets (McGuiness). Hydrogen becomes liquid at a temperature of 14K, thus research into its use for superconductivity as a coolant is currently ongoing (Cambridge).

1.1.1 The Applications of High Purity Hydrogen

In economic terms the main driving force for high purity hydrogen production are the semiconductor and LED industries (Power and Energy). Semiconductor production requires high purity hydrogen for doping of silicon wafers (Job). Broken bonds of amorphous silicon and amorphous carbon are saturated by hydrogen gas, giving a more stable material and hence improved semiconductor properties (Spear). In addition, interstitial hydrogen also acts as an electron donor in several oxides used as high dielectric constant gate oxides (Peacock and Robertson). In each case the presence of trace impurities in the hydrogen gas stream will lead to contamination of the semiconductor material making it less stable and effective.

Legislation regarding reductions in carbon emissions and the need for non-fossil fuel based energy sources has brought fuel cell technology to the forefront of current scientific research. Proton Exchange Membrane (PEM) fuel cells operate at low temperatures (50-100 ºC) and offer efficiencies of up to 60% (Crawley). PEM fuel cells are considered by many as a possible replacement for petrol/diesel engines for vehicular applications primarily due to increased efficiency cleaner emissions (Züttel).

PEM fuel cells initially take a gas stream of hydrogen and catalytically split molecules into two protons and two electrons at the anode. Protons pass across an ionically conductive electrolyte while electrons flow around a circuit to the cathode. Protons reform with electrons as well as oxygen, from the air, giving an output of pure water and heat, Figure 1.1.

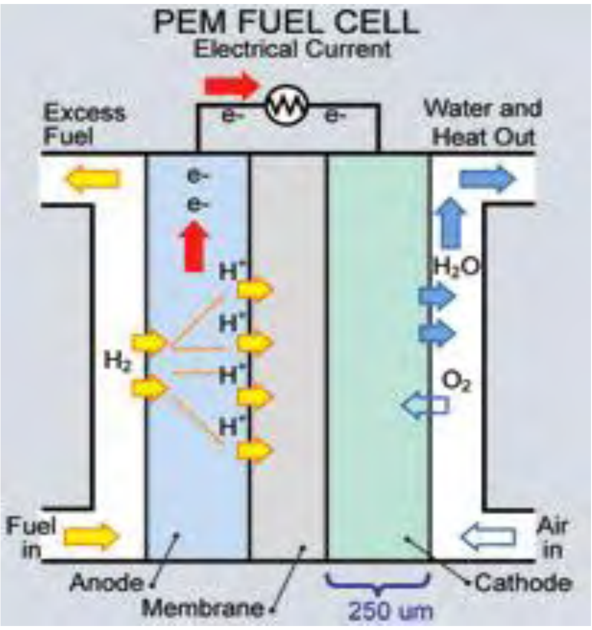

Figure 1.1 – A schematic diagram of a PEM fuel cell (SRNL).

Impurities of CO and sulphur based compounds, such as H_2S, in the hydrogen gas stream have been shown to poison the platinum catalyst at the anode and reduce the lifetime of the fuel cell (US DoE PEM).

2 Literature Review

2.1 Production of Hydrogen

Despite being more abundant than any other element in the universe, hydrogen does not often exist in molecular form (BOC). Pure hydrogen can be produced by many means, each of which has their own virtues and shortcomings. Two major sources of hydrogen, reviewed in this thesis, are reformation of hydrocarbons and electrolysis of water. Although reformation of hydrocarbons such as methane yields large quantities of hydrogen the reaction by-products include CO and CO_2 whereas hydrogen produced from water gives only oxygen as a by-product.

2.1.1 Steam Methane Reformation (SMR)

The current method by which 48% of world hydrogen and more than 95% of US hydrogen is produced is Steam Methane Reforming (SMR) shown in Figure 2.1.

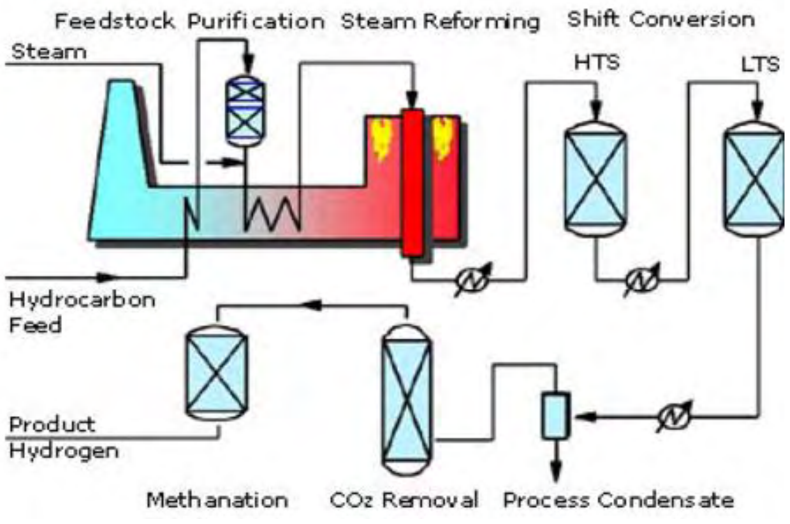

Figure 2.1 – The production of hydrogen via the SMR process (Design News)

The methane or natural gas source is purified in order to remove sulphur and chlorine which would poison catalysts used later in the process; reducing their lifetime (SMR DoE). Syngas, a mixture of hydrogen and carbon monoxide is produced by mixing steam with methane or natural gas at 800 ºC in the presence of a nickel catalyst; this process is called steam reformation Equation 2.1. After reformation the water gas shift reaction is carried out whereby carbon monoxide in the syngas mixture is reacted with remaining steam giving hydrogen and carbon dioxide Equation 2.2. Often there are two different shift reactions at 300 ºC and 200 ºC (SMR DoE). The carbon dioxide is removed giving a low-medium purity grade of hydrogen.

Reformation reaction

$$\mathbf{CH_4 + H_2O \rightarrow CO + 3H_2} \qquad \textbf{Equation 2.1}$$

Water Gas Shift reaction

$$\mathbf{CO + H_2O \rightarrow H_2 + CO_2} \qquad \textbf{Equation 2.2}$$

Efficiency of 65-75% is typical for this hydrogen production method (Book), as a large scale, established technology this technique is thought to have limited capacity for improvements in efficiency (Book).

2.1.2 Coal Gasification

Coal gasification is another hydrogen production process using fossil fuel sources, shown Figure 2.2. Coal is heated to 1800 ºC in air to give a syngas mixture of hydrogen, carbon monoxide and carbon dioxide with associated traces of sulphur, mercury and other environmentally damaging particulates (CG DoE).

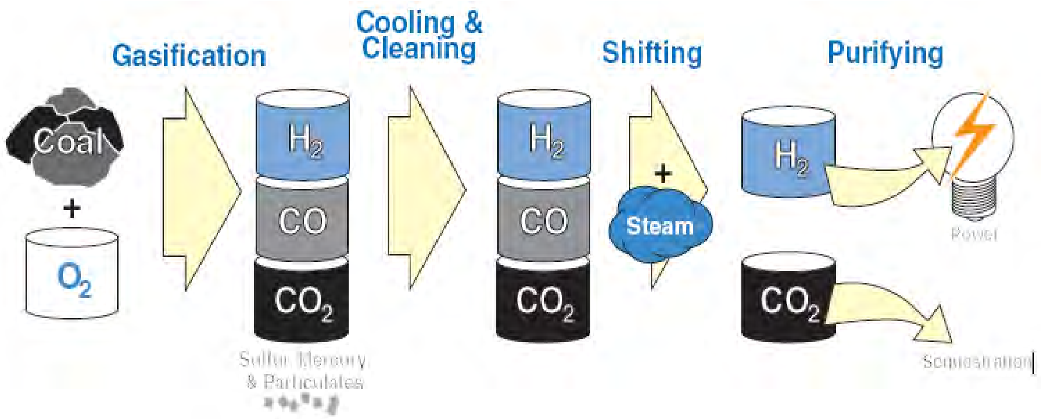

Figure 2.2 – The process of coal gasification to produce hydrogen (FCHEA).

The hot syngas is cooled and cleaned to remove the sulphur, mercury and other particulates which must be disposed of in an environmentally conscious manner. During the next step is a shift reaction, carbon monoxide reacts with steam to produce more hydrogen and carbon dioxide similar to SMR process in Equation 2.2. The carbon dioxide and hydrogen are separated for CCS and use as an energy carrier respectively. (Book)

2.1.3 Hydrogen Production from Water

A water molecule can be split into hydrogen and oxygen atoms using heat, light or electricity; hydrogen production from this method has high extremely high purity (S.S. Labs). If renewable energy sources were used to split water molecules and the hydrogen produced was used as an energy carrier, then the result of this would be a drastic reduction in carbon emissions

Hydrogen, produced from water, may be used as an energy source from which water itself is the only by-product; either by use of a PEM fuel cell or via combustion. The by-product of water could then be used to produce hydrogen; an energy cycle is now operational, as opposed to a linear process of energy consumption, Figure 2.3.

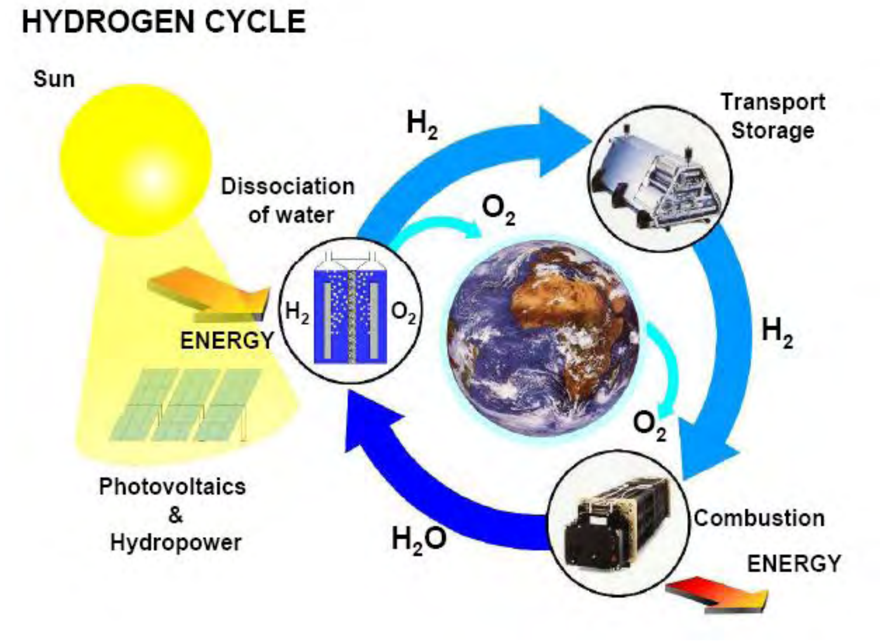

Figure 2.3 – The hydrogen energy cycle (Züttel)

2.1.3.1 Electrolysis of Water

An electric current is passed through water, which is distilled to reduce breakdown of the electrodes and catalysts. The water molecule is split into hydrogen and oxygen via the reactions shown in Equations 2.3, 2.4 and 2.5.

Anodic Reaction: $2H_2O \rightarrow O_2 + 4H^+ + 4e^-$ **Equation 2.3**

Cathodic Reaction: $4H^+ + 4e^- \rightarrow 2H_2$ **Equation 2.4**

Overall Reaction: $H_2O \rightarrow H_2 + 0.5O_2$ **Equation 2.5**

Electrodes are made of nickel or nickel-based alloys. Hydrogen is collected at the cathode and oxygen at the anode. Ionic transfer across the water is aided by the addition of potassium hydroxide (KOH). The typical voltage used is 1.2 V; cells can be set up in a series of stacks increasing production yield. Water is heated to ~70 ºC to increase the rate of the reaction. The process operates at low current densities of <0.4 A/cm^2 and is typically ~ 60-90% efficient (S.S. Labs). Gas purities of 99.8% and 99.2% can be achieved for hydrogen and oxygen respectively; reducing the need for further purification. Stringent monitoring of the contamination of oxygen in hydrogen is required as the lower explosive limit is just 4 atomic %. (S.S. Labs)

2.1.3.2 Splitting Water using Heat

High temperatures give energy to split water into hydrogen and oxygen. The process occurs at temperature > 2000 ºC but the gas mixture then recombines rapidly. The process can be split into several smaller sections by chemical additions. Processes such as next-generation nuclear fission and solar thermal systems have excess heat as which could be used for this production method (Book).

2.2 Separation of Hydrogen

The SMR produces gas streams typically containing 18% CO_2, 7% CH_4 and 1% CO (Hagg); hence it is imperative to separate hydrogen from the gas stream. Selecting hydrogen the purification method used will be a function of the following; required purity, volume required, operational scale, cost and the need for removal of specific contaminants (Fletcher).

2.2.1 Pressure Swing Absorption

Porous materials such as zeolites are used to effectively sieve the gas mixture by adsorbing unrequired gases at high pressures. As contaminate gases are adsorbed the remaining hydrogen can be collected. The pressure is then reduced and the contaminate gases are collected. This leaves the chamber free for a new stream of impure gas to be input. This method can produce hydrogen of up to 99.99% on a large scale. However this system will only allow for ~80% of hydrogen to be recovered due to losses in the purging step (Grashoff).

2.2.2 Cryogenic Distillation

The cryogenic distillation method utilises the low temperature boiling point of hydrogen to separate it from a mixed gas stream. The process may be carried out on a large scale to produce hydrogen. A mixed gas stream is chilled and hydrogen is the last gas to liquefy; as only helium has a lower boiling point than hydrogen; -268.9 ºC compared to 252.9 ºC for hydrogen (Fletcher). Purity of hydrogen produced in this manner is, in practice, limited to ~99% (US DoE NETL). The process is very energy intensive due to chilling the gas stream to extremely low temperatures; however this does allow hydrogen to be stored in liquid form more easily.

2.2.3 Hydrogen Selective Membranes

To further improve the purity of hydrogen gas separation membranes can be used. A pressure gradient across a sealed, semi-permeable membrane material gives the necessary driving force for permeation of hydrogen across its width. Hydrogen is selectively allowed to permeate through the membrane while other impurity gases are rejected. Effect hydrogen selection membranes must have high selectivity of hydrogen from other gases as well as high flux and high rate of flux of hydrogen across the membrane. Membrane materials can operate over a broad range of temperatures and pressures and can operate on small scale portable applications as well as on an industrial scale.

2.2.3.1 Porous Membranes

Porous ceramic, polymer and metallic based materials are available for hydrogen purification. Pores of <1 nm are required for hydrogen purification. This method has a higher recovery than pressure swing absorption >85% but gives lower purity of just 99% as helium, carbon dioxide and water can pass through the system (Grashoff). The low purity means that porous membranes are not suitable for fuel cell applications.

2.2.3.2 Dense Membranes

The only method of producing ultrapure hydrogen (>99.9999%) is to use dense metallic membranes. This method also gives up to 99% recovery from hydrogen rich gas streams (Grashoff). Unlike porous membranes, which allow molecular hydrogen to diffuse across their width, dense metallic membranes split hydrogen into atomic form prior to diffusion, as shown in Figure 2.4 (Sholl).

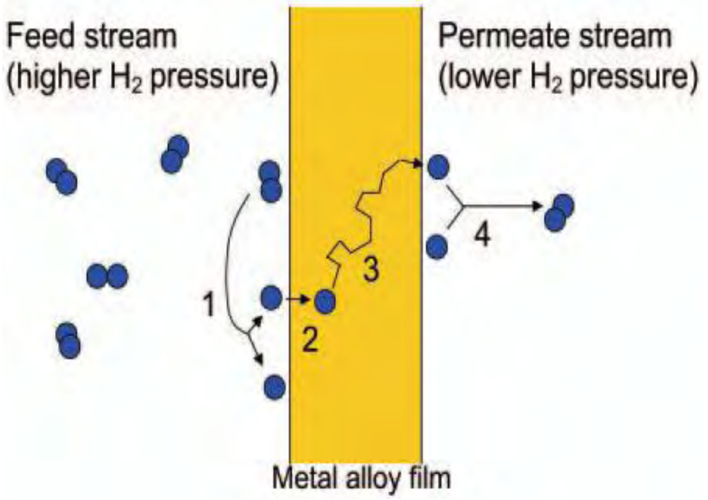

Figure 2.4 – Purification of hydrogen using a palladium based membrane (Sholl).

Hydrogen selectively permeates across the membrane in four stages.

1. A pressurised mixed gas stream, containing a high partial pressure of hydrogen, is fed to one side of the membrane where molecular hydrogen is adsorbed onto its surface. The metallic membrane then acts as a catalyst, allowing hydrogen to dissociate into two hydrogen atoms.
2. Hydrogen atoms are absorbed into the metal lattice.
3. The hydrogen atoms are then transported from the high pressure feed to low pressure permeate side, moving through the interstitial sites of the metal lattice. Atoms move though the lattice in ionic form, an electron ‘screens’ this proton inhibiting a charge imbalance.
4. When the two ‘screened protons’ reach the permeate side of the membrane they can recombine to form a hydrogen molecule (Paglieri).

Theoretically a perfect metal lattice should yield 100% pure hydrogen, as hydrogen is the only atom small enough to permeate across the interstitial sites in the lattice. Minute levels of impurity species will only pass across the membrane due to imperfections in the metal lattice (Paglieri). Hydrogen separated by this mechanism initially requires hydrogen rich gas streams and can only be carried out industrially on a range of operational scales. Dense membranes require catalytic precious metals such as palladium and thus the cost of hydrogen from this technique is high.

2.3 Palladium for Hydrogen Separation

Pure palladium has the ability to catalytically split the hydrogen molecule into hydrogen atoms at its surface, meaning it can be used as a membrane material, selectively allowing hydrogen permeation. Thomas Graham discovered the high solubility of hydrogen in Palladium in the 1860’s; noting that it would absorb 600 times its own volume of hydrogen (Graham).

Palladium has an f.c.c. structure with octahedral and tetrahedral interstitial sites at which small non-metallic atoms such as hydrogen, boron and carbon may sit within the metal lattice. Due to greater distance between nearest neighbour interstitial atoms octahedral lattice sites are favourable for interstitial occupation in an f.c.c. lattice (Jewell). There are however a number of limiting factors to palladium’s use in pure form as a membrane material; including, most crucially, its instability in thermal cycling under hydrogen pressure.

2.3.1 The Pd-H System

At low concentrations of hydrogen where H/Pd is <0.02(α_{max}) only f.c.c. α phase, with hydrogen in solid solution, exists. Above H/Pd = 0.02 palladium-hydride (β) forms. The two phases are immiscible and co-exist in the palladium-hydrogen system until a H/Pd ratio of 0.6 above which only β phase (β_{max}) exists, Figure 2.5 (Grashoff).

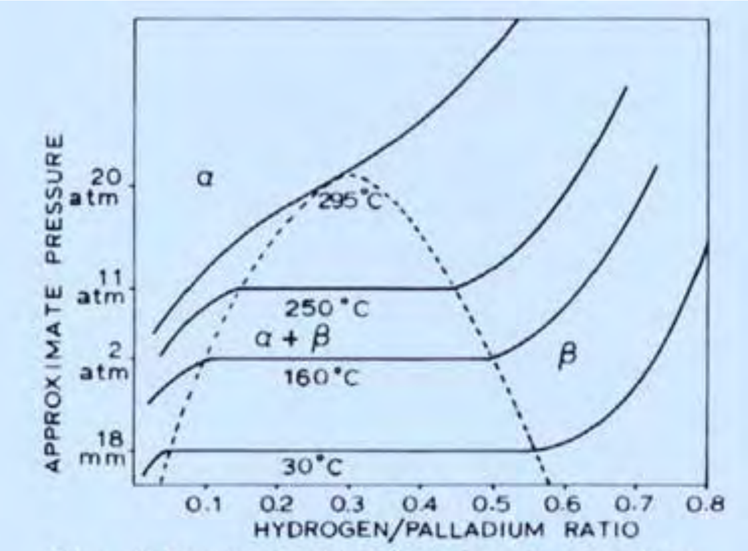

Figure 2.5 – The temperature isotherm, characterising the absorption relationship of the two immiscible f.c.c. phases, α and β (Grashoff).

The β_{max} phase has a lattice parameter of 4.025 Å compared with α_{min} value of 3.895 Å. Thus, during thermal cycling the transition from α to β will result in a 10% volume expansion, leading to a high level of distortion potentially resulting in membrane failure (Pagleiri). The coexistence of these two immiscible phases leads to substantial distortion, strains on the lattice and a high number of dislocations (Wise).

Studies to determine isotherms in the palladium-hydrogen system have been conducted (Bruning and Sieverts; Gillespie and Downs; Gillespie and Sieverts), summarised previously in Figure 2.5. To avoid the phase change in the palladium-hydrogen system, the temperature should be maintained above 300 ºC where only α phase is formed. Additionally the alloy should be cooled in a dehydrogenated condition. The miscibility gap can be eliminated by alloying additions, which can also have the benefit of reduced poisoning, increased strength and permeability.

2.4 Hydrogen Transport across a Dense Metallic Membrane

In order to maximise permeability of hydrogen through a dense metallic membrane there are two principle factors to be considered; the solubility and diffusivity of hydrogen within the material.

The concentration (c) of hydrogen at the surface of the membrane is equal to the pressure of hydrogen in the gas phase (p) multiplied by Sievert's constant (K).

$$c = Kp^{0.5}$$

Equation 2.6

Fick's Law, equation 2.7, is derived from calculations using Sieverts equation (2.6). The difference of the hydrogen pressure either side of the membrane is used to calculate hydrogen flux across the membrane. Hydrogen solubility is, at a given temperature, proportional to the square root of the hydrogen pressure, thus a value of 0.5 is selected for n. Surface dissociation are not a rate limiting factor for permeability of hydrogen in bulk materials (Pagleiri).

Equation 2.7

$$J = \frac{\phi\left(P_i^n - P_{ii}^n\right)}{t}$$

J - Hydrogen Flux ($mol.m^{-1}.s^{-1}$)
ϕ - Permeability ($mol.m^{-1}.s^{-1}.Pa^{n}$)
Pi - Up stream Pressure (MPa)
Pii - Downstream Pressure (MPa)
t - Membrane Thickness (mm)
n – Permeability Constant (0.5)

The parameters used in equation 2.7 may be summarised by the schematic diagram given in Figure 2.6.

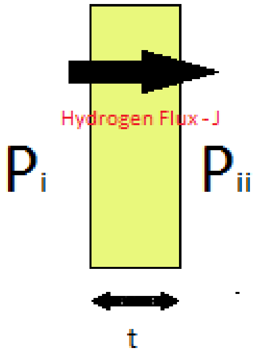

Figure 2.6 – Membrane flux parameters.

As hydrogen flux is a product of both diffusivity and solubility of hydrogen through a material, to increase permeability across membrane either or both of these factors must be increased (Pagleiri). In order to manipulate the diffusivity or solubility of hydrogen in palladium alloying is required. Additionally, the hydrogen flux of the membrane may be increased by increasing the membrane area or by reducing the thickness. A reduction in thickness also has the benefit of decreasing cost, as less raw material is used. Foils can be cast and rolled for use as hydrogen purification membranes however, due to the high pressure difference either side of the membrane, supporting materials are often required in order to prevent distortion of the membrane (Nanu).

2.5 Binary Pd Alloys

In order to counteract the issues of pure palladium alloying is required. Alloying of palladium has been investigated thoroughly with the key aims being to reduce distortion upon thermal cycling by closing the α-β miscibility gap, improve resistance to poisoning and maintain or increase the permeability of the alloy.

A comparison of maximum permeability values for a range of palladium based alloys at 350 ºC and 20.68 bar are shown in Figure 2.7 (Grashoff). Palladium-Yttrium is the alloy with the highest measured permeability. Gold, copper, cerium and silver also have been shown to increase permeability from that of pure palladium (Grashoff). These alloys form a substitutional solid solution (Grashoff). The α to β phase transition is reduced, the miscibility gap is shifted to below room temperature. Several Pd-based binary alloys, such as those containing Au, Ag and Cu, also have improved mechanical properties and resistance to poisoning.

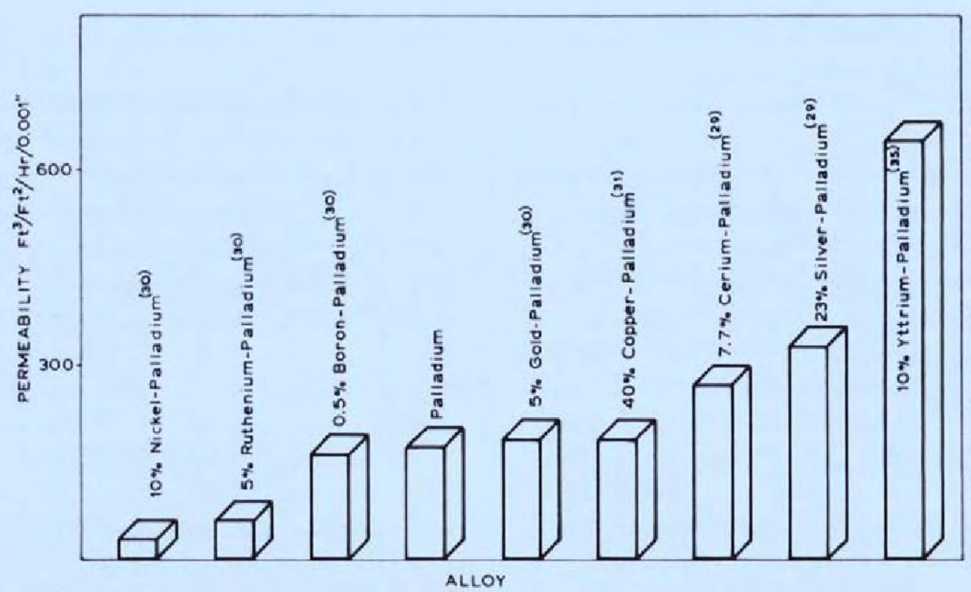

Figure 2.7 – A comparison of maximum permeability values for a selection of binary palladium based alloys at 350 ºC and 20.68bar pressure (Grashoff).

Several papers and patents have shown (Hurlbert, McKinley, Allard, Topsoe) that additions of boron, which occupies interstitial sites, can also be beneficial. However the Pd-B binary alloy itself has a lower hydrogen permeability than pure palladium.

2.5.1 Contamination and Poisoning

There are three processes which can inhibit catalytic activity of a membrane surface (Musket):

1. Impurities segregate to the surface of the palladium membrane during annealing, inhibiting the dissociation of the hydrogen molecule by reducing the number of active sites.
2. Formation of corrosion products at the surface of the material can occur due to exposure to aggressive environmental conditions.

3. Chemisorption of impurities found in the feed gas; carbon monoxide and sulphur based compounds, particularly hydrogen sulphide, are known to be particularly damaging.

2.5.1.1 Effect of Carbon Monoxide (CO)

Carbon monoxide is most abundant in gas streams produced from hydrocarbon sources such as coal gasification and SMR (SMR DoE). The presence of carbon monoxide is known to reduce the permeability of hydrogen in pure palladium. Reductions in hydrogen permeation flux were also found at low temperatures and high CO concentrations (Gao). Amandasson observed comparable permeability at 300 ºC; below 150 ºC however the permeability of hydrogen in palladium foils tended towards zero.

2.5.1.2 Effect of Hydrogen Sulphide (H_2S)

Poisoning at the surface of the palladium alloy reduces its catalytic activity. The presence of hydrogen sulphide in the feed gas stream results in drastic reductions in permeability. Hurlbert showed that 5 minutes exposure at concentrations of just 50 volume ppm of H_2S can reduce permeability by 20%. In an hour formation of palladium sulphide in conjunction with the growth of cracks and pores led to structural stresses; due to the high lattice constant of Pd-S (Kulprathipanja). Structural stresses may also lead to the permeation of impurity gases (Kajiwara). Water has been shown to increase the rate formation of the Pd-S phase (Kulprathipanja).

2.5.2 Characteristics of a Successful Membrane

For a successful membrane alloy the following points should be satisfied (Pagleiri):

1. Selectively allows only hydrogen to permeate.
2. Effective for prolonged periods at high temperatures and pressures accompanied by low distortion upon thermal cycling in the presence of hydrogen, in order to allow variable temperature and pressure conditions.
3. Resistant to poisoning from hydrogen sulphide, chlorine, carbon monoxide, hydrocarbons and other contaminants of the input gas stream.
4. High output of hydrogen per unit volume.
5. Ability to reduce thickness, to both increase output and decrease material costs.

2.5.3 Palladium Silver

A large volume of research has been carried out on Pd-Ag alloys, which are the current alloy system used in commercial purifiers. The α/β miscibility gap is closed by the addition of silver, with maximum permeability measured at ~23at%Ag (Pagleiri). Despite a reduction of hydrogen diffusivity a large increase in hydrogen solubility gradient leads to a net increase in permeability compared to pure Pd (Amandusson). Pd-Ag alloy has a slight increase in strength compared to pure palladium. Further benefits include resistance to impurities of NH, CH_4, CO_2, CO and N although resistance to H_2S is still relatively poor (Yoshida). The lifetime of palladium-silver membranes is limited by expansion of the lattice upon absorption of hydrogen, the Pd to α transition. Furthermore, prolonged exposure to high temperatures will also result in grain coarsening, which will also reduce strength (Pagleiri).

2.5.4 Pd-Cu

Of particular interested to industry is that the highest recorded permeability occurs at ~40wt%Cu; thus the alloy is cheaper to produce as it uses less palladium (McKinley). The addition of copper also improves alloy ductility; making rolling of foils to a given thickness less energy intensive and hence cheaper. A reduction in effective operation temperature from palladium-silver would also be beneficial to commercial applications, it has been shown that maximise membrane performance for Pd-Cu is ~350 ºC (McKinley, Thoen and Roa).

Unlike palladium-silver the solubility of hydrogen in the Pd-Cu alloy is less than that of pure palladium; however diffusivity of hydrogen greatly exceeds that of Pd or Pd-Ag. Furthermore the solubility gradient across the membrane, from the high- to the low-pressure side, does not vary as greatly as Pd-Ag. This leads to a reduction in volume expansion upon hydrogen absorption and thus increases durability. Although the alloy has a greater permeability than pure palladium, it is still far lower than that of palladium silver (Grashoff). Pd-Cu may also be rolled thinner than Pd-Ag, due to greater strength and ductility, this both increases permeation rates and reduces the amount of alloy material required.

2.5.4.1 Resistance to H_2S

Improved resistance to poisoning of the alloy by sulphur containing compounds, such as H_2S, is another advantage to Pd-Cu. Rather than exposure time, concentration of H_2S in the gas stream has been shown to be the main factor in inhibiting both pure Pd and Pd-Cu permeation. Hydrogen permeation of pure Pd is completely inhibited by 100 ppm of H_2S in the gas stream whereas for Pd-Cu (47at%Pd) inhibition is extended to 300 ppm (Kulprathinpanja). At greater H_2S concentrations the presence of f.c.c. phase was shown to give enhanced resistance to poisoning (Rothenberger).

Blocking of membrane dissociation sites inhibits permeation. The membrane surface condition has also been shown to effect susceptibility to H_2S. Rougher surfaces have been shown to have lower H_2S tolerance; this has been attributed to broken bonds at grain boundaries giving more sulphur adsorption sites (Kulprathinpanja).

2.6 The Structure of Pd-Cu

2.6.1 Crystal Structure

Initial studies into the Pd-Cu system were carried out by Reur in 1906; further studies included Jones and Sykes, Taylor, Jaumot and Savertsky and Nemilov. More recently Subramanian and Laughlin carried out an extensive study detailing the various phases present in the alloy. The most current phase diagram developed using CALPHAD phase diagram construction software was developed by both Huang and Li et al and is shown, Figure 2.8. Of particular interest to membrane applications are the β (or B2) b.c.c. phase between ~35-50 at% Pd and the mixed phase region up to ~67 at%Pd, due to higher permeability. The maximum temperature at which the β phase exists is 596 ºC, at 40 at%Pd, Above which only α phase remains and there is a complete range of solid solubility (Huang). Neighbouring mixed phase regions, of b.c.c. β and f.c.c. α. lie adjacent to either side of the β phase field. Lower palladium concentration phases have also been thoroughly researched showing an ordered Cu_3Pd type unit cell below 20 atomic % Pd as well as 1D-LPS and 2D-LPS structures (Subamranian and Laughlin).

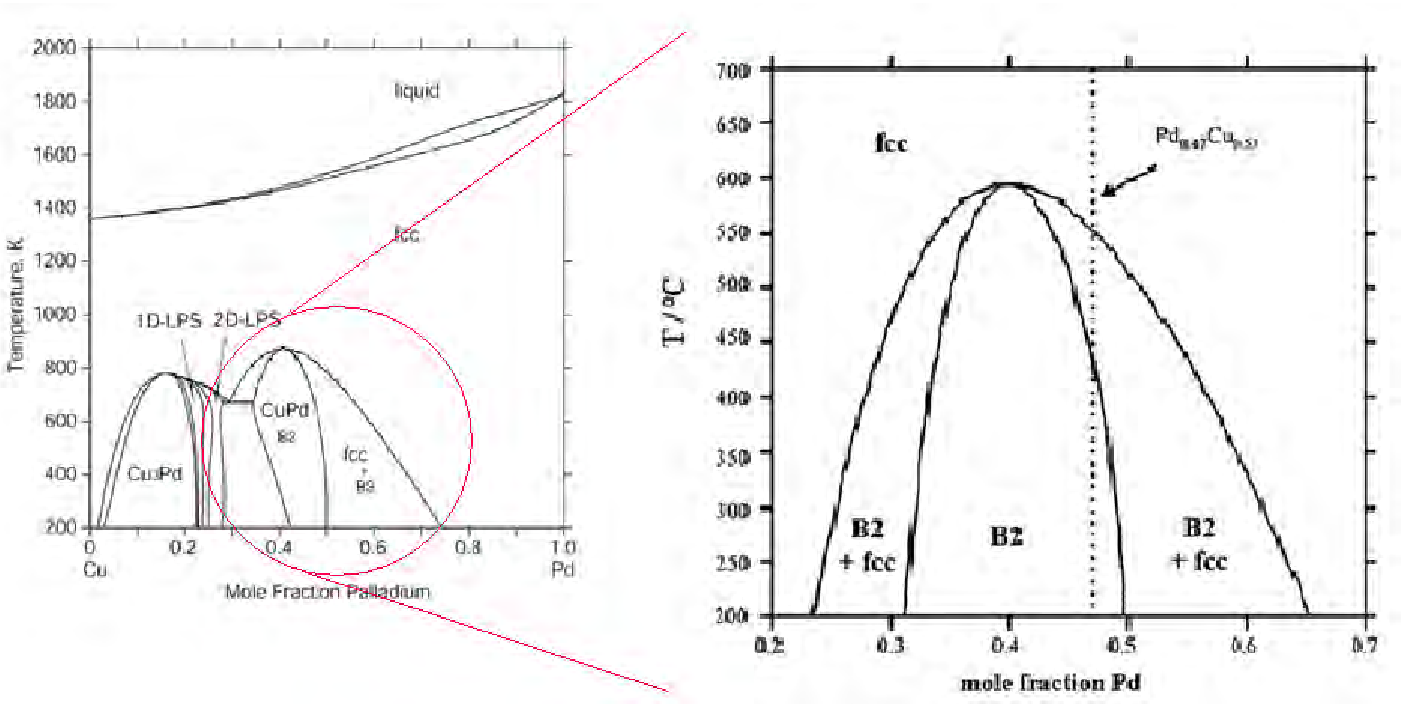

Figure 2.8 – The Pd-Cu phase diagram around the high permeability α+β phase field (Li AND Decaux).

2.6.2 Permeability in Relation to Structure

A strong relationship between hydrogen alloy composition, crystal structure and permeability has been established (Volkl, Rothenberg, Piper). McKinley first located a peak in permeability at 47 atomic %Pd when measured at 350 ºC. Indeed a shift in composition of just 3 atom % can be attributed to a reduction in permeability of 50%, as shown in Figure 2.9.

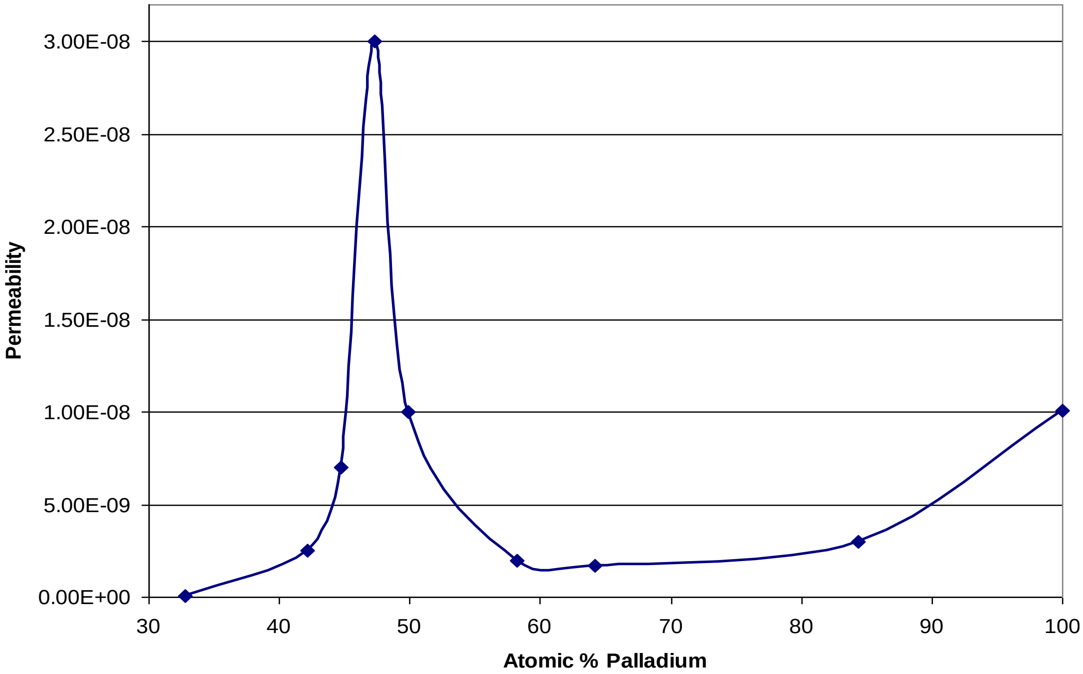

Figure 2.9 – Variations in permeability for a range of Pd-Cu alloys at 350 ºC.

The diffusion coefficient reaches a maximum value in the β phase field. Diffusion, in f.c.c lattices, takes place via the octahedral interstitial sites whereas in a b.c.c. material the tetrahedral interstices sites are occupied. It has been found that this leads to a decrease in activation energy for diffusion. A comparison of diffusivity of hydrogen in a 47 at%Pd alloy showed significantly higher values for equilibrium cooled b.c.c. structure than that of quenched f.c.c. (Volkl).

Despite higher diffusivity Figure 2.9 shows a large decrease in permeability as copper content increases. This may be attributed to a reduction in solubility of hydrogen upon the development of a fully b.c.c. structure, as modelled by Huang et al using CALPHAD software, Figure 2.10.

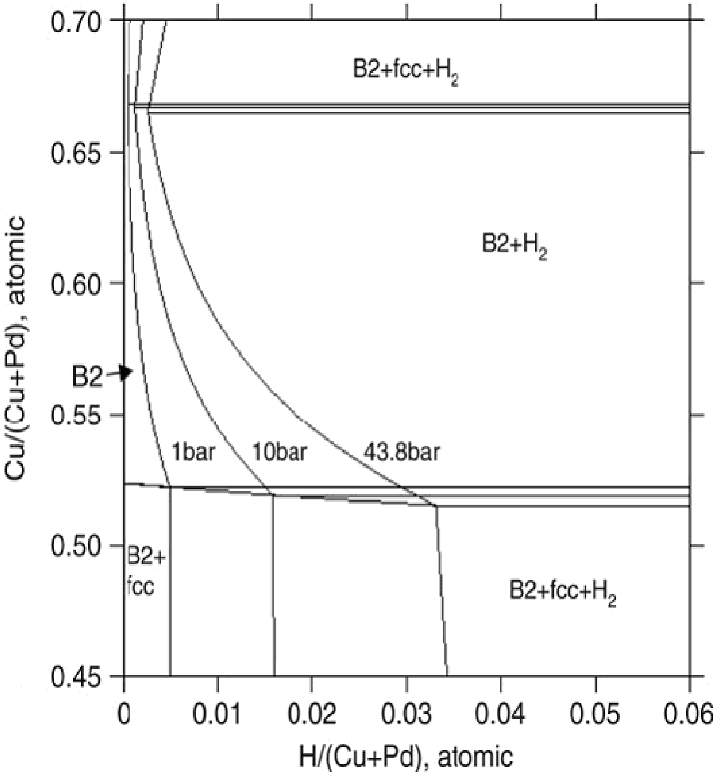

Figure 2.10 – Reduction in solubility of hydrogen upon the transformation from the mixed phase to fully b.c.c.; the boundary line for which also appears to change under increased hydrogen overpressure (Huang).

2.6.3 The Effect of Hydrogen on Pd-Cu

Work by Piper on a selection of Pd-Cu foils, including those around the β phase field, calculated the diffusion coefficient of hydrogen by measuring electrical resistivity at varying hydrogen pressures. It was shown that interstitial hydrogen solution has the affect of shifting the phase boundary towards more Pd-rich compositions. The system is now a ternary of Pd-Cu-H, a summary of these results is shown in Figure 2.11. The shift in the phase boundary does not appear to be linear with 0 atm (0 bar) and 5 atm (5.07 bar) exhibiting a greater variation in phase boundary position than between 5 to 120atm (120 = 121.59 bar). A similar effect has later been demonstrated by Huang (Figure 2.10) where the diagram also appears to demonstrate variation in the phase boundary line under increasing hydrogen overpressures.

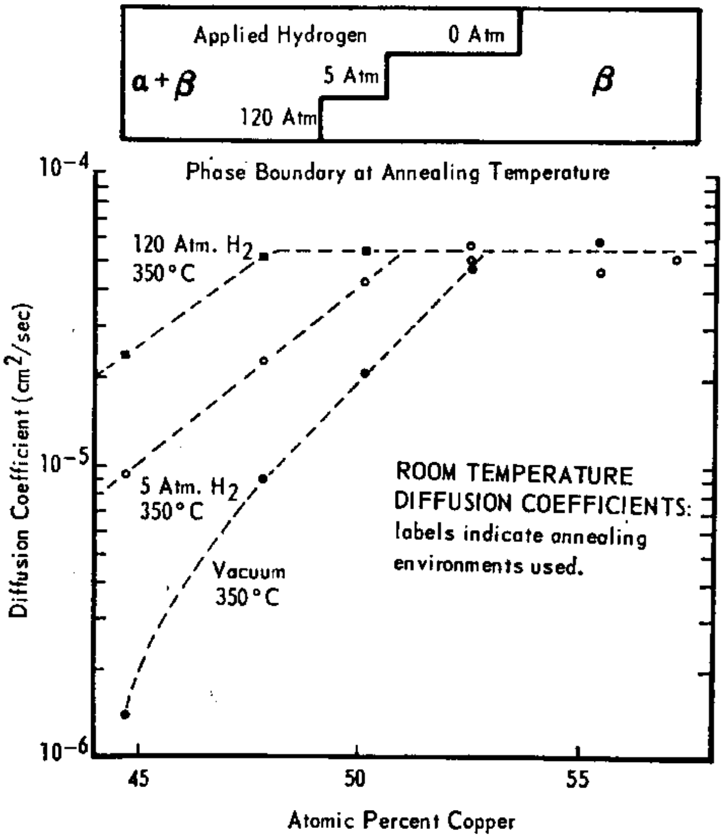

Figure 2.11 – The effect of hydrogen pressure on the room temperature diffusion coefficients of a range of palladium-copper alloy foils (Piper).

Development of the b.c.c. phase is facilitated by the presence of hydrogen. No reference has been made in the literature to a purely b.c.c. sample 47 at% palladium heat treated under an inert or vacuum atmosphere. When annealed in the presence of hydrogen a fully b.c.c. structure, of the same elemental composition, is easily achieved (Goldbach). Decaux investigated this phenomenon by heat-treating quenched f.c.c. foils at 200 ºC for 556 hours, which did not yield any b.c.c. phase. However, at 250 ºC, b.c.c. phase was produced with further heat treatment at this temperature (Decaux).

This may be an indication that hydrogen promotes the development of the b.c.c phase. Indeed, calculations from first principles show that the enthalpy of formation at room temperature of the Pd-Cu phase to be −12.73 kJ/mol, whereas enthalpy of formation of the hydrogenated phases CuPdH and $CuPdH_2$ to be −7.20 and 2.32 respectively (Huang). The promotion of the phase transformation in the presence of hydrogen may be the source of this anomaly. It may also be the case that the current phase diagram widely, referred to in the literature (Figure 2.8) (Subramanian and Laughlin), may be plotted incorrectly and this composition does not ever produce purely b.c.c. phase. Other binary phase diagrams reported in the literature show the high permeability composition to lie on the phase boundary itself, Figure 2.12.

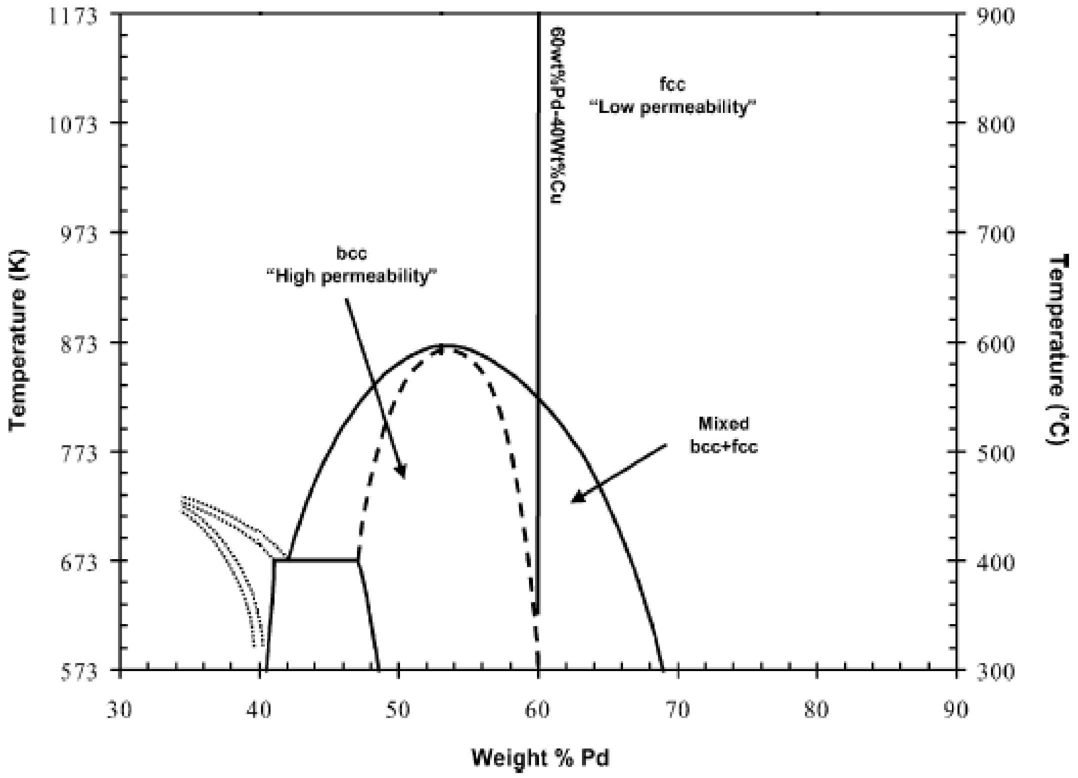

Figure 2.12 – The Pd-Cu phase diagram as reported by Howard.

Kinetic effects may also influence the shape of the phase diagram at low temperatures and thus a more conclusive study is required. If the composition of the high permeability alloy does lie in the mixed phase region at room temperature, a shift in the phase boundary in the presence of hydrogen at this composition may facilitate b.c.c. formation. The formation of some b.c.c. phase at 250 ºC described by Decaux was simply to overcome the higher enthalpy of formation value without hydrogen present.

Another effect of hydrogen on the binary Pd-Cu alloy is permeation hysteresis upon temperature cycling. Permeability tests by Yuan show a variation of the phase boundary under heating and cooling cycles (Yuan). Upon cooling of the fully f.c.c. alloy (47.3 at% Pd) the transition to mixed phase was suppressed in comparison to heating, Figure 2.13. Results were taken from XRD fragments of alloys annealed in hydrogen and hydrogen permeability measurements. Metastable hydrogenated f.c.c. PdCu phases exist and upon cooling they may limit stoichiometric segregation brought about by prolonged exposure to temperatures in the mixed phase region (Yuan).

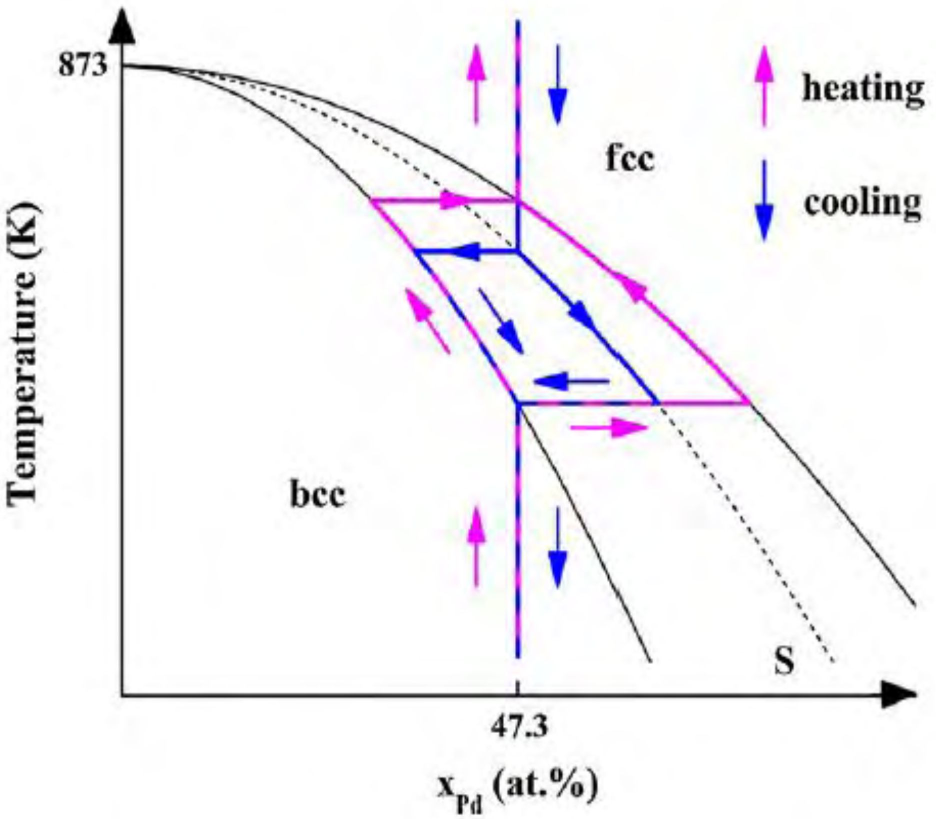

Figure 2.13 – Non-equivalent phase transformation of fcc/bcc upon heating and cooling at 47.3 atomic %Pd (Goldbach).

Compositional segregation of f.c.c. and b.c.c. phases in the alloy may lead to reduced permeability. As shown in Figure 2.9 a small shift of b.c.c., to lower Pd content, or f.c.c., to higher Pd content, gives rise to a large reduction in permeability of both phases. Furthermore, when in the mixed phase, temperature fluctuations may lead to stresses and microscopic cracks at the grain boundaries; due to larger solubility of hydrogen in the f.c.c. phase Figure 2.10. Solubility variations also mean initial growth of b.c.c. phase from coexisting f.c.c. grains may results in gas pockets forming at grain boundaries; reducing strength and membrane selectivity. This puts the long-term properties of the membrane under thermal cycling under scrutiny (Goldbach).

2.6.4 Structural Gradient across Membrane

It has been shown that hydrogen has the effect of shifting the composition of Pd-Cu structures and the extent of the shift is governed by hydrogen concentration: hydrogen acts as an additional alloying element forming a ternary system of Pd-Cu-H (Piper). As a pressure differential across the membrane is essential for mass transport of hydrogen, a concentration gradient of hydrogen and hence a structural variation through the material will exist. The extent of the hydrogen concentration profile across the membrane is largely unknown. A comprehensive study of the ternary Pd-Cu-H system at a range of pressures has also yet to be completed. Should the downstream side of the membrane have a low hydrogen pressure it may have the effect of reducing the permeability of the alloy, despite a higher pressure-differential. Slight shifts in composition have been shown to have a strong effect on permeability Figure 2.9. As the concentration profile across the membrane width is unknown two possible profiles are shown in red and blue (Figure 2.14).

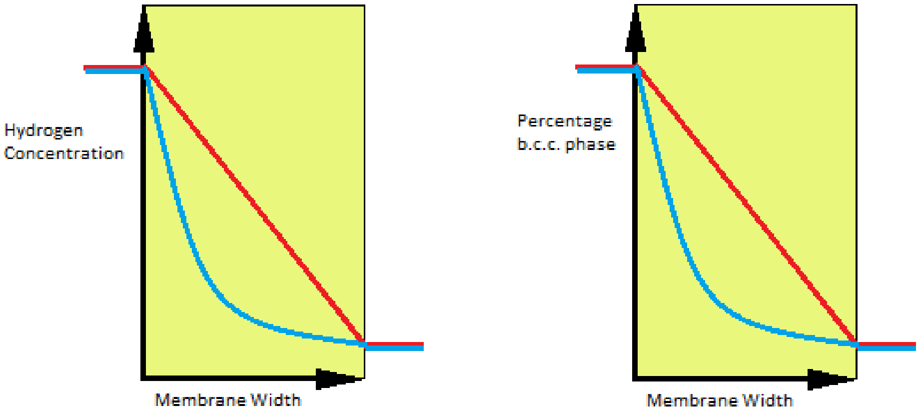

Figure 2.14 – A schematic diagram of possible hydrogen concentration profiles and the corresponding structural variation in the Pd-Cu membrane.

2.7 Aims and Objectives

The aim of this project is to investigate and establish the effect of hydrogen on the binary phase diagram of Pd-Cu, in particular around the high permeability (47 at% Pd) region. Experimental data collected on phase transitions under inert and hydrogenated experiments, at a variety of hydrogen pressures, will be compared. These results may then be used in order to investigate a ternary system of Pd-Cu-H.

Data from hydrogenated phase transitions and the relative amount of b.c.c. phase present at these temperatures will then be used to rationalise the collected permeability data. From this data it will then be possible to approximate the conditions under which the highest permeability can be achieved, including: the alloy composition; upstream and downstream pressure; and operating temperature.

3 Experimental Methods

In order to investigate the effect of hydrogen on the phase transition temperature of Pd-Cu, three different alloy compositions were provided by Johnson Matthey Noble Metals (Royston, UK) with nominal compositions around the high permeability region (Pd-Cu53at%). In their as-received state the alloys had been cold-rolled from a cast ingot into a foil. Due to the formation of copper-oxide layers, at the surface of the foil, a solution of 50% HCl was used to etch samples for 1 minute.

All samples were annealed at 500 ºC for 72 hours either under vacuum or under pressure of inert argon gas; to ensure homogeneity. All samples were cooled from 500 ºC to room temperature at a rate less than 2 ºC per minute. Although higher temperatures may have been preferable for this treatment, 500 ºC was used in order to avoid formation of copper-oxides and interdiffusion with the steel based annealing furnace.

Initial experiments focussed on characterisation of the crystal structure and morphology of each of the alloys by X-Ray Diffraction (XRD) and Energy Dispersive Spectroscopy (EDS) using a Scanning Electron Microscopy (SEM). As described in Section 2.6. The nature of the phase diagram is such that even slight variations in composition can have large effects on transition temperature, particularly around the high permeability region, making an accurate assessment of alloy compositions crucial.

The effect of elevated temperatures on the phase structure and stability in inert atmospheres were then determined using XRD and Differential Scanning Calorimetry (DSC). Similar tests were then performed at high temperature under a range of hydrogen pressures, also using XRD and DSC. These experiments were used to determine the nature of the phase transformations under typical membrane operating conditions, and to relate the structural information to the observed hydrogen permeabilities.

3.1 Characterisation of Composition and Structure

In order to accurately investigate the effect of hydrogen on the phase diagram, the composition of each alloy must be determined. EDS was performed for elemental analysis of the percentage composition of the alloy. X-Ray Diffraction (XRD) was also used in the characterisation of alloy structure and composition. XRD spectra were refined by Rietveld analysis, using Topas© software to allow a quantitative comparison of the proportion of f.c.c. and b.c.c. phases present in the alloy. Lattice spacings from the XRD spectra were then used to determine the alloy composition using a variant on Vegard's Rule, based on data collected from the literature.

3.1.1 Scanning Electron Microscopy (SEM)

A JEOL 6060 SEM, equipped with INCA EDS software was used to image the microstructure of Pd-Cu samples at various stages during this work. The Pd-Cu samples were mounted in conducting Bakelite, polished on a series of SiC papers and diamond paste-impregnated papers (up to a 1μm diamond paper). Secondary electron images were taken to view the alloys surface condition, and backscattered images were used to assess compositional homogeneity. It was hoped that the Pd-rich and Pd-depleted areas would give an indication of the size and prevalence of mixed f.c.c. and b.c.c. phases which are stoichiometrically dissimilar. An INCA 300 energy dispersive spectrometer was used for elemental analysis of composition. Analysis of both areas and spots of the lighter and darker regions in backscattered image were used to verify compositional differences in the material. In combination with this, regions on the surface of the alloy which appeared to show inclusions were analysed.

3.1.2 X-Ray Diffraction

XRD spectra were produced with a Bruker D8 Advance diffractometer. Scans were performed over a 2θ range of 20-100°. The XRD spectra produced in this project can be used to show the presence of phases in as-received condition as well as after exposure to various annealing conditions.

In addition, the XRD spectra were used to calculate the lattice spacing (a) with Equation 3.1, where the‘d’ values of the peaks are given by Equation 3.2). The atomic volume of b.c.c. and f.c.c. phases were also calculated using the lattice spacings value, Equations 3.3 and 3.4. The peak intensities gave an indication of the degree of texture induced during rolling of the samples. Topas software © was been used to more accurately calculate the lattice spacing of the f.c.c. and b.c.c. phases and to quantitatively estimate the relative percentage of each phase present.

Lattice Spacing:	$a = d (h^2 + k^2 + l^2)^{0.5}$	**Equation 3.1**
Bragg's Law:	$n\lambda = 2d \sin\theta$	**Equation 3.2**
Atomic Volume (f.c.c.):	$a^3 / 4$	**Equation 3.3**
Atomic Volume (b.c.c.):	$a^3 / 2$	**Equation 3.4**

3.2 High Temperature Inert and Hydrogenated Testing

Once the composition of each Pd-Cu batch had been established the effect of elevated temperatures on phase transitions was determined. Three principle techniques were used during the course of this work; Differential Scanning Calorimetry (DSC), in-situ XRD and hydrogen permeability measurements, which were performed using the bespoke hydrogen flow rig constructed at the University of Birmingham.

3.2.1 In-Situ X-Ray Diffraction

An Anton-Parr cell, on a Bruker D8 Advance diffractometer, was used for XRD under pressurised conditions and elevated temperatures. For each of the alloys scans were carried out under 1bar He as well as 1, 5 and 10 bar H_2. In total, 36 scans were taken from 2θ values of 20-100º. Initially a room temperature scan was made followed by further scans at 50 ºC intervals up to 450 ºC, after which scans were made at 25 ºC intervals up 700 ºC, and then scans were made at the same temperatures on cooling. A heating and cooling rate of 2 ºC per minute was used with a dwell time of 20 minutes for each scan.

3.2.2 Hydrogen Flow Rig

Hydrogen flux across the Pd-Cu membranes has been determined over a range of temperatures and pressures. A schematic diagram of the hydrogen flow rig is shown in Figure 3.1 (Fletcher).

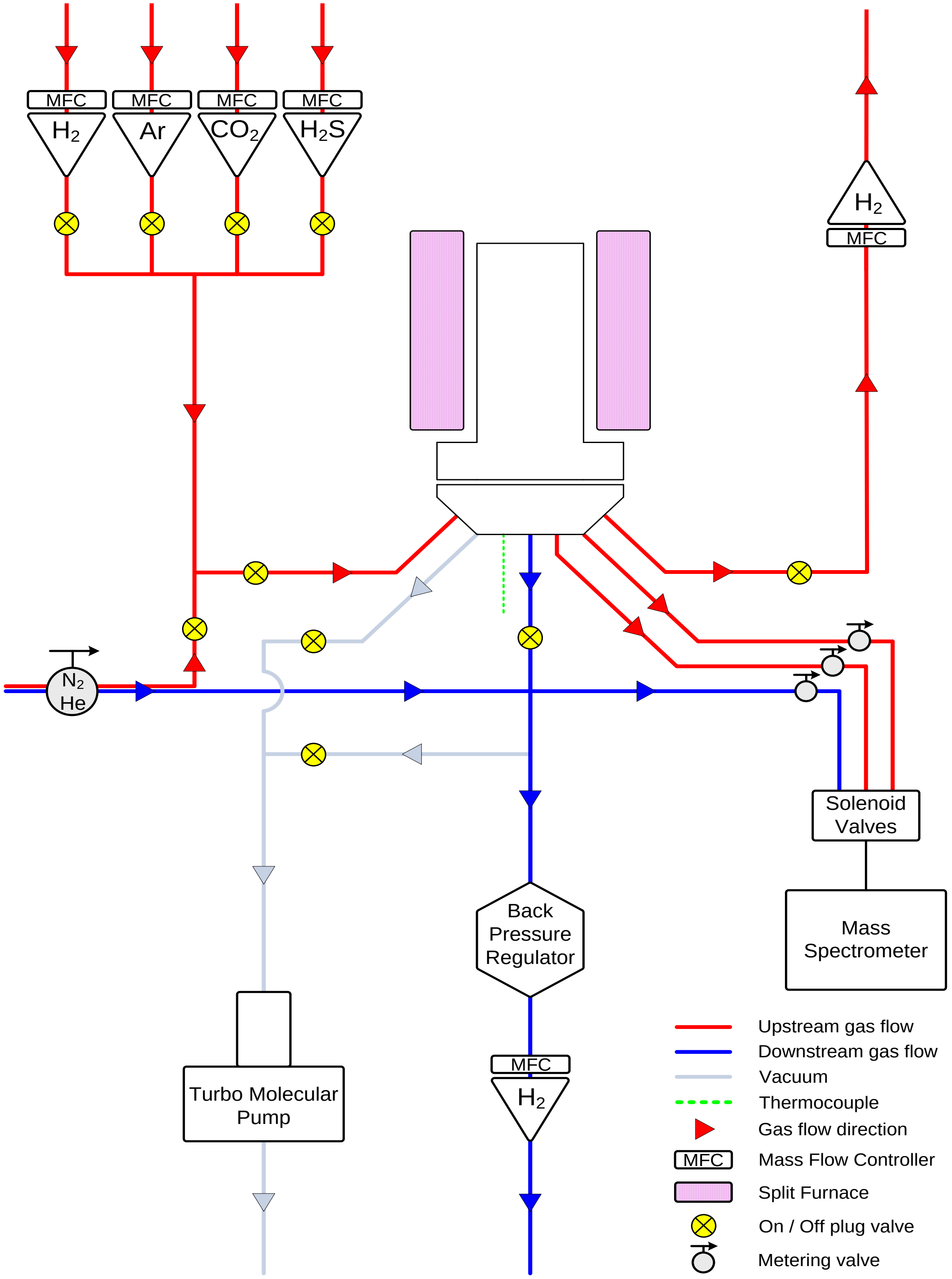

Figure 3.1 – A schematic view of the hydrogen flow rig, developed at the University of Birmingham. (Fletcher)

A membrane is placed between an annealed copper gasket and a knife-edge to give a leak free-seal, Figure 3.2 (Fletcher). To verify the system was leak-free a pressure differential was put in place across the membrane using argon gas, which cannot permeate through the membrane. Any flow on the downstream side would thus be a result of leaking at the seal or elsewhere on the system. After the leak-test the chamber was placed under vacuum and then purged with hydrogen.

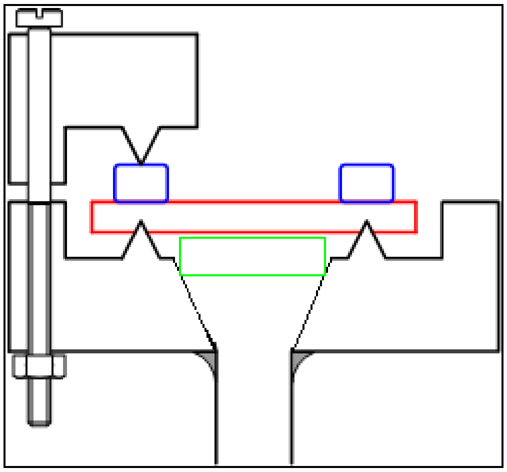

Figure 3.2 – A membrane material (red) held in place by a knife edge seal (black) using copper gasket (blue) with a macro-porous stainless steel support (green) (Fletcher).

A constant pressure of 10 bar was applied to the upstream side of the membrane, whilst the downstream side was regulated to 1, 3 and 5 bar, using a back-pressure regulator. A furnace surrounding the sealed chamber in which the membrane lies was heated to >400 ºC at 2 ºC/min. Heating was continued until a thermocouple inside the furnace, 2 mm below the membrane, reached 400 ºC. When the membrane temperature reached 400 ºC the furnace was allowed to cool to room temperature at a rate of ~1 ºC/min. For each experiment two thermal cycles were made.

The rate at which hydrogen passes through the membrane is measured using a mass flow controller. This data can be used to calculate the permeability of hydrogen through the membrane material, which unlike hydrogen flux, considers membrane area and thickness.

3.2.3 Differential Scanning Calorimetry

Tests have been carried out using a Netzsch DSC204HP with finely chopped Pd-Cu foils seated in sealed aluminium pans. Tests were carried out between 30 and 590 ºC using a heating/cooling rate of 2 ºC/min. The samples were then held at 590 ºC for 10 minutes prior to cooling. The maximum temperature attainable on the equipment was 590 ºC. Initial measurements were performed on each of the alloys under 3 bar Ar (gauge pressure) for comparison with binary phase diagrams reported in the literature; Huang (Figure 2.8) and Subramanian and Laughlin (Figure 2.12). Subsequent measurements were performed under 3 and 10 bar hydrogen overpressures to study the effect of hydrogenation conditions on phase transformations. It should be noted that throughout this work all pressure values are given as gauge not absolute values, as per the literature.

4 Results and Discussion

Visual observations of Batches 1 and 2 showed acceptable surface and general condition. Batch 3 appeared to have surface oxides; data was generally less reliable limiting analysis. Firstly the structure and characterisation of alloys has been established, the effect of a hydrogenated atmosphere on phase transformations has been investigated and finally results from various hydrogen permeability measurements are shown. In each of these sections results are presented moving across the phase diagram with lowest palladium content reported first. The nominal composition values, given by Johnson Matthey, indicated that Batch 2 would have the highest Cu content followed by Batches 1 and 3 respectively moving towards the Pd-rich end of the phase diagram. Details of the alloy batches are summarised in Table 4.1.

Table 4.1– Pd-Cu alloy batch details

Batch	**Nominal Composition (at %)**	**Observed Surface Condition**	**Measured Thickness**
1	$Pd_{49}Cu_{51}$	Acceptable	102 µm
2	$Pd_{47}Cu_{53}$	Acceptable	31 µm
3	$Pd_{52}Cu_{48}$	Oxidised	33 µm

Heat treatments were carried out to anneal alloys and give greater homogeneity across the foil. Specimens were heated at 500 ºC for 72 hours either under vacuum or in inert Nitrogen or Argon gas. The specimens were cooled slowly at <1 ºC per minute in order to replicate equilibrium conditions. It may be assumed that all data presented is for vacuum or inertly annealed specimens unless otherwise stated.

Prior to any homogenising heat treatment it was necessary to check surfaces for the presence of CuO and Cu_2O oxides, formed during membrane fabrication and noted in previous Department of Metallurgy and Materials work on the same binary alloy system (Fletcher Private Communication). Visual inspection of Batches 1 and 2 did not show any obvious surface oxides, however for Batch 3 surface oxides were observed on either side of the alloy. XRD analysis was used to confirm the presence of such oxides.

4.1 Measurements of Composition and Crystal Structure

4.1.1 XRD Analysis of Membrane Crystal Structure and Composition

For reference XRD traces of f.c.c. and b.c.c. Pd-Cu alloys (47 at% Pd) are shown, Figure 4.1. This is accompanied by a table of approximate peak positions and their corresponding crystallographic planes in Table 4.2

Table 4.2 – Approximate peak positions and hkl values

Phase	2θ	hkl
F.c.c.	41	111
	48	200
	71	220
	86	311
	91	222
B.c.c.	30	100
	43	110
	53	111
	62	200
	71	210
	78	211
	94	220

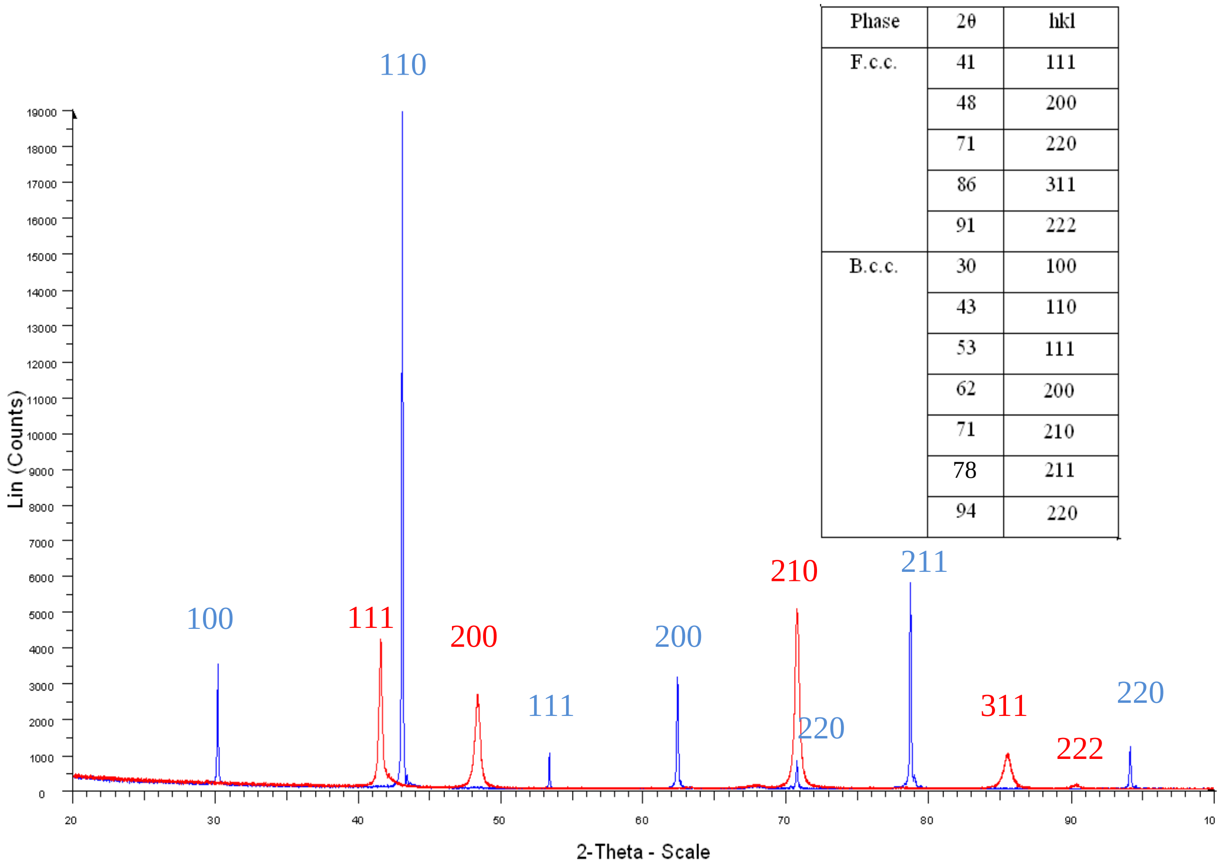

Figure 4.1 – XRD trace of a fully f.c.c. (red) and full b.c.c. (blue) Pd-Cu structure. Using Batch 2 nominal composition $Pd_{47}Cu_{53}$.

It shall be noted that the b.c.c. phase in this alloy is ordered and so an additional peak at (100) is observed. In order to calculate the composition of an alloy Vegard's Law

(Denton) may be used. As the atomic % of Palladium in the Pd-Cu alloy increases so will the lattice spacing. Vegard's law approximates the transition to be linear for binary alloys; however in the case of the f.c.c. phase, using data from the literature (McKinley Piper, Volkl, Nemilov, Jones & Sykes, Jaumot and Sawatzky), it has been shown to have a curved shape, Figure 4.2

The lattice parameter values, calculated using Topas software, of XRD traces can be used to establish the composition of the alloy, from the lattice spacing versus composition variation shown in Figure 4.2. For mixed phase samples the relative amount of each phase, also calculated using Topas, will be considered in calculating the composition of the alloy. Topas software calculates the relative weight percentages of each phase based on a perfect crystal lattice. Unless otherwise stated, when comparing the proportion of each phase weight percentages are referred to, purely as a consistent means of comparison. A tolerance of +/- 3.5% is assumed for all XRD work.

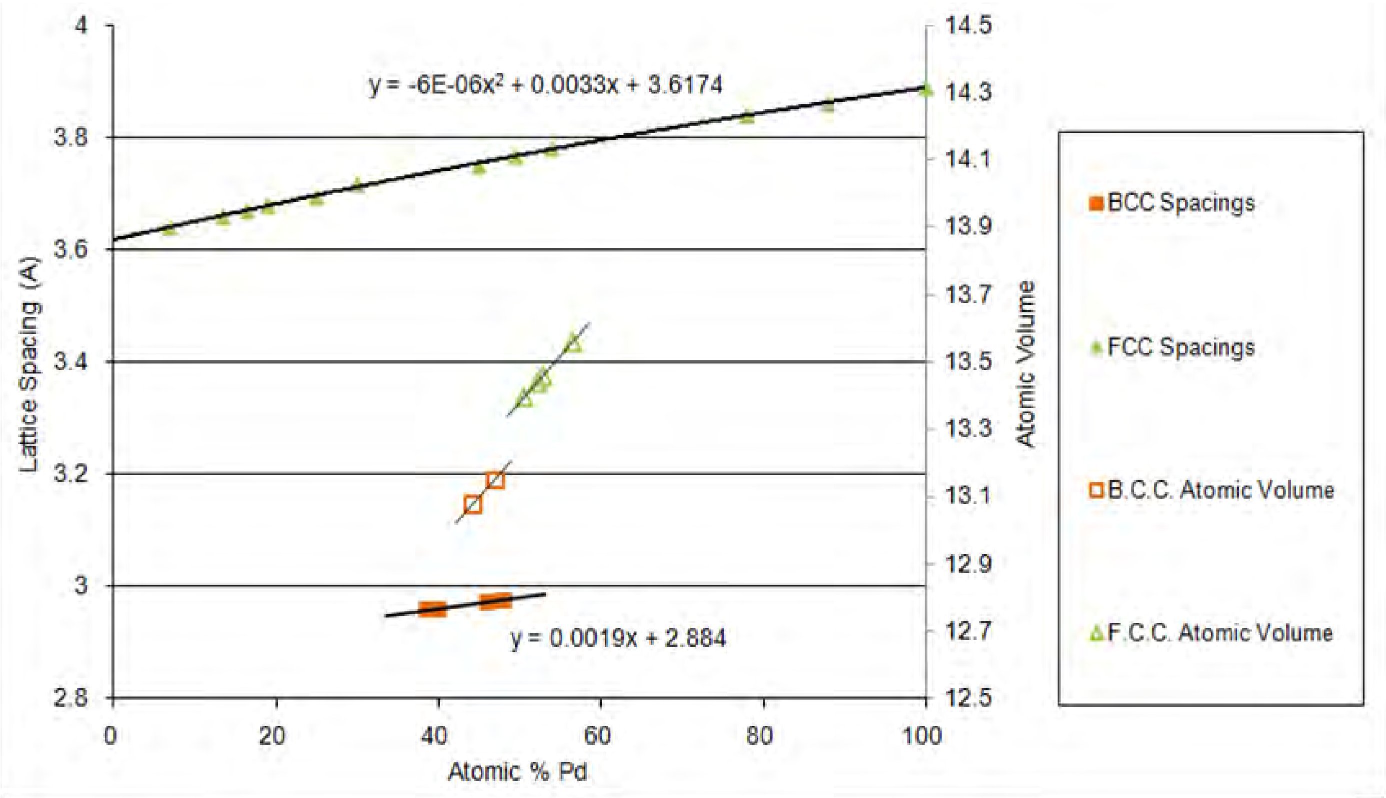

Figure 4.2 – A graph to show the relationship between Lattice Spacing and Atomic Volume against Atomic % Pd, for both f.c.c. and b.c.c. structures of palladium copper.

An erroneous peak at ~68° was found for a large number of scans; this was attributed to a reflection from the diffractometer, sample holder, furthermore some XRD scans show a shift in the entire spectra by 1° due to system and computing errors, this does not affect the accuracy of the relative phase proportions calculated by Topas. Where relevant these common errors are cited when describing the results.

4.1.2 Batch 2 – Nominal Composition of ~47at% Pd

Based on previous investigations (McKinley, Piper, Goldbach, Decaux, Volkl, Howard, Yuan) this alloy was expected to exhibit the greatest hydrogen permeability due to its nominal composition. The surface condition appeared to be smooth reflective and free from oxides. Using a micrometer the thickness of the alloy was found to be 31μm thick.

The as-received alloy had been quenched from >600 °C and cold rolled, rather than equilibrium slow cooled and thus, as expected from the Pd-Cu phase diagram, an entirely f.c.c. structure was observed using XRD (Figure 4.3). Furthermore peaks were relatively broad indicating some compositional variation between f.c.c. grains or residual cold work damages. As mentioned previously an erroneous low intensity peak at ~68° is shown.

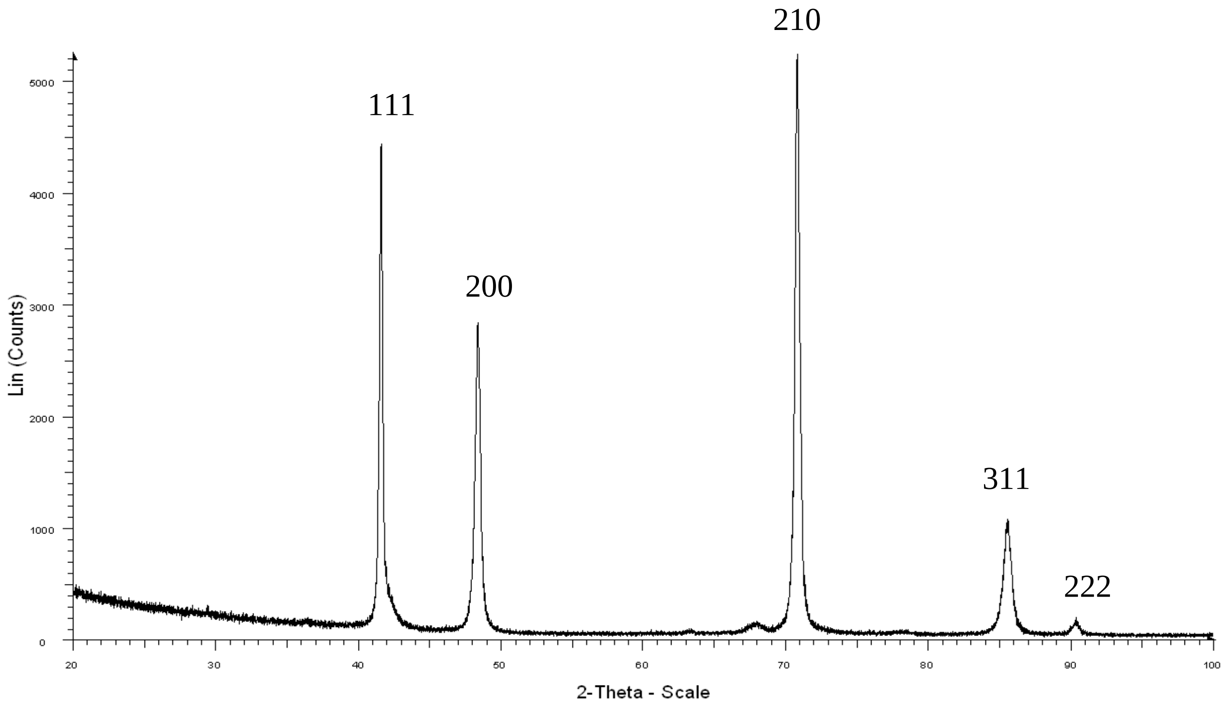

Figure 4.3 – An XRD trace of as received batch 2, revealing a fully f.c.c. structure.

XRD analysis of Batch 2 after heat treatment (500 ºC under vacuum for 72 hours) showed narrower peaks, compared to the as received sample, signifying better homogeneity in the structure. The spectra can be attributed to a mixed phase b.c.c./f.c.c. structure (Figure 4.4). The b.c.c. phase of the alloy appears to be strongly textured in the [110] plane, most likely due to residual rolling texture induced in the Johnson Matthey fabrication process. Topas analysis of the XRD spectra from the b.c.c. phase of the annealed alloy indicated an alloy composition of 47.76 at% Pd based on data of Figure 4.2. In addition Topas software analysis of the peak intensities for the f.c.c./b.c.c. phase balance showed 21.08% f.c.c. existed in the alloy, with a phase composition of 48.69 at% Pd. The other 78.92% of the alloyed formed by the b.c.c. phase has a composition of 47.51 at% Pd. Thus the composition calculated from XRD data is defined as 47.76 at% Pd.

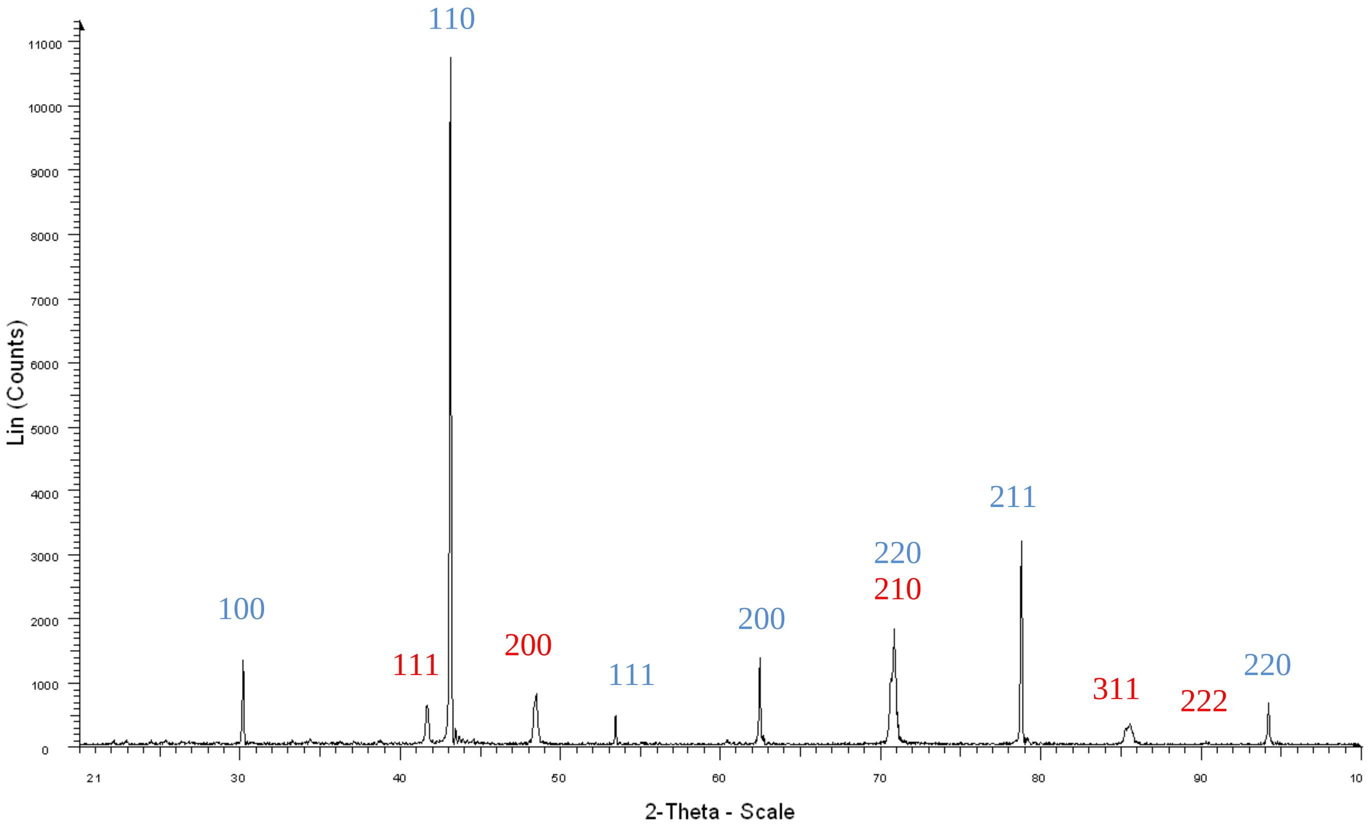

Figure 4.4 – An XRD trace of the alloy after heat treatment, showing mixed phase structure predominantly comprised of b.c.c. phase. F.c.c. peaks are highlighted in red and b.c.c. in blue.

Despite little evidence of contrast in the backscattered image (Figure 4.5) EDS analysis of batch 2 after the annealing treatment showed slight compositional deviations between areas of the alloy, Table 4.3. These deviations may arise from the existence of small f.c.c. grains nucleated in the material or minor inhomogeneity in the alloy.

Table 4.3 – Vacuum annealed EDS summary

Condition	Scan	At% Pd	Error	Average
Vacuum Annealed	1	46.80	0.23	47.38
	2	47.44	0.23	
	3	47.55	0.23	
	4	47.64	0.23	
	5	47.48	0.23	
	6	47.41	0.23	

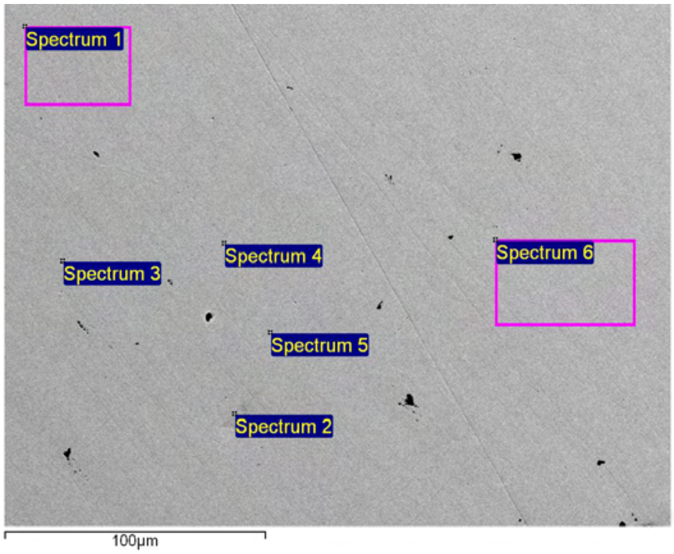

Figure 4.5 – A backscattered image of the alloy after heat treatment and the regions analysed using EDS

As the accuracy of the XRD results is thought to be greater than that of EDS and in-situ XRD measurements were also taken later in the work, the composition of batch 2 alloy used throughout this project is 47.76 at% Pd.

As may be seen in Figure 4.4 the XRD trace shows a mixture of f.c.c. and b.c.c. structures. Previous literature had also cited that no purely b.c.c. structure of ~47 at% Pd had been achieved by annealing without hydrogen present (Decaux). The annealing treatment of present work took place at higher temperatures than previous work, such as Decaux (250 ºC), and was left to cool slowly in order to give close to equilibrium conditions. This may indicate that the CALPHAD phase diagram proposed by Huang (Figure 2.8) is incorrect and that the β phase boundary is never fully b.c.c. at room temperature at this composition as shown by Subramanian and Laughlin (Figure 2.12). The phase transition to a fully f.c.c. structure for this alloy is expect to take place at approximately 550ºC, based on both the findings of both Subramanian and Laughlin and Huang.

4.1.3 Batch 1 – Nominal Composition of ~52 at% Pd

As this alloy was cast and then quenched prior to rolling an f.c.c. structure was expected. Using a micrometer the thickness of Batch 1 was found to be 102 μm (this value will be used later in calculating permeability). The surface condition appeared to be smooth, reflective and free from oxides.

XRD analysis was carried out on as received Batch 1 samples, which were found to have an f.c.c. structure as shown in Figure 4.6. Broad but well defined f.c.c. reflections only are present with no b.c.c. phase reflections indicating that the variations in composition must arise from compositional variations between f.c.c. grains. A low intensity peak at ~36º is an experimental anomaly. As with Figure 4.3, an extraneous low intensity broad peak at ~68º is shown.

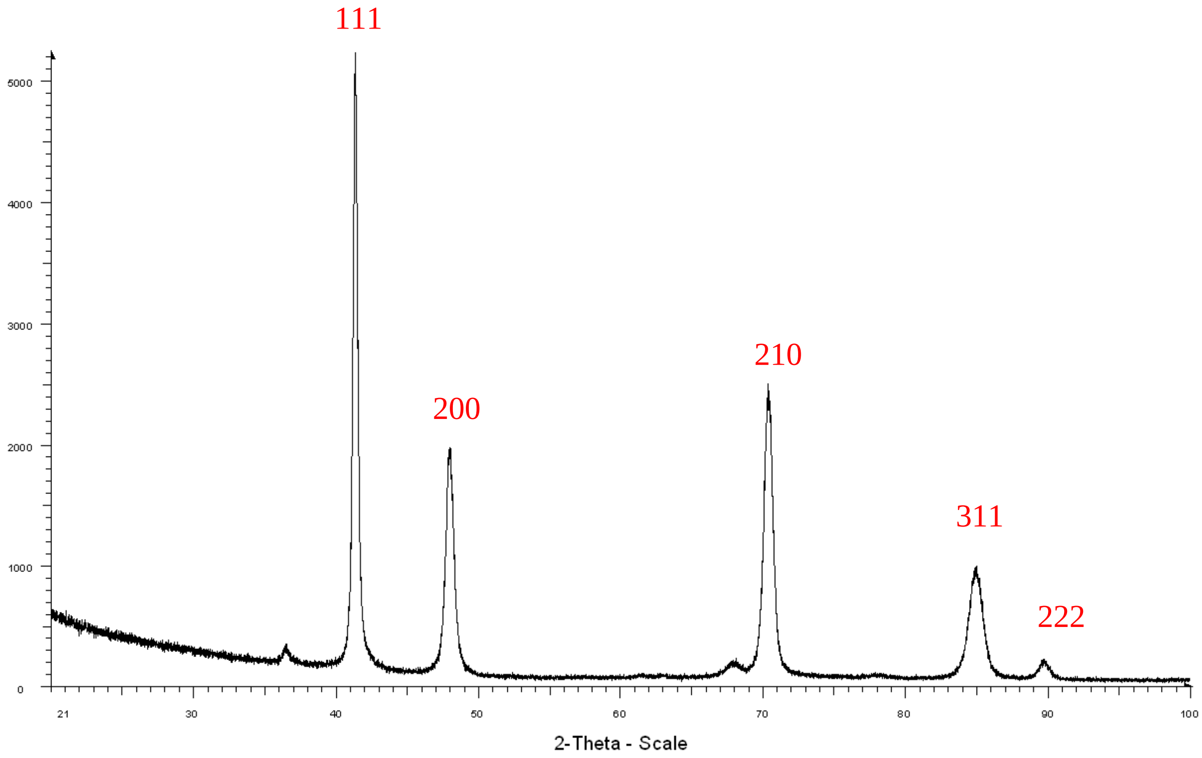

Figure 4.6 – XRD spectra for as received batch 1, showing broad f.c.c. peaks.

An XRD spectra of the batch 1 structure after homogenising heat treatment, 500 ºC under vacuum for 72hrs, was taken (Figure 4.7). Some b.c.c. phase was nucleated giving a mixed phase structure which exhibited narrower peaks indicating greater homogeneity of the f.c.c. and b.c.c. phases or a relaxation of cold work damage. Spectra were taken from both sides of the foil and exhibited similar peak positions and intensities.

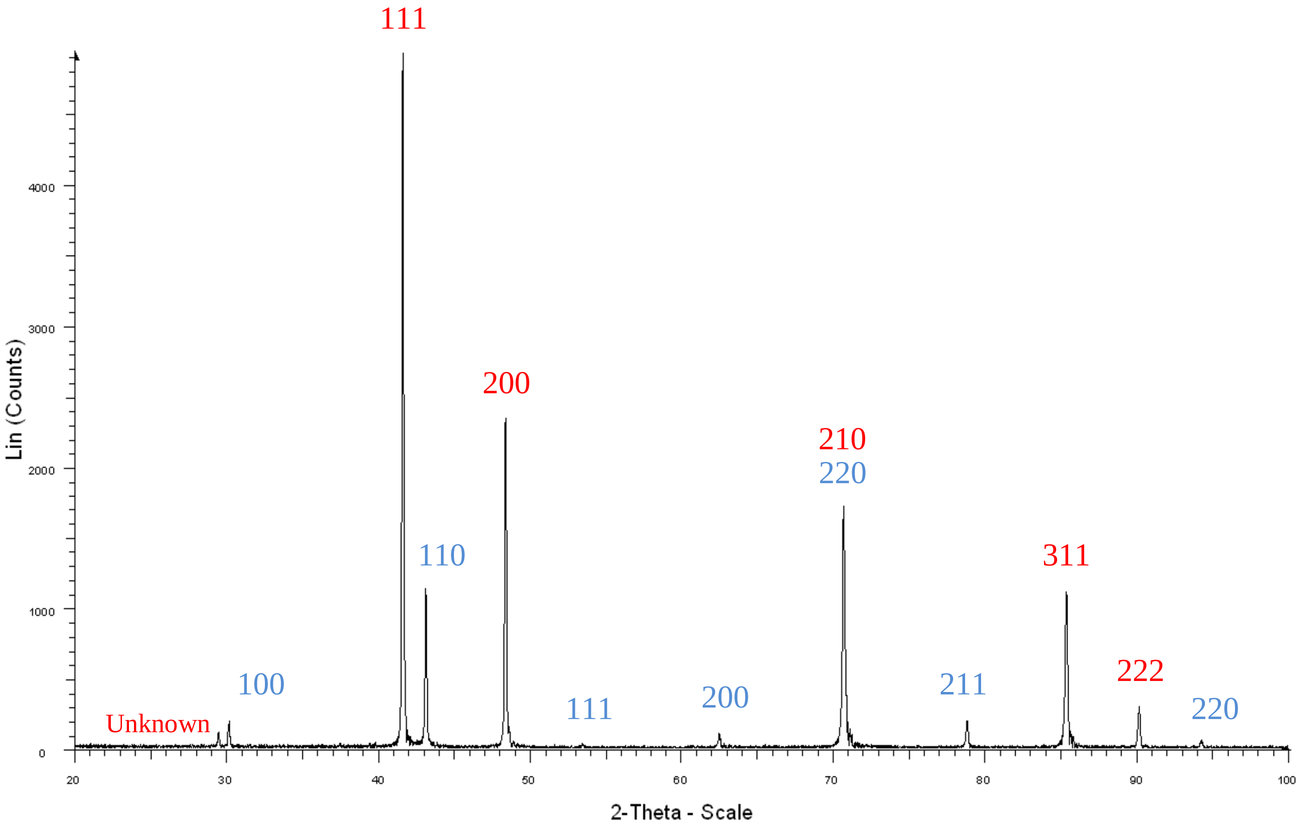

Figure 4.7 – An XRD trace of batch 1 after an annealing treatment at 500ºC for 72hrs under vacuum. A mixed phase structure is present. F.c.c. peaks are highlighted in red and b.c.c. in blue.

The lattice spacing values of f.c.c. and b.c.c. phases and the relative percentage of each phase in the alloy were calculated using Topas software. The b.c.c. phase was shown to have a lattice spacing of 2.97383 Å and constituted 13.25% of the alloys weight. The remaining 86.75% of the alloy was f.c.c. with a lattice spacing of 3.76972 Å. From Vegard's law compositions of 47.00 and 50.57 at% Pd have been calculated for the b.c.c. and f.c.c. phase respectively. The overall composition of the alloy from XRD spectra can hence be calculated to be 50.10 at% Pd.

EDS analysis after the annealing heat treatment of batch 1 showed a relatively even compositional range, with an average atomic % Palladium of 52.15, Figure 4.8. There is, however, still some variation in composition indicated by the results, although this may arise from the presence of both f.c.c. and b.c.c. grains in the sample. This average does not include the values from spectrum 4, which showed a large amount of carbon, attributable to the Bakelite into which the sample was set.

Table 4.4 – Vacuum annealed EDS summary

Condition	Scan	At% Pd	Error	Average
Vacuum Annealed	1	52.27	0.22	52.15
	2	52.78	0.22	
	3	51.85	0.22	
	5	51.70	0.22	

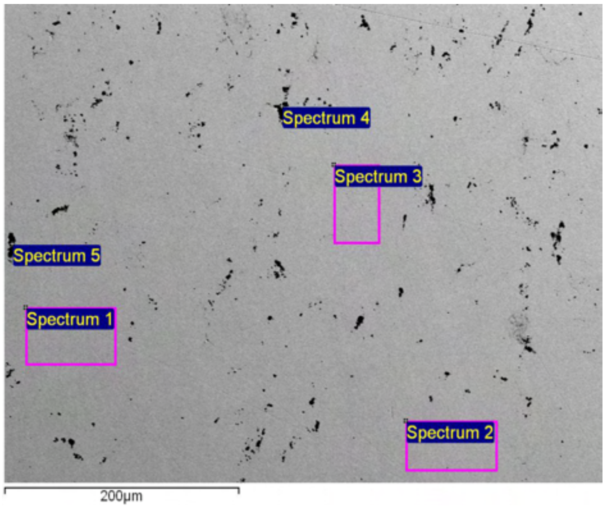

Figure 4.8 – Backscattered SEM image of vacuum annealed batch 1 and the areas at which spectrums were taken using EDS.

The data from XRD spectra and EDS give different compositions for the batch 1 alloy; 50.10 and 52.15 at% Pd respectively. Errors in the EDS readings could give a lower atomic percentage than predicted, but not as low as the value shown for XRD. Alternatively there may be some variation of composition through the thickness of the material which would explain deviation between the reading at the surface for XRD and of the bulk alloy for EDS. It has been decided that, for consistency, as XRD is the primary technique used in this work the value of 50.10 at% Pd will be used.

4.1.4 Batch 3 – Nominal Composition of ~60at% Pd

Visual inspection of the as-received batch 3 foil showed a brown discoloration that appeared to be an oxide layer. These were removed by etching in a solution of 25% HCl for one minute before the XRD spectra was taken (see Figure 4.9). The XRD spectra shows a fully f.c.c. structure with what is possibly a small residual film of Cu_2O, indicated by the blue lines, as identified by Topas. The presence of this oxide is particularly notable at the W, X and Z reflections (2θ values of 29º, 36° and 43º). Reflection Y (39º) did not appear to correspond to any oxide or b.c.c. phase material. It was decided that the batch 3 alloy would be etched after annealing in a solution of 50% HCl for 1 minute in order to ensure more complete removal of the oxide layer. After the annealing treatment, should the oxide still visibly remain, a further etching treatment (50% HCl) was carried. The thickness of the alloy was measured to be 33µm using a micrometer.

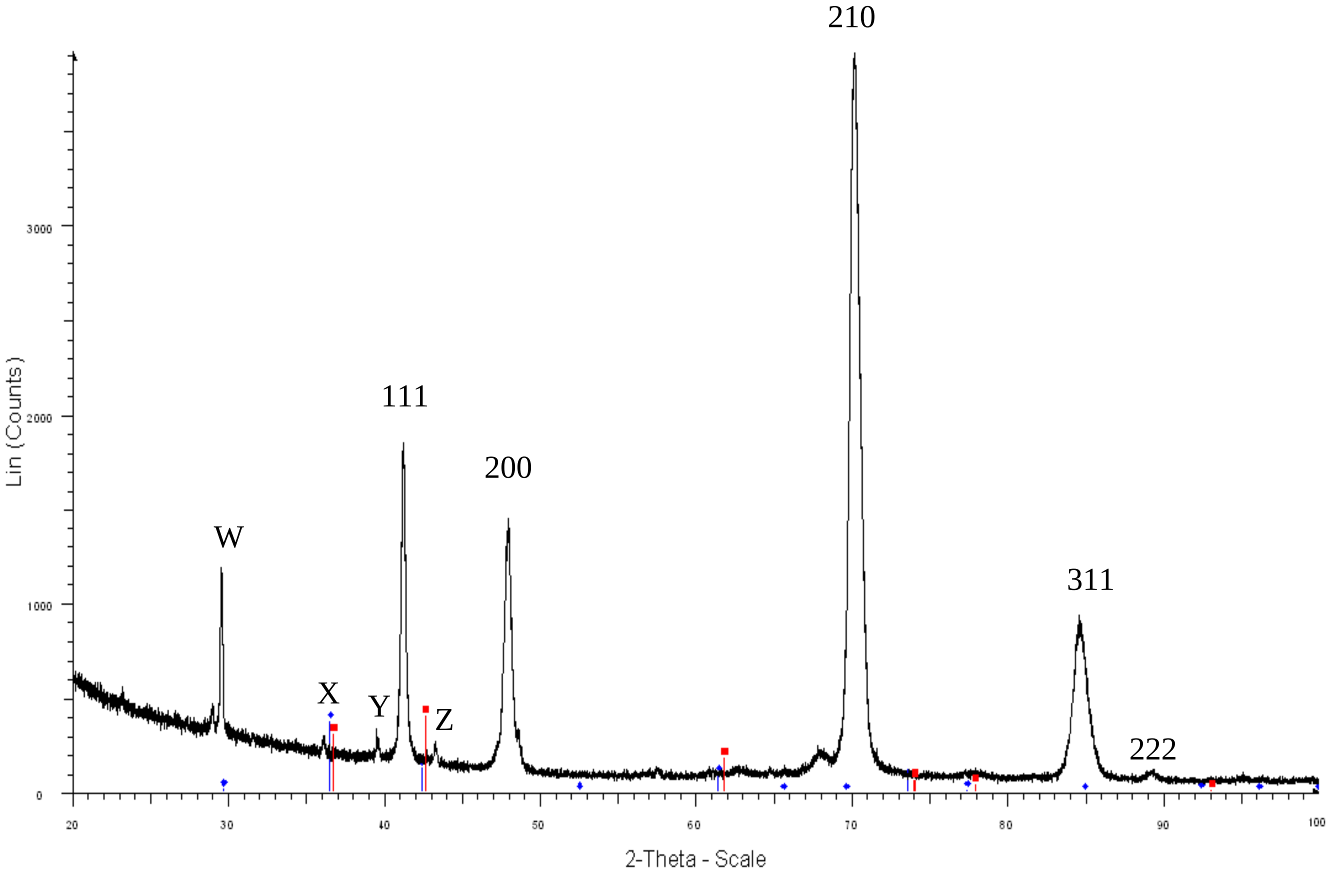

Figure 4.9 – XRD trace of batch 3 after etching in 25% HCl solution, prior to heat treatment, appears to possibly show a small amount of Cu_2O surface oxide.

XRD of annealed batch 3 samples etched in a solution of 50% HCl were also fully f.c.c. (Figure 4.10) despite cooling under equilibrium conditions. This indicates that the alloy lies outside the mixed phase boundary line. Each side of the foil was checked in this instance and for both side A (blue) and B (red) a fully f.c.c. structure was found. Analysis using Topas software attributed the small peak X (~29º), as identified by Topas, to Cu_2O surface oxides rather than a small presence of b.c.c. phase.

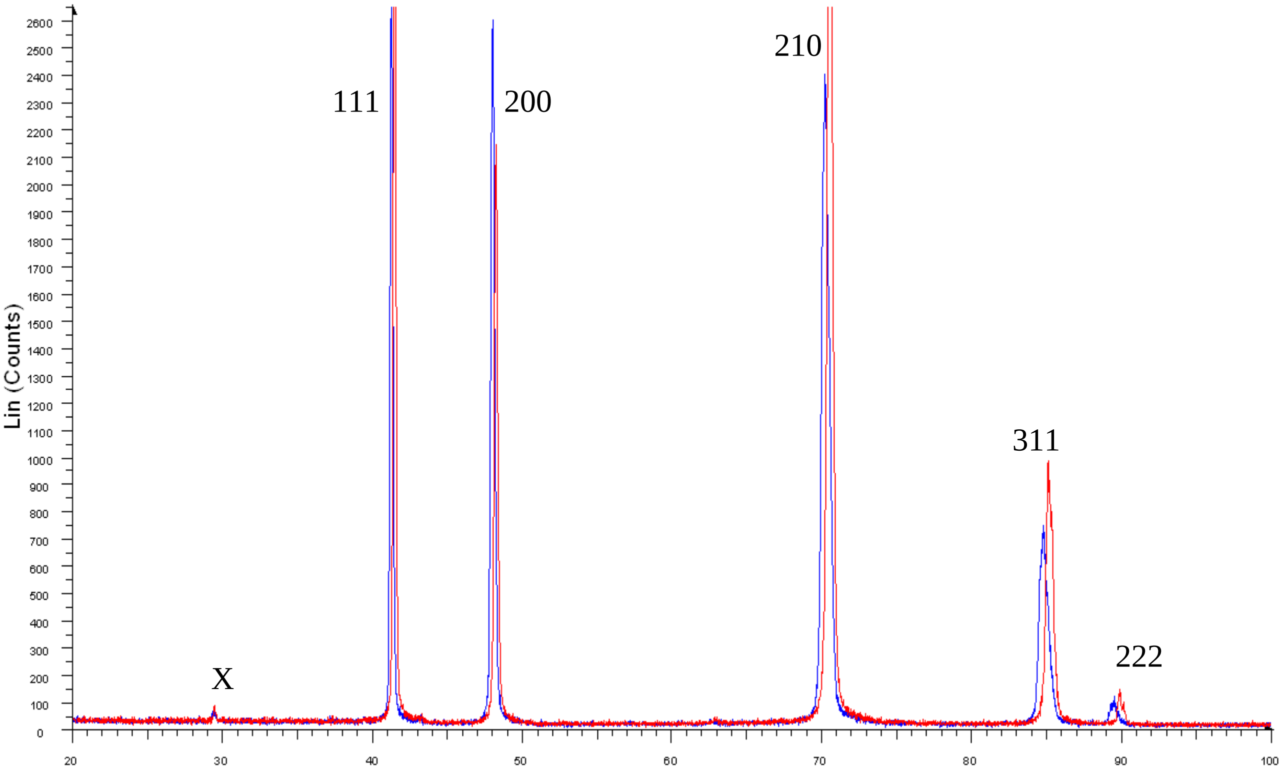

Figure 4.10 – Batch 3 after 50% etch in HCl after annealing largely showing the removal of oxides of from side A (blue) and side B (red).

Topas software was also used to accurately calculate the lattice parameter of the f.c.c. phase on either side of the alloy etched in 50%HCl. The composition was found to be different; atomic % Pd 52.24 and 56.48 for sides A and B respectively.

EDS analysis of alloy after exposure to the 50% HCl and heat treatment, under conditions described previously, showed a broad range of compositions, Figure 4.11 and Table 4.5.

Table 4.5 – Vacuum annealed, after 50% HCl etch, EDS summary.

Condition	Scan	At% Pd	Error	Average
Vacuum Anneal – 50% Etch	1	56.17	0.32	57.16
	2	56.98	0.32	
	3	55.83	0.32	
	4	55.40	0.32	
	6	62.11	0.32	
	7	57.43	0.32	
	8	57.07	0.32	
	9	56.34	0.32	

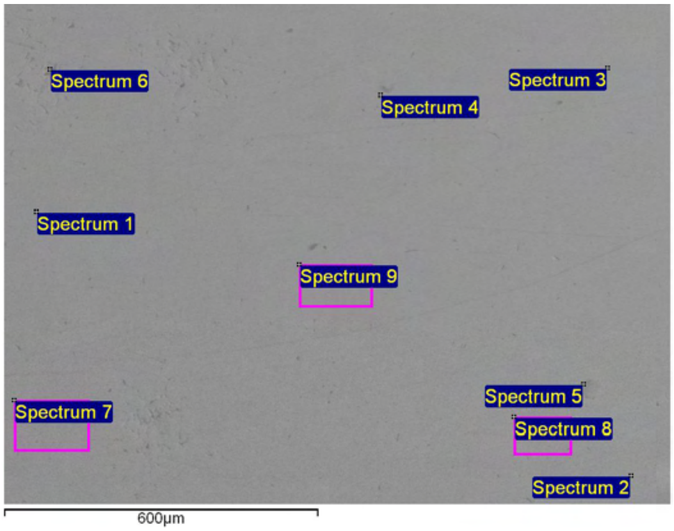

Figure 4.11– A backscattered image of as received structure of batch 3 and the regions where EDS was carried out.

4.1.5 Summary - Composition and Crystal Structure

The composition of each of the alloys Batches 1, 2 and 3 is plotted on the phase diagrams derived by Huang using CALPHAD and Subramamian and Laughlin from experimental data (Figure 4.12). Clearly there are significant discrepancies between the two phase diagrams. Of particular interest is Batch 2, around the composition associated with the high hydrogen permeability peak summarised in Figure 2.9. In one instance the alloy lies directly on the phase boundary line (Subramamian and Laughlin) and in the other (Huang) inside the β phase field. Also of interest is Batch 3 which has been shown to have a fully f.c.c. structure after annealing. The structure of Batch 3 is in keeping with the phase diagram of Subramanian and Laughlin rather than that of Huang which shows a mixed phase structure at this composition.

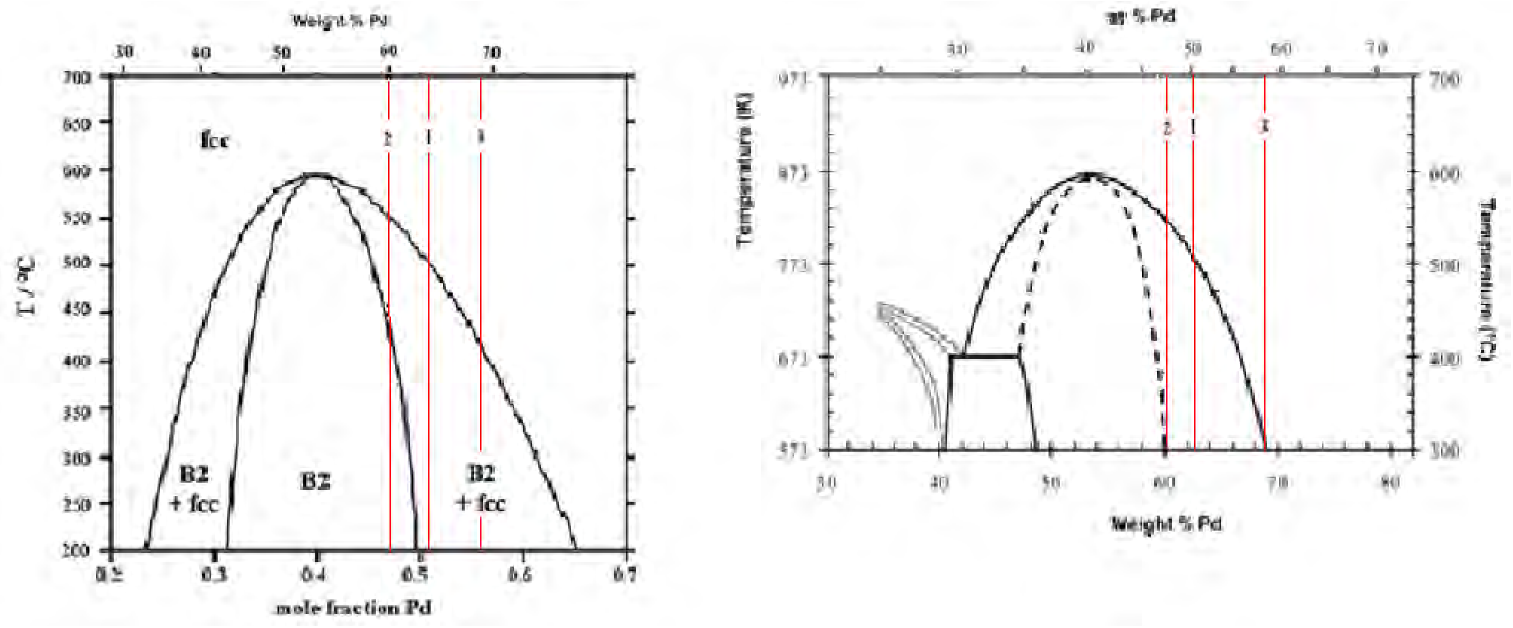

Figure 4.12 – Where alloys 1,2 and 3 lie with respect to the phase diagrams of Huang using CALPHAD software (left) and Subramamanian and Laughlin from experimentation (right).

It was decided that both Batches 1 and 2 alloys would be used for DSC, in-situ XRD and permeability experiments as they appear to exhibit a uniform crystallographic structure.

Although Batch 3 exhibited some compositional stratification, leading to variability in the results it produces, it may still be used. The penetration depth of Cu Kα X-rays is ~10µm but the intensity of near surface reflections will be stronger. Thus, if the same side of the sample was analysed each time during in-situ measurements, the results produced should be consistent for a single composition. For this work the more Pd-rich side of the alloy (B) was chosen as this phase lies outside the mixed phase region, according to the Subramamian and Laughlin diagram, so any b.c.c. phase nucleated would be as a result of a phase boundary shift. DSC experiments consider the alloy in bulk and compositional variation would make results difficult to interpret hence these tests were not carried out. Hydrogen permeability tests were carried out on Batch 3 alloy foils but it was ensured that the Pd-rich side (B) of the membrane always faced the upstream (10bar) side.

It should be noted that batches will now be referred to by their elemental composition i.e. $Pd_{50.10}Cu_{49.90}$, $Pd_{47.76}Cu_{52.24}$ and $Pd_{\sim56.5}Cu_{\sim43.5}$ for Batches1, 2 and 3 respectively.

4.2 The Effect of Hydrogen on Structure – In-Situ XRD and DSC

The primary experimental technique used in this section is XRD use for characterisation of the annealed Pd-Cu foils at high temperatures in a hydrogenated atmosphere.

In-situ XRD measurements performed using the Anton-Parr cell occasionally exhibited peaks which could not be attributed to Pd-Cu or any relevant oxides or hydrides. These reflections were thought to be due to foils incomplete covering the sampling area allowing the alumina sample platform and impurities on it to be exposed to the X-ray beam. During in-situ measurements at high temperatures sample deformation due to the relaxation of residual stresses. Deformation will have greatest affect on the accuracy of results at the end of the thermal cycle.

4.2.1 In-Situ XRD Analysis of $Pd_{47.76}Cu_{52.24}$

XRD scans of $Pd_{47.76}Cu_{52.24}$ at a range of temperatures under inert (He) and hydrogenated atmospheres were taken as described in Section 3.2.1. For each XRD spectrum the weight percentage of b.c.c. phase was calculated using Topas software, by means of establishing phase balance in the system. The XRD data for $Pd_{47.76}Cu_{52.24}$ in different atmospheres (under10 bar hydrogen and 1 bar helium) are shown in Figure 4.13 and Figure 4.14 respectively.

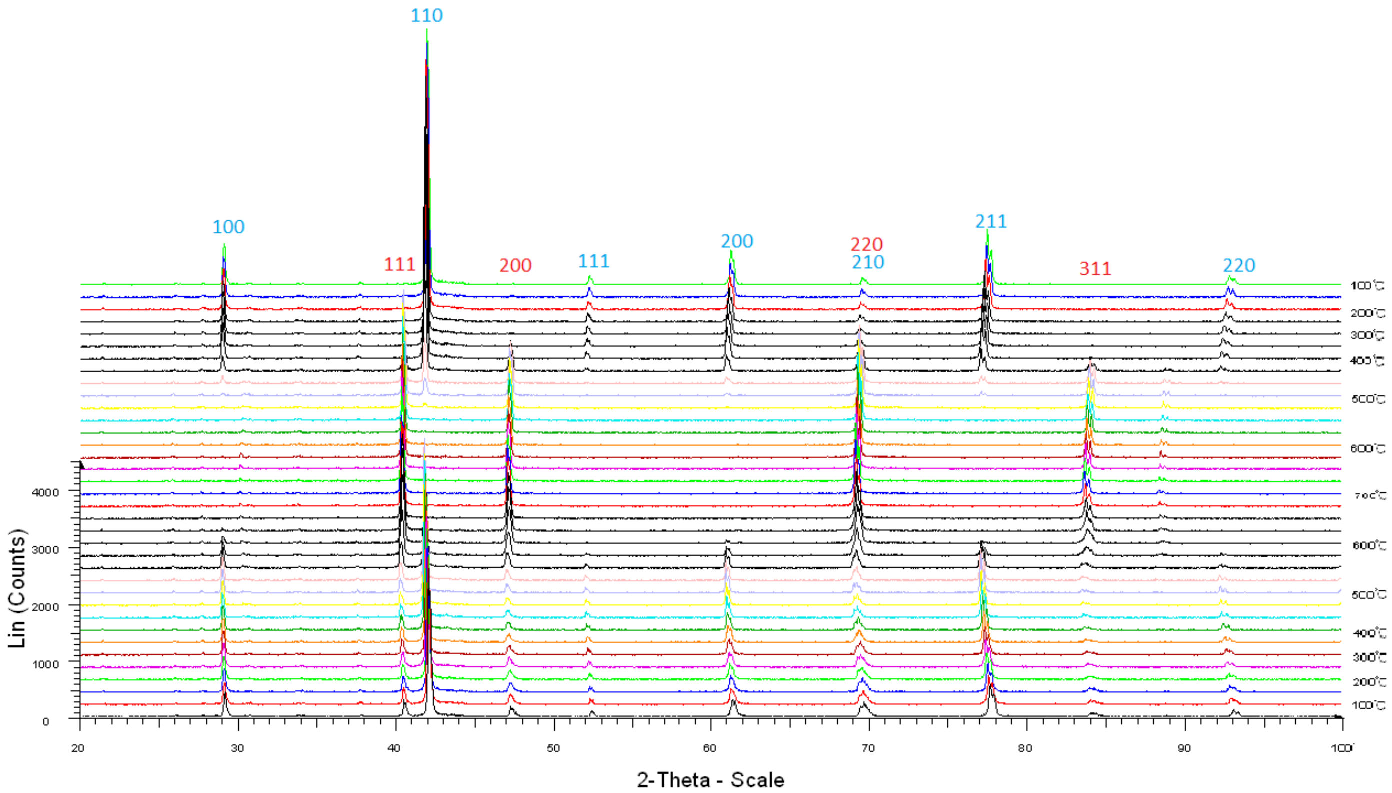

Figure 4.13 – XRD spectra of $Pd_{47.76}Cu_{52.24}$ heated from room temperature to 700°C and back, under an atmosphere of 10bar hydrogen.

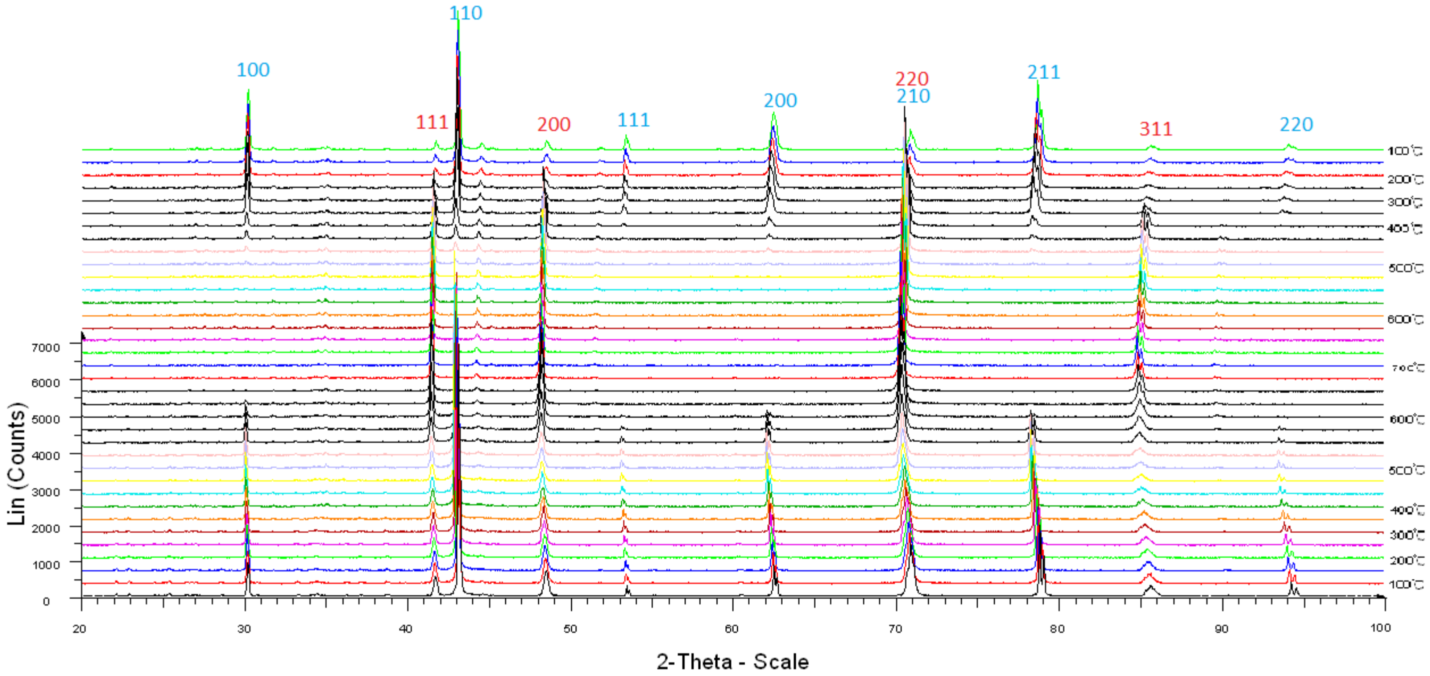

Figure 4.14 – XRD spectra of $Pd_{47.76}Cu_{52.24}$ heated from room temperature to 700°C and back, under an atmosphere of 1bar helium.

The relative phase proportions, in terms of weight%, can be calculated from the XRD spectra of Figure 4.13 and Figure 4.14 using Topas software. Figure 4.15 shows the results for $Pd_{47.76}Cu_{52.24}$ heated in a helium atmosphere.

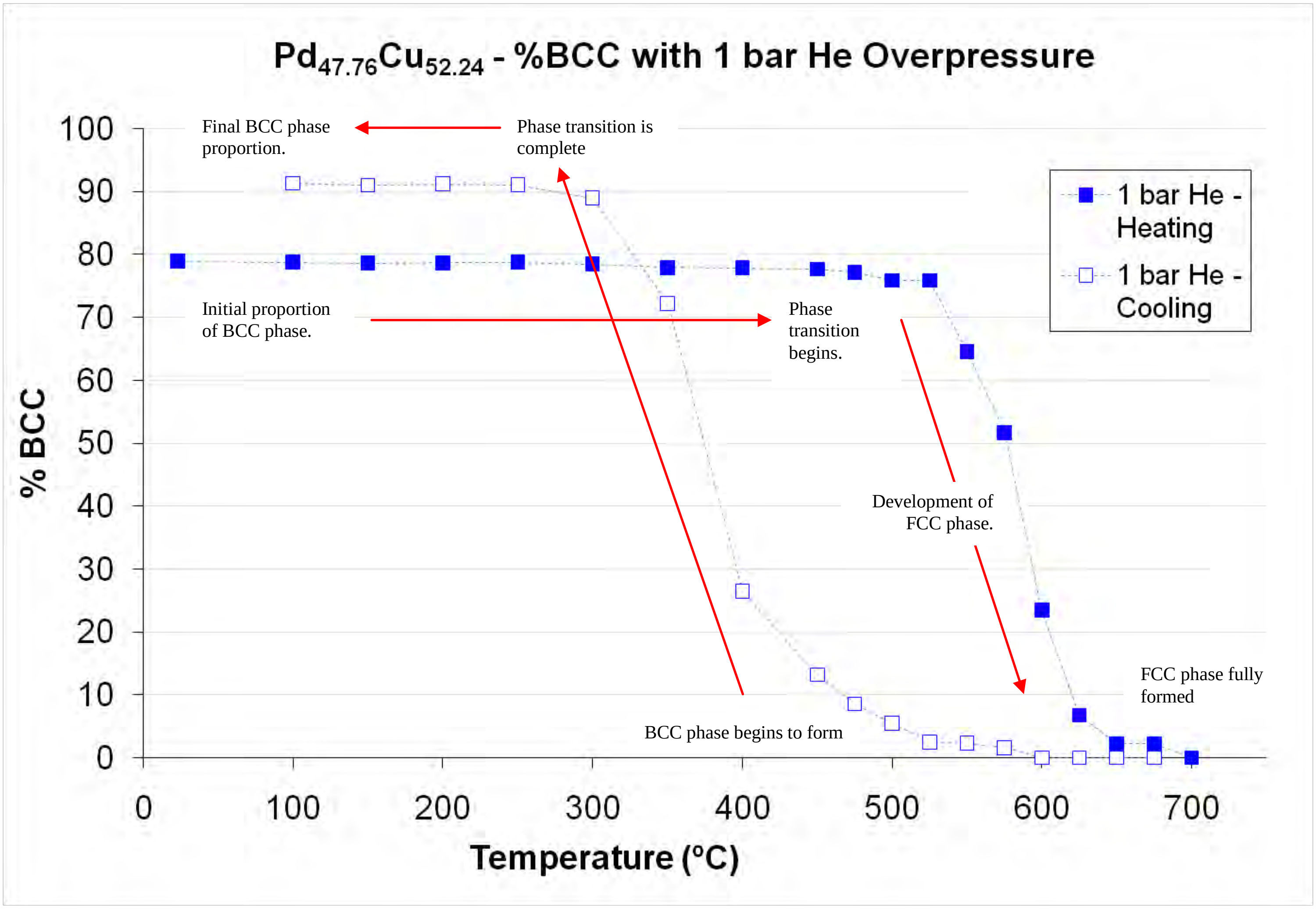

Figure 4.15 – A summary of the proportion of b.c.c. phase, in weight%, at various temperatures in both heating and cooling; using Topas analysis of In-Situ XRD spectra.

The heating cycle affects the proportion of phases; this is particularly evident in cooling where the onset temperature of b.c.c. phase nucleation occurs at lower temperatures than heating. A full summary of results is shown in Figure 4.16.

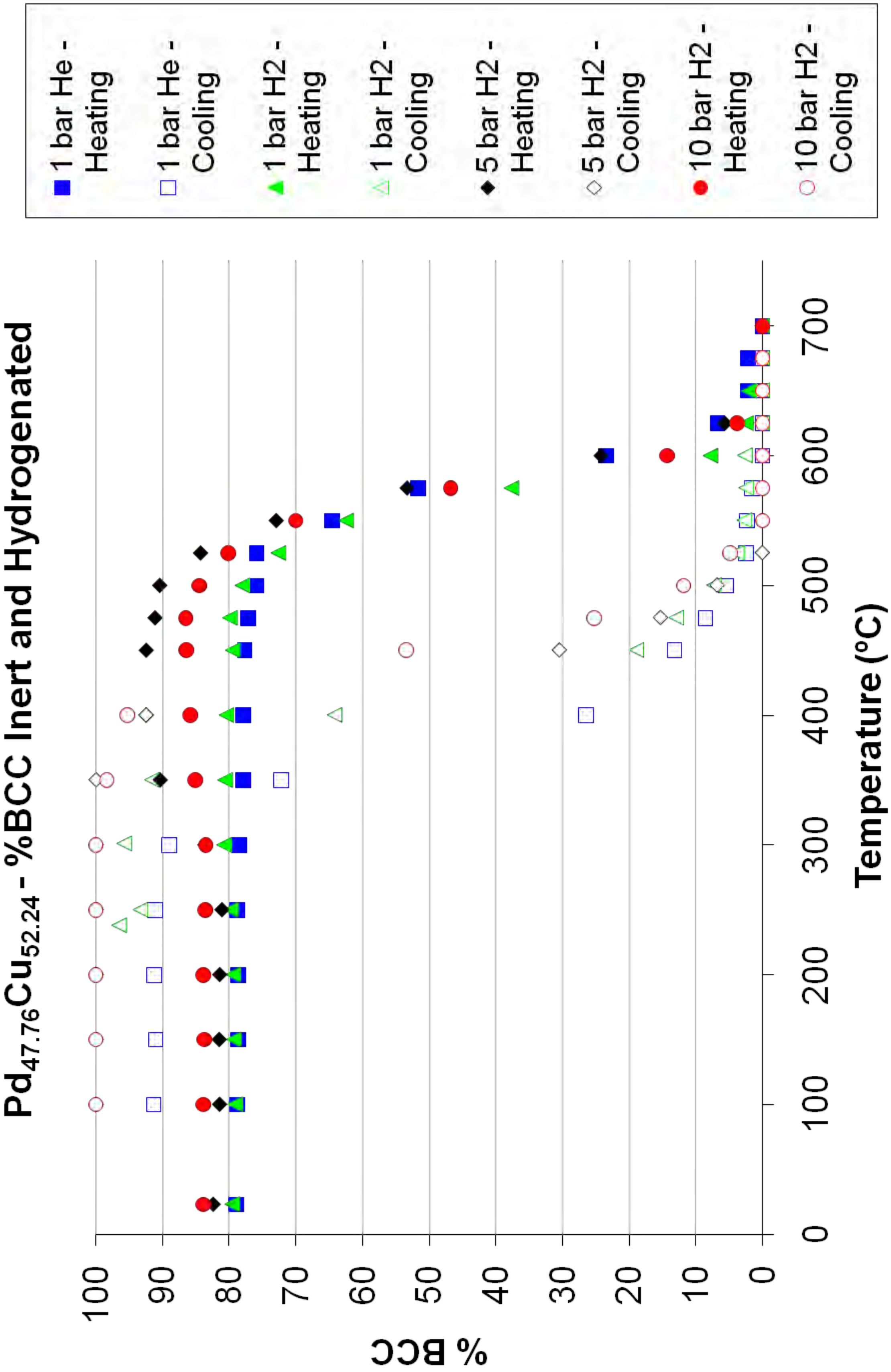

Figure 4.16 – The percentage b.c.c. of $Pd_{47.76}Cu_{52.24}$ (Batch 2) up to 700 °C under various atmospheric conditions.

Despite being cut from adjacent regions of the $Pd_{47.76}Cu_{52.24}$ foil XRD samples yielded slightly different starting amounts of b.c.c. phase. This was attributed to experimental error relating to both the diffractometer and the Topas analysis software.

As temperature increased XRD under 10 bar hydrogenated samples showed an increase in the percentage of b.c.c. phase present at temperatures >300 ºC prior to transition to a fully f.c.c. structure (~600 °C). This may perhaps suggest a non-equilibrium starting condition or more likely, as the effect is not shown for samples heated in helium gas, a shift in the boundary line leading to varied composition through the lever rule. Varying amounts of b.c.c. phase prior to phase transition made an accurate comparison of results more difficult, as dissimilar rates of transformation may result in the same phase proportions, for example. In contrast under He atmosphere the b.c.c. phase content was not developed.

The onset and completion temperatures of phase transformations are of particular use in establishing the position of the phase boundary in temperature/ composition diagrams. A summary of the phase transition onset temperatures is given in Table 4.6.

Table 4.6 – The b.c.c to f.c.c. phase transitions of $Pd_{47.76}Cu_{52.24}$ (batch 2) under a range of atmospheric conditions.

Atmospheric Condition	Transition Onset Heating (ºC)	Transition Completion Heating (ºC)	Transition Onset Cooling (ºC)	Transition Completion Cooling (ºC)
10 bar H_2	475-500	625-650	550-525	400-350
5 bar H_2	475-500	625-650	525-500	400-350
1 bar H_2	500-525	600-625	525-500	350-300
1 bar He	525-550	625-650	525-500	350-300

From the onset temperatures it can be seen that, for $Pd_{47.76}Cu_{52.24}$, the presence of hydrogen reduces the transition temperature from mixed phase to fully f.c.c. Upon cooling, greater pressures of hydrogen gave higher onset and completion temperatures. Hydrogen was thus shown to shift phase boundary line, towards the Pd-rich end, in line with early results of Piper. Distinct hysteresis is shown in the phase transition points between heating and cooling cycles; this is in line with findings from Goldbach.

Fully b.c.c. phase was developed under 5 and 10 bar hydrogen overpressures when cooled from 700 °C. In contrast under inert He conditions fully b.c.c. phase was not developed, as was noted previously by Decaux for a similar alloy composition. Unfortunately spectra at low temperatures of the 1 bar hydrogen scan could not be recorded due to a system error; so a full comparison cannot be drawn.

It has been shown that interstitial hydrogen present in f.c.c. crystal structures will reduce the enthalpy of formation of b.c.c. phases (Huang) which may be the reason that a fully b.c.c. phase is not made. It may also be the case that the phase boundary line is shifted in the presence of hydrogen and this accounts for the observation of different structures when cooling in an inert atmosphere (Piper).

4.2.2 In-Situ XRD Analysis of $Pd_{50.10}Cu_{49.90}$

As with $Pd_{47.76}Cu_{52.24}$ XRD spectra were taken under various hydrogen and helium overpressures while heating up to 700 ºC and in cooling back to room temperature. The results of spectra taken under 10bar hydrogen and 1bar helium are shown in Figure 4.17 and Figure 4.18 respectively.

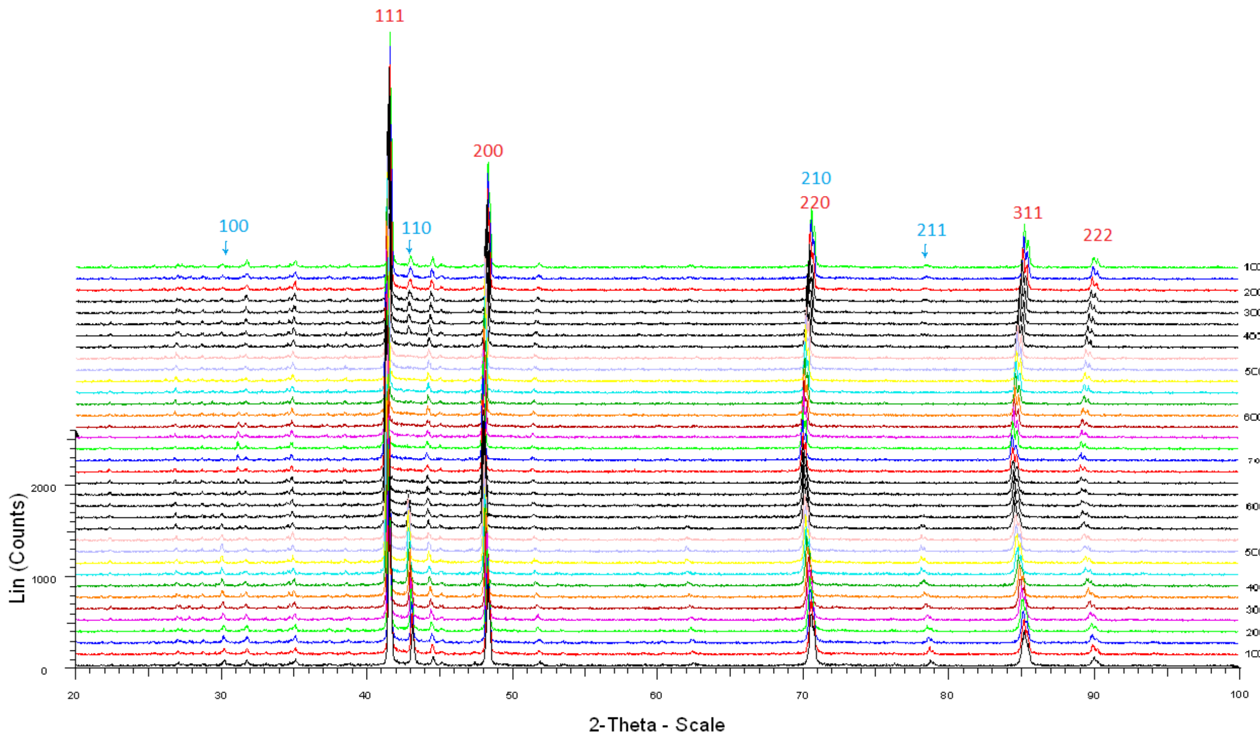

Figure 4.17 – XRD spectra of $Pd_{50.10}Cu_{49.90}$ heated from room temperature to 700°C and back, under an atmosphere of 10bar hydrogen.

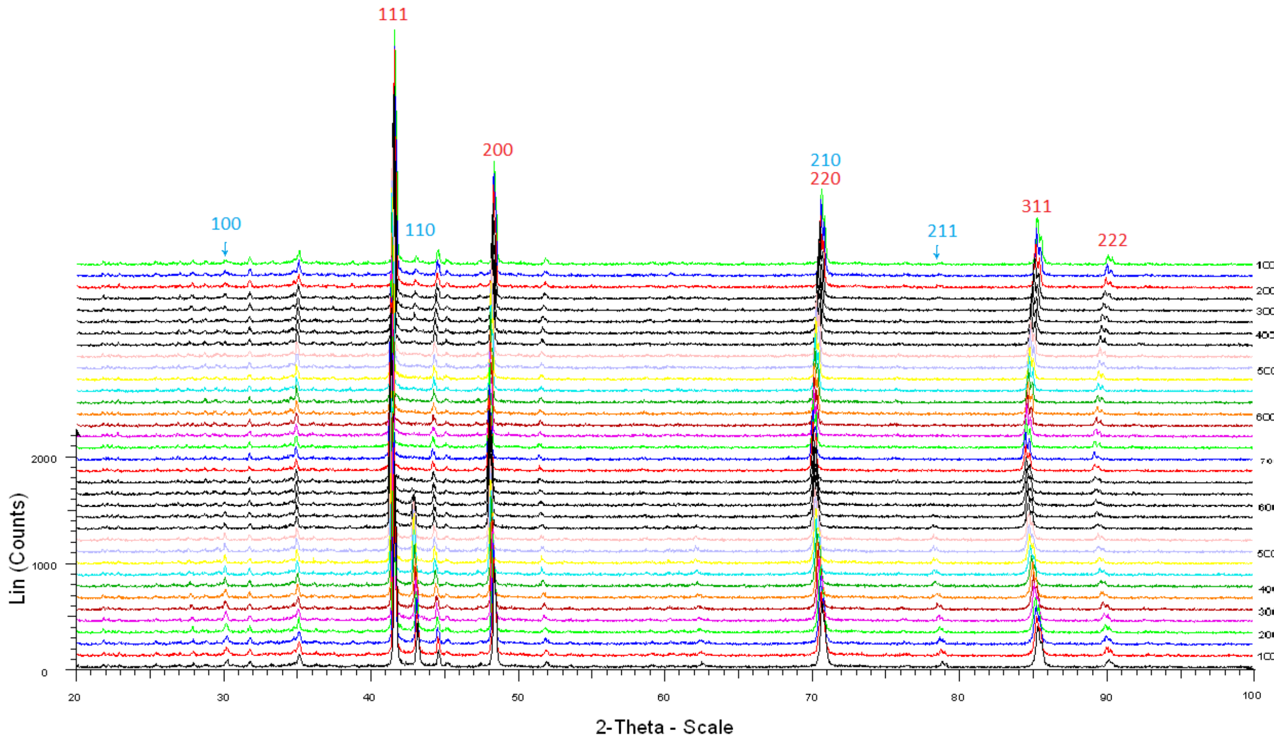

Figure 4.18 – XRD spectra of $Pd_{50.10}Cu_{49.90}$ heated from room temperature to 700°C and back, under an atmosphere of 1bar helium.

Topas analysis was carried out for each XRD spectra detailing the proportion of b.c.c. phase in the alloy, shown Figure 4.19.

Different proportions of b.c.c. phase were initially calculated despite all samples being cut from adjacent regions and annealed at the same time. As with $Pd_{47.76}Cu_{52.24}$ an error of +/-3.5% is assumed for this work. There appeared to be two different initial proportions of the b.c.c. phase ~12% and ~16%; within the experiment error. Compositional variation across the material may be the reason for the existence of two seemingly different phase proportions. However, XRD spectra of either side of the sample gave matching traces, thus the error is thought to stem from experimental XRD variables such as; non uniform starting height of the sample, bent or warped samples, inlet of gas moving the sample on the supporting alumina platform or errors in Topas software.

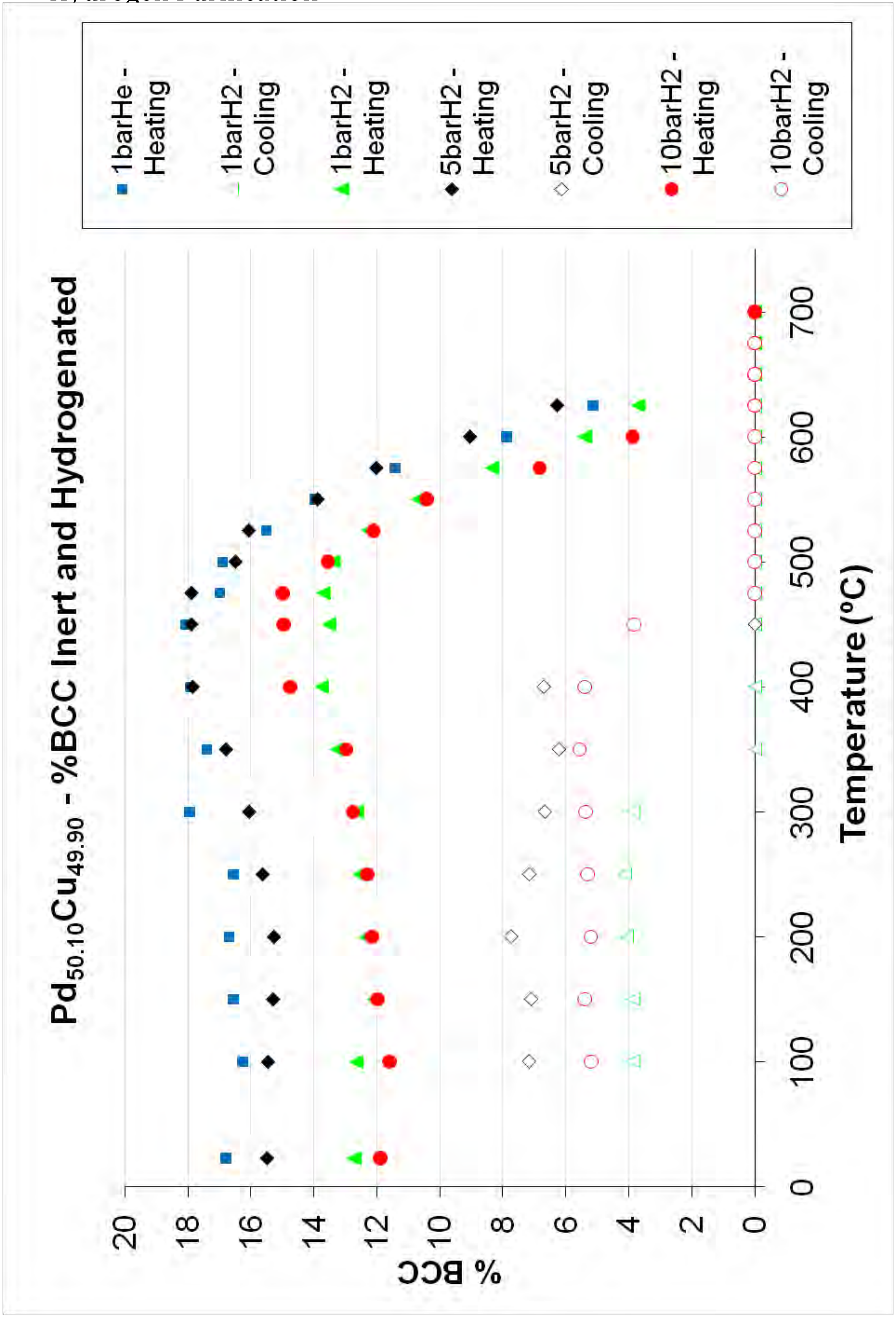

Figure 4.19 – The percentage b.c.c. of $Pd_{50.10}Cu_{49.90}$ (batch 1) up to 700 ºC under various atmospheric conditions.

A common feature of all $Pd_{50.10}Cu_{49.90}$ alloys under all experimental conditions was growth of the b.c.c. phase prior to the f.c.c. transition which complicated the interpretation of data. This probably indicates that cooling during the annealing process was not carried out under equilibrium conditions. Thus, the heating cycles of the XRD scans are less reliable than the cooling cycles for deriving compositional data.

Varying starting contents of b.c.c. phase may also affect the rate of transition making comparison more difficult. However, the onset and completion temperatures are still useful and are summarised in Table 4.7.

Table 4.7 – The phase transitions of $Pd_{50.10}Cu_{49.90}$ (batch 1) under a range of atmospheric conditions.

Atmospheric Condition	Transition Onset Heating (ºC)	Transition Completion Heating (ºC)	Transition Onset Cooling (ºC)	Transition Completion Cooling (ºC)
10 bar H_2	475-500	600-625	475-450	450-400
5 bar H_2	475-500	625-650	450-400	450-400
1 bar H_2	500-525	625-650	350-300	350-300
1 bar He	450-525	625-650	N/A	N/A

During heating the effect of hydrogen on the observed crystal structure appears to be negligible. In contrast the transformation under helium overpressures does not have a clearly defined starting point and could vary between 450 and 525 ºC. Variations of weight percentage b.c.c. phase between samples measured in hydrogen are within the experimental error of +/-3.5%; completion of the b.c.c. to f.c.c. phase transformation appears to take place at a similar temperature. A pressure of 10bar hydrogen may accelerate the rate of the phase transformation process, in that it appears to occur more rapidly than at lower pressures.

Phase transformations occurred at significantly lower temperatures in the cooling cycle, in line with the results of Goldbach, and the present work measured for Pd-47.3at%. The effect of hydrogen pressure was also more obvious in cooling. The temperature of onset and completion of the transformation was greater for higher pressures of hydrogen. From the phase diagram of Huang, Figure 4.12, it would be expected that b.c.c. phase is nucleated; however with a helium overpressure no b.c.c. phase was developed. In contrast, annealing of the as received $Pd_{50.10}Cu_{49.90}$ alloy with a fully f.c.c. structure, for 72hrs at 400 ºC in an inert atmosphere, had yielded some b.c.c. phase. The cooling rate for in-situ XRD experiments was 2 ºC per minute accompanied by dwell times of 20 minutes in which the XRD spectra were take. This is faster than the cooling from annealing of as received f.c.c foils. It seems likely that the cooling rate was too rapid to allow the b.c.c. phase to nucleate as opposed to a shift in the mixed / b.c.c. phase boundary. The presence of hydrogen clearly promotes the formation of b.c.c. phase, probably by reducing the enthalpy of formation, as noted by Huang.

4.2.3 In-Situ XRD Analysis of $Pd_{\sim 56.5}Cu_{\sim 43.5}$

XRD samples were taken on side B only which has a composition of approximately 56.5 at % Pd. XRD measurements take values from a depth of ~10µm and reflections will be more intense at the surface hence measurements taken from the same side in each case will reduce the effects due to variations in phase balance across the alloy width.

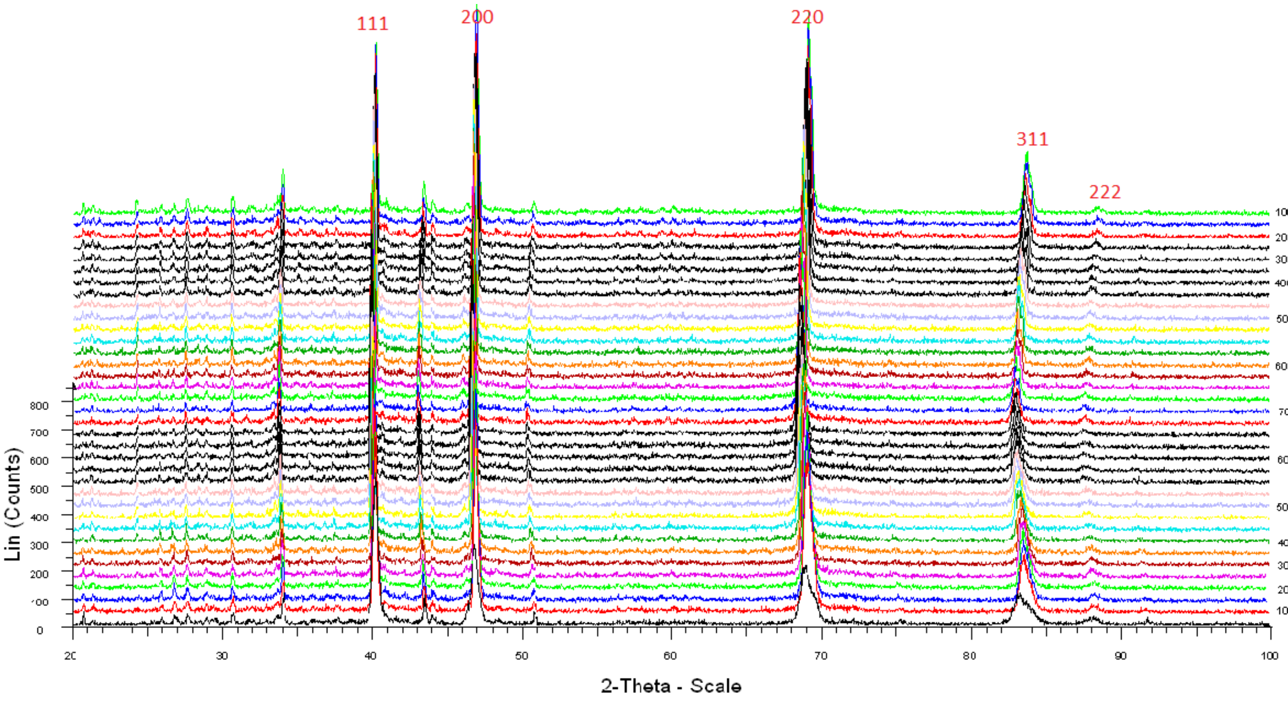

Figure 4.20 – XRD scans of $Pd_{\sim 56.5}Cu_{\sim 43.5}$ (batch 3) heated and then cooled to a temperature of 700 ºC under 10bar pressure.

Examination of the XRD spectra for each of these alloys did not show the presence of any b.c.c. phase at any stage under both inert and hydrogenated conditions. Minor peaks in positions which might have been attributed to the b.c.c. phase did not show any variation in peak height with temperature. This suggests that these small peaks more than likely arise from the alumina platform, or impurities present in it. Figure 4.20 shows XRD scans over a wide range of temperatures under 10 bar pressure. Other scans were similar and are shown in the appendix 7.1.

The reliability of the XRD captured later in the cycle (i.e. the cooling cycle) may be questionable as upon removal the foil sample was found to be bent and no longer lying flat on the sample platform; meaning that reflections at the latter stages of the experiment are likely to have been influenced. However, the spectra will still be valid for calculating the phase balance.

In relation to the Pd-Cu phase diagram side A of the alloy ($Pd_{\sim 56.5}Cu_{\sim 43.5}$) appears to maintain a fully f.c.c. structure throughout all temperatures, implying that the alloy composition lies outside of the mixed b.c.c./f.c.c. phase region. This is in accordance with the phase diagram presented by Subramanian and Laughlin, Figure 2.12, rather than the CALPHAD generated diagram, Figure 2.8 (Huang). According to the Pd-Cu phase diagram of Huang for a $Pd_{\sim 56.5}Cu_{\sim 43.5}$ alloy significant amounts of the b.c.c. phase should have been observed at temperatures below 400 °C.

4.2.4 DSC Results

DSC tests were deemed unreliable due to inconsistent results. These results are not used for interpretation of the Pd-Cu-H ternary alloy system. A summary of the principle reasons for not including the DSC data is given in the appendix 7.2.

4.3 Hydrogen Permeability Measurements

Hydrogen permeability tests were performed on all alloys over a range of pressure gradients and temperatures. Pressure on the upstream side of the membrane was maintained at 10bar, on the downstream side the pressure was set at 1, 3 or 5 bar. The phase balance of the Pd-Cu alloy on the upstream side of the membrane will replicate effects seen for in-situ XRD using a hydrogen overpressure of 10bar. Similarly membrane tests with 1 or 5 bar downstream pressure will be comparable to in-situ XRD measurements at 1 or 5bar hydrogen overpressure, while 3 bar downstream pressure will have a phase balance somewhere between 1 and 5 bar.

Using the mass flow controller the amount of hydrogen gas which passes through the membrane is measured. The measurement is taken at a predetermined frequency of time intervals time with the membrane temperature also recorded at this time. Downstream pressure is kept constant by the back pressure regulator. Hydrogen flux J may be calculated taking the measured downstream flow (ml.min^{-1}) and dividing by the membrane area (2.5447cm^{2}). As the mass flow controller was calibrated for nitrogen it was recommended by the manufacturer to multiply by M1 (1.008) to convert to hydrogen. However, it was found (Fletcher Private Communication) that multiplying by a further factor M2 (1.045) gave more accurate results. After using the conversion factor results were given in ml.cm^{-2}.min^{-1} this is converted to mol.m^{-2}.s^{-1} by multiplying by a factor of 0.0074405 (equation 4.1). Then, using equation 4.2$\emptyset = \frac{\boldsymbol{Jt}}{\boldsymbol{Pi^n - Pii^n}}$

Equation 4.2, rearranged from equation 2.7, the permeability can be calculated.

$$\boldsymbol{J = \left(\frac{DSF * M1 * M2}{A}\right) * U}$$ **Equation 4.1**

$$\emptyset = \frac{\boldsymbol{Jt}}{\boldsymbol{Pi^n - Pii^n}}$$ **Equation 4.2**

J – Hydrogen flux (mol.m^{-2}.s^{-1})

DSF – Measured downstream flow value (ml.min^{-1})

M1 – Manufacturers recommended hydrogen conversion factor (1.008)

M2– Empirically calculated additional hydrogen conversion factor (1.045)

A – Membrane area (mm^{2})

U– Unit conversion factor (0.0074405)

t– Membrane thickness

Pi– Upstream pressure

Pii– Downstream pressure

n– 0.5

4.3.1 Permeability Test Details

Earlier experiments on Pd-Cu membranes showed that at elevated temperatures the pressure differential across the membrane led to membrane failure (Fletcher Private Communication). Furthermore the pressure induced ‘doming’ of the membrane prior to failure leading to a reduction of the thickness through which hydrogen will permeate hence effective reaction area is increased leading to potential miscalculations of permeability values. To prevent these effects a macro-porous stainless steel disc was rested on the downstream side of the membrane (Figure 3.2). The support structure was not welded or brazed to the membrane so no intermediate crystal structures were formed. Pores in the support structure had an average diameter of 1μm. Flow tests in the absence of a membrane showed that the supporting material had no effect on hydrogen flow.

Failure of unsupported membranes was common (Fletcher Private Communication), at high temperatures and pressures, and generally came about due two factors acting in conjunction with one another: i) Excessive deformation of membranes in combination with lattice expansion upon formation of f.c.c. phase. ii) Generally failure occurred parallel to surface topography which had been induced by the rolling process.

4.3.2 Preliminary Hydrogen Permeability Measurements

The general shape of curves for hydrogen permeability against temperature during thermal cycling for Pd-Cu b.c.c. alloys using a for a system configuration of 10bar upstream and 1 bar downstream pressure, is shown, Figure 4.21. The increase in permeability between the two cycles has been attributed to structural variation in the material and the development of the b.c.c. phase which will discussed in greater detail later in this section.

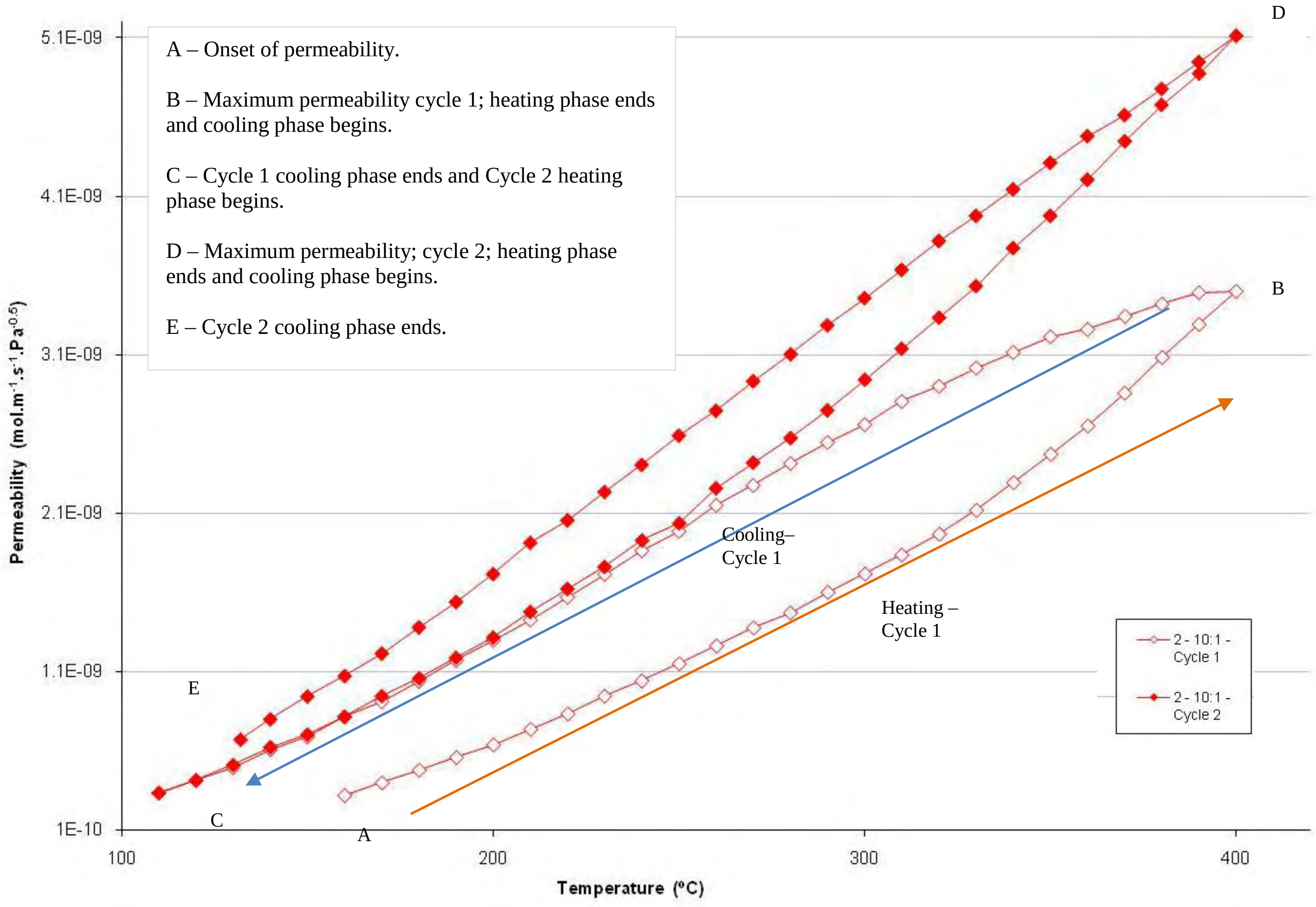

A – Onset of permeability.

B – Maximum permeability cycle 1; heating phase ends and cooling phase begins.

C – Cycle 1 cooling phase ends and Cycle 2 heating phase begins.

D – Maximum permeability; cycle 2; heating phase ends and cooling phase begins.

E – Cycle 2 cooling phase ends.

Figure 4.21 – Annotated permeability against temperature for $Pd_{47.76}Cu_{52.24}$ with 10bar upstream and 1bar downstream hydrogen overpressure.

Initially an investigation was performed to demonstrate the effect of temperature, and thus composition, on the membrane material. Permeability traces were produced for two as received (f.c.c.) membranes. Sample A was heated to 400 ºC and then cooled to room temperature, with pressures of 16 and 1 bar for upstream and downstream sides respectively. Sample B was heated to 600 ºC with an upstream pressure of 1.25 bar and downstream pressure of 0 bar, no cooling curve is shown for this experiment (note that pressures are given in bar not barg). The permeability measurements for the two experiments are plotted in Figure 4.22.

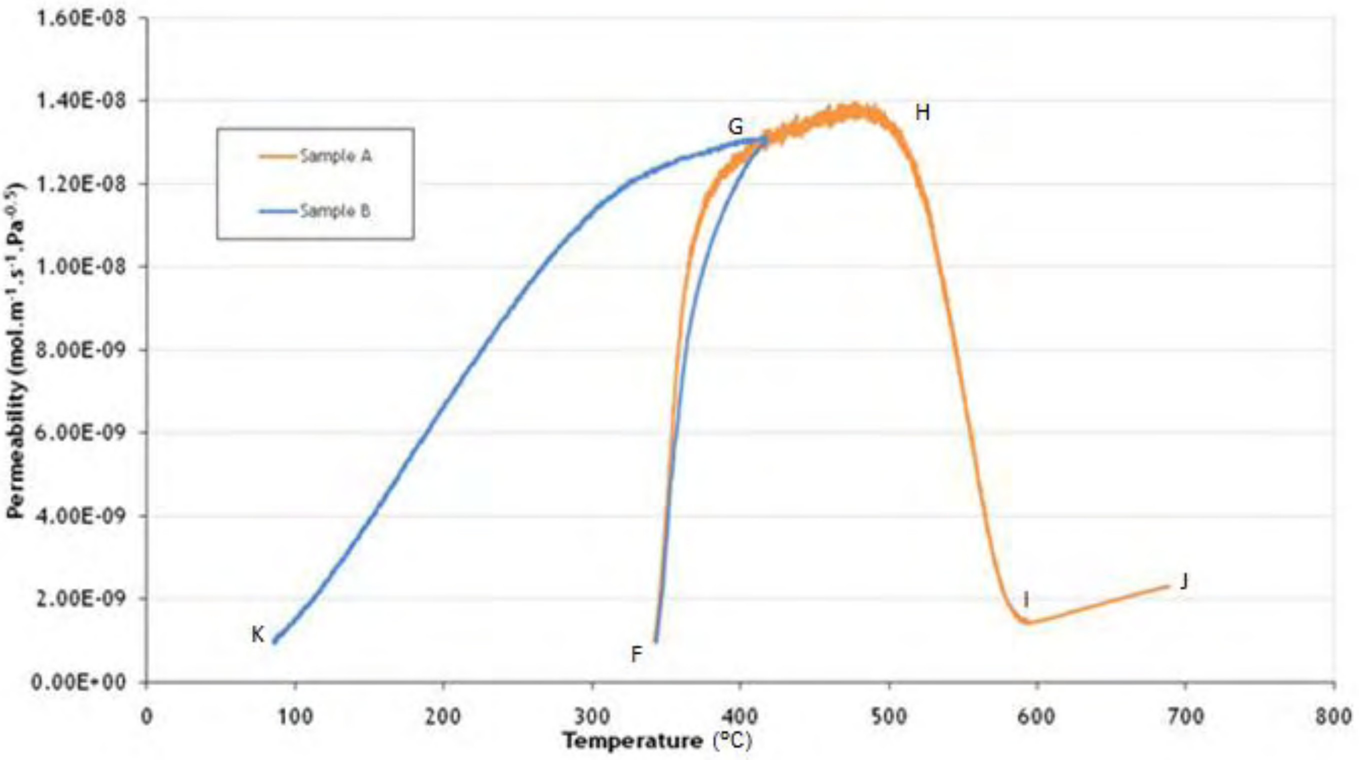

Figure 4.22 – Preliminary permeability experiments on as received $Pd_{47.76}Cu_{52.24}$; initial f.c.c. composition. Heated continuously to 700ºC for sample A and heated to 400ºC before cooling to room temperature for sample B.

In each case, despite different hydrogen pressure values, the onset of permeability occurs at ~340 ºC at point F. This value corresponds to the nucleation of the b.c.c. phase. Prior to this insufficient heat was input to allow the kinetics required for phase transition. As temperature increases from F to G the b.c.c. phase rapidly forms, this is confirmed by rapidly increasing permeability.

Sample A is heated to 700 ºC and through the permeability trace phase transformations can be seen. Between F and H phase change is limited although a slight increase in permeability occurs with increasing temperature. At point H (~500 ºC) the f.c.c. phase begins to nucleate and so a decrease in permeability is noted. The transition temperature corresponds to the values given in Figure 4.16 at 1 bar pressure. The phase transition occurs up to 600 ºC, at point I; again the end point of phase transition corresponds well with the values given in Figure 4.16 at 1 bar pressure. Between points I and J the sample is fully f.c.c. with a slightly increasing permeability value due to the increasing temperature; as observed between points G to H in the b.c.c. phase.

Sample B is cooled at 400 ºC and the permeability decreases to point K, along a different path to the heating cycle (A to B). This shows the b.c.c. phase is maintained in the majority of membrane.

4.3.2.1 Durability Testing

The durability of the as received $Pd_{47.76}Cu_{52.24}$ alloy, supported by macro-porous stainless steel, was also tested by continual thermal cycling under hydrogen from 75-400 ºC. A pressure of 16bar was selected for the upstream side of the membrane and 1bar for the downstream side; the high pressure differential ensured high stresses were placed on the membrane. The sample was thermally cycled 8 times; showing increasing permeability with each cycle, Figure 4.23.

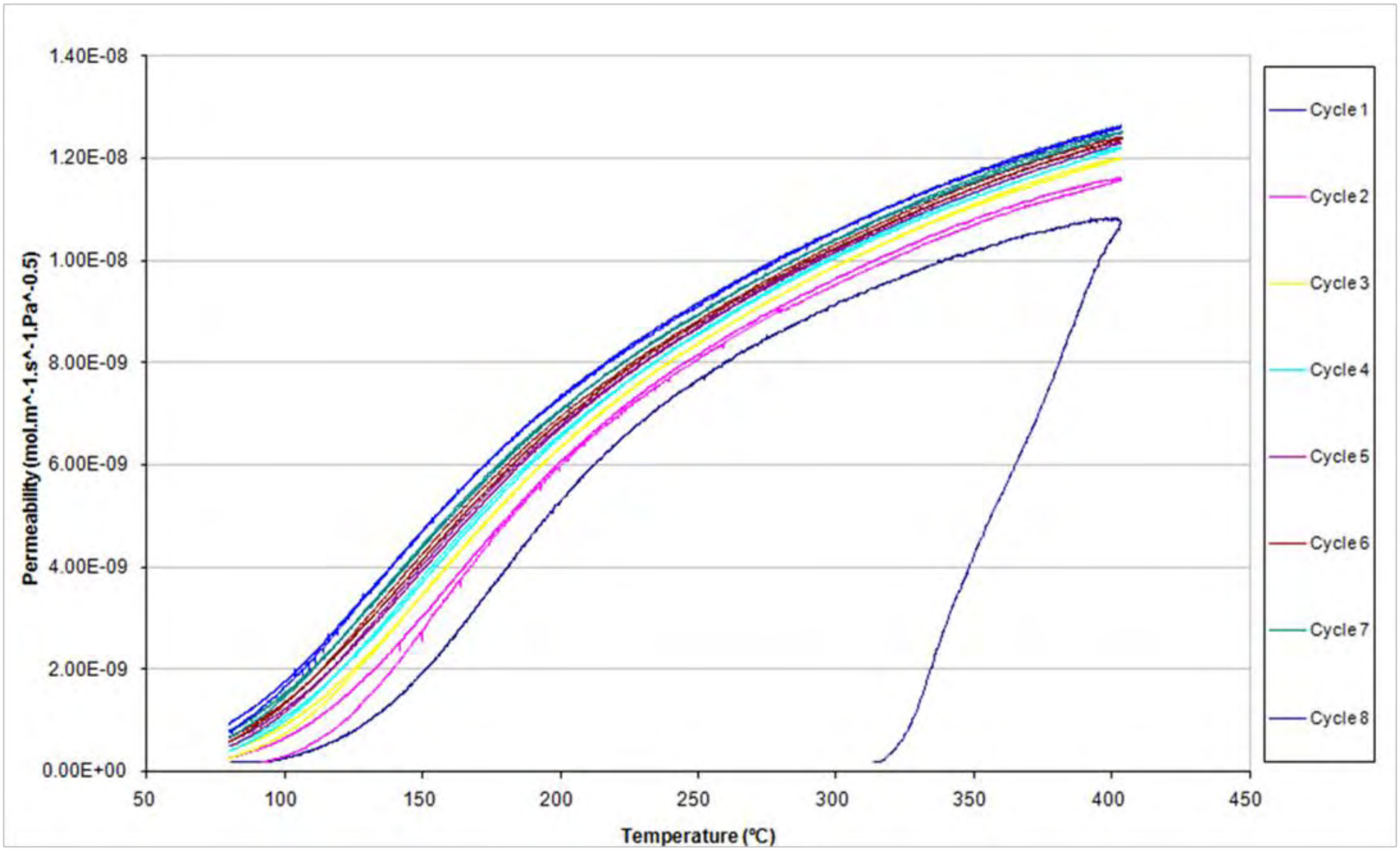

Figure 4.23 – Permeability of as received $Pd_{47.76}Cu_{52.24}$ (batch 2) alloy thermally cycled between 70 and 400 ºC with an upstream pressure of 16 bar and downstream pressure of 1bar.

The alloy demonstrates good durability during limited thermal cycling making the alloy potentially useful for commercial applications. Increasing membrane permeability was noted between cycles was noted initially at the minimum temperature of 75 ºC and persisted over the whole range of test temperatures. A possible explanation for this could be increasing leak flow during thermal cycling as the knife edge seal is loosened due to thermally activated expansion and contraction of the nuts and bolts. However the contribution of leak flow was measured at room temperature on the final cycle and no leaks were detected. It may be that the increase in permeability between thermal cycles arises as a result of grain coarsening with prolonged exposure to elevated temperatures. Grain coarsening will reduce the total amount of grain boundaries which the screened proton of hydrogen needs to cross, allowing for increased permeability. This could also this be due to small but progressively greater degrees of ordering in the bcc phase being formed and stabilised in the presence of hydrogen.

4.3.3 Permeability Measurements for $Pd_{47.76}Cu_{52.24}$

Hydrogen flux represents the amount of hydrogen passing across a membrane of a given area per unit time, whereas hydrogen permeability is a temperature dependant constant for the material which would be independent of pressure (Equation 2.7). However, in the Pd-Cu system, hydrogen pressure on the downstream side of the membrane will affect the crystal structure and as such both the hydrogen flux and permeability (Figure 4.24).

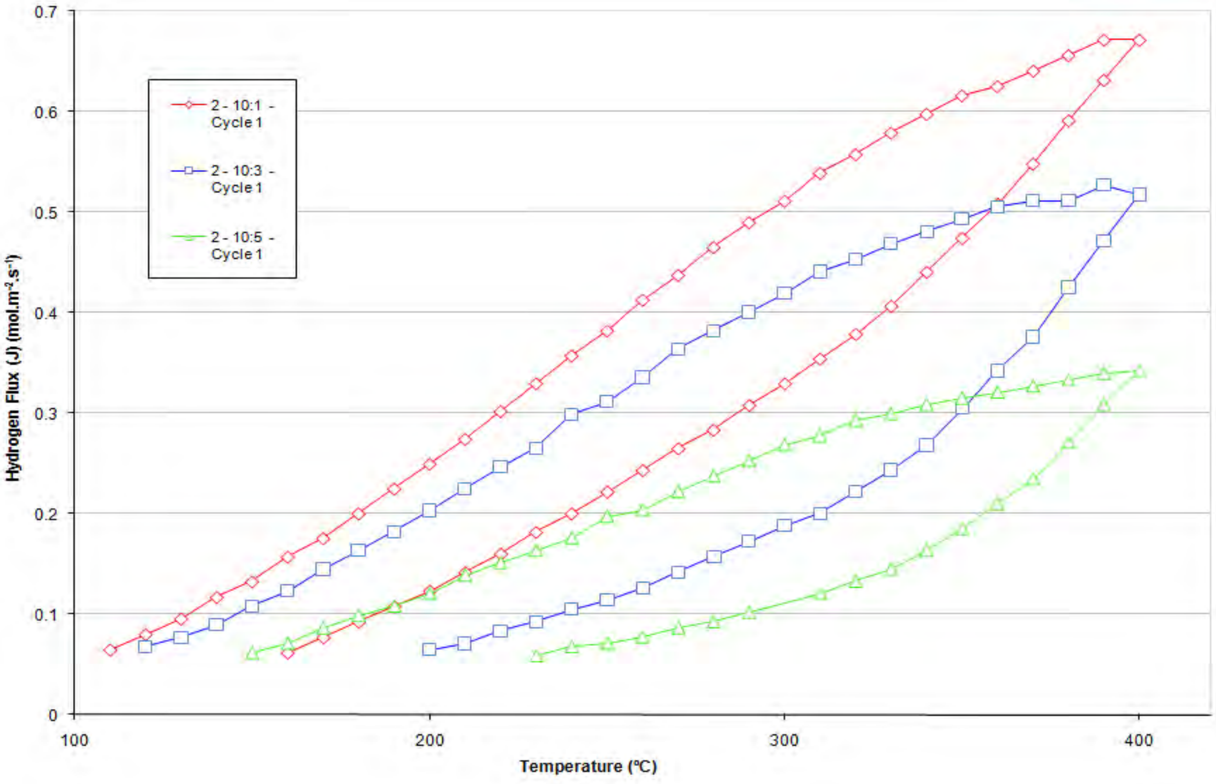

Figure 4.24 – Hydrogen flux against temperature for $Pd_{47.76}Cu_{52.24}$ for experimental configurations with hydrogen overpressures of 10 bar upstream and 1, 3 and 5bar downstream.

As would be anticipated a greater pressure differential appears to lead to a greater hydrogen flux. However, as found through in-situ XRD in the present work, the crystal structure is dissimilar between membranes; hence the pressure differential is not the only factor that has allowed for hydrogen flux to vary.

A comparison between hydrogen permeability for the same membranes is given in Figure 4.25. Although greater pressure gradients lead to increased hydrogen flux, permeability measurements demonstrate that exposure to greater hydrogen pressure on the downstream side result in higher permeability. This apparent contradiction that pressure difference is not the dominant factor probably arises from the interrelation between hydrogen and the crystal structure in Pd-Cu alloys.

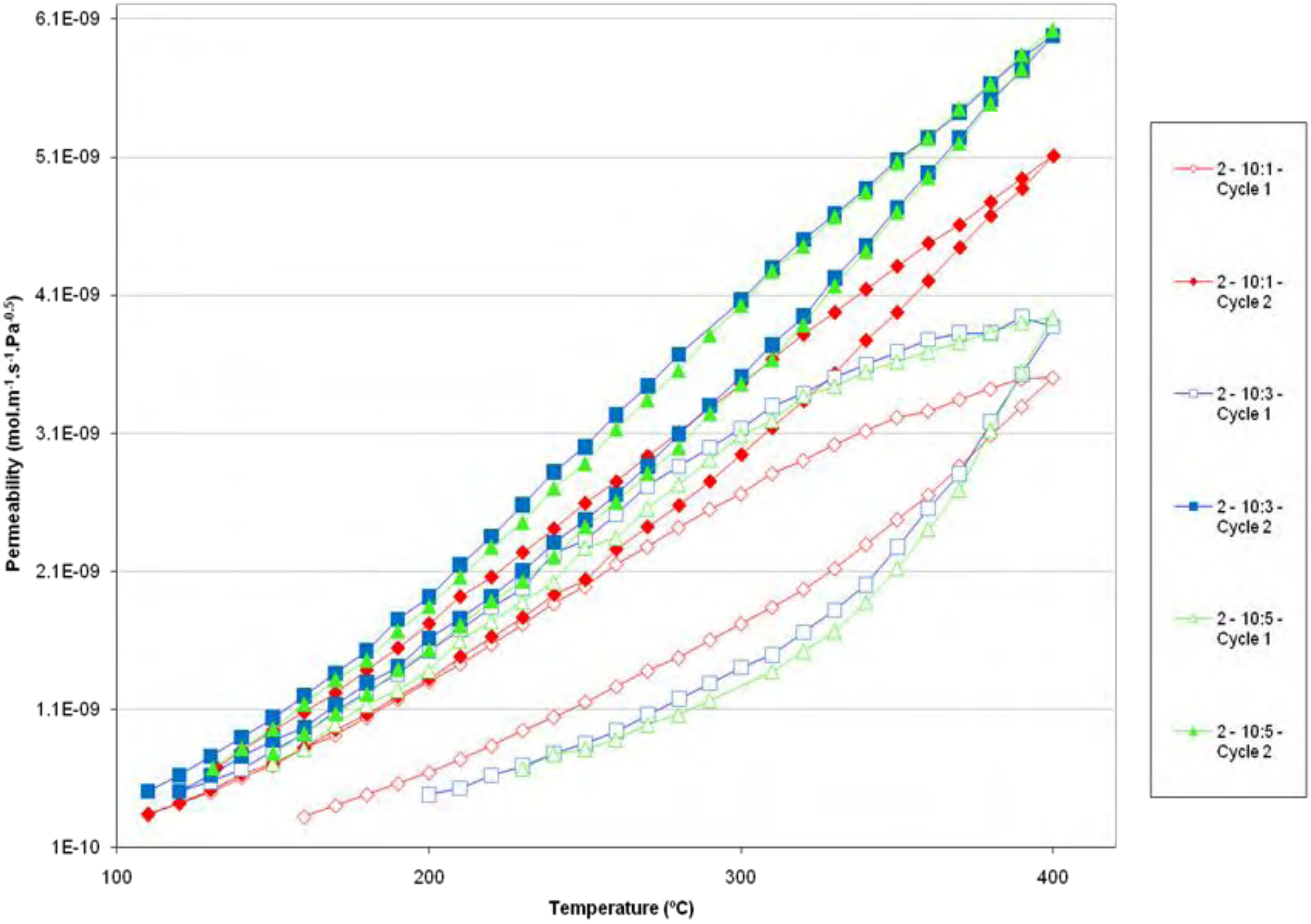

Figure 4.25 - Permeability of $Pd_{47.76}Cu_{52.24}$ (batch 2) under downstream pressures of 1, 3 and 5 bar.

Similar maximum permeability values, of ~6x10^{-9} mol.m^{-1}.s^{-1}.$Pa^{-0.5}$, for experimental configurations with downstream hydrogen overpressures of 3 and 5 bar were recorded on the second cycle. The configuration with a downstream pressure of 1bar showed a lower permeability value ~5.2x10^{-9} mol.m^{-1}.s^{-1}.$Pa^{-0.5}$; i.e. 85% of the values measured for 3 and 5bar configurations. The data indicate that within the total pressure range of 10 to 1 bar across the membrane, decreasing the pressure differential has increased its hydrogen permeability value at a given temperature.

As noted previously there is the large increase in permeability between the first and second cycle; a trend apparent for all experimental configuration. The development of the b.c.c. phase, by cooling under hydrogenated conditions, is likely to be the source of the increase in permeability between the two cycles. It has been shown (Figure 4.16) that after heating to 400ºC the structure will still contain some f.c.c. phase irrespective of the hydrogen overpressure. The phase balance of the alloy after cooling from 400ºC, however, cannot be determined from these in-situ XRD experiments. A foil was subjected to the same temperature profile as the first cycle of a membrane under 10 bar hydrogen overpressure and a room temperature XRD scan of the foil was subsequently produced, Figure 4.26.

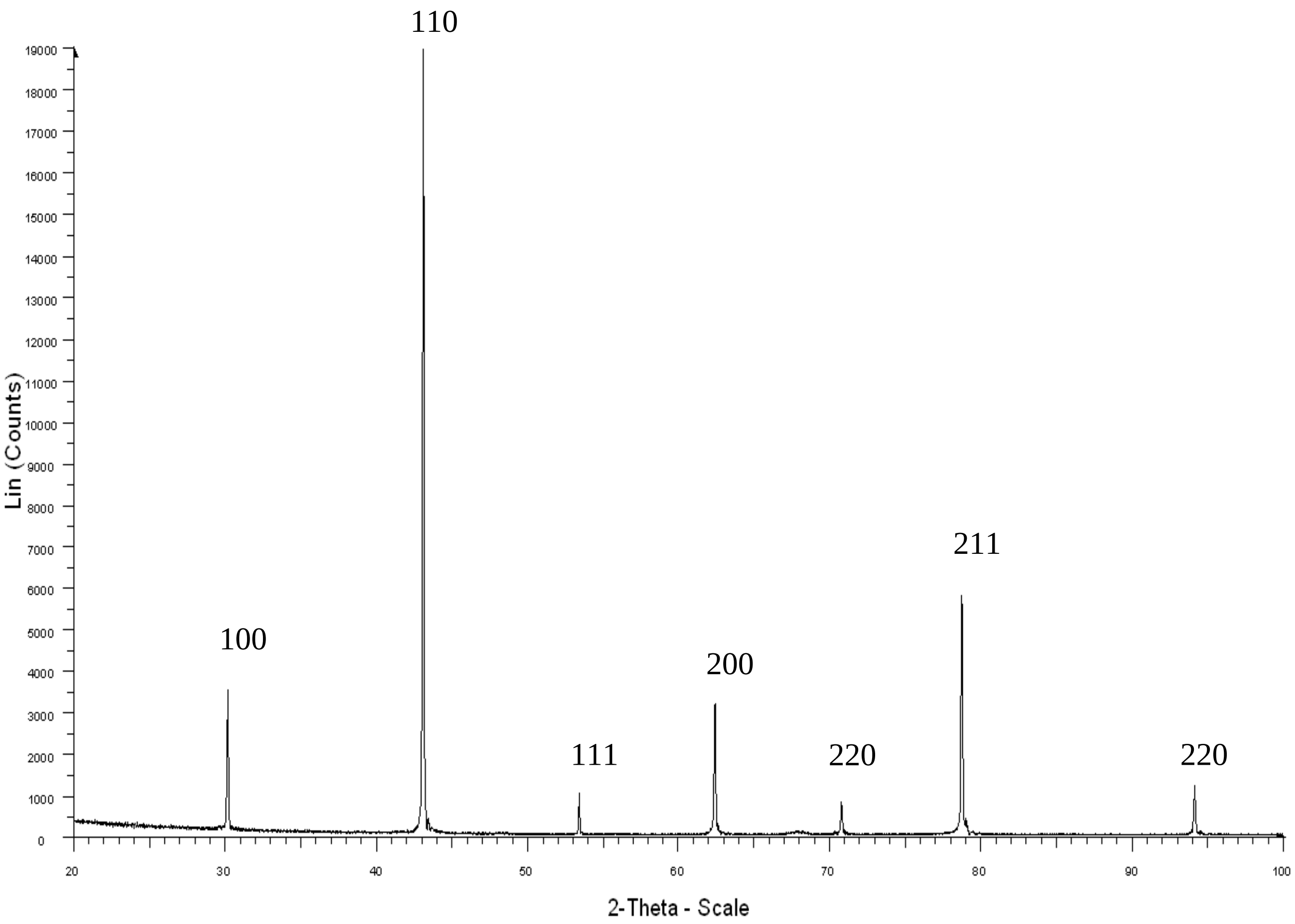

Figure 4.26 – An XRD trace of Pd$_{47.76}$Cu$_{52.24}$ after heating to 400 ºC while exposed to 10bar hydrogen and cooling slowly replicating the conditions of permeability experiments.

The XRD spectra revealed the structure was fully b.c.c. after thermal and hydrogenation conditions replicating the first cycle of the permeability tests. This data explains that the second cycle is more likely to have given a higher hydrogen flux value due to a greater volume fraction of b.c.c. phase in the alloy. Similarly, cooling in atmosphere of 1bar hydrogen of a Pd-Cu alloy with a similar composition has been shown to give a fully b.c.c. structure (Decaux). This indicates that all samples in the second cycles of the present work are probably fully b.c.c. Variable permeability values at a given temperature in both different experimental configurations and between cycles using the same membrane, underlines the apparent effect of the development of b.c.c. phase.

A smaller increase in permeability between heating and cooling of the second thermal cycle are apparent for each experimental configuration. As the structure is fully b.c.c. further development of this phase is not possible, however, it may come as a result of a more ordered structure forming due to continued high temperature exposure.

The activation energy (E_A) for hydrogen permeation may be calculated using an Arrhenius-type plot of the experimental data. The relationship between temperature and diffusion co-efficient is given by equation 4.3.

$$D = D_0 \exp\left(\frac{-E_A}{RT}\right)$$

Equation 4.3

D – Diffusion coefficient	R – Universal gas constant
D_0 – Diffusion coefficient at 0	T - Temperature
E_A – Activation energy	Φ - Permeability

The hydrogen permeability of a material is influenced by both its hydrogen solubility and hydrogen diffusivity. As the alloy is Pd-rich it can be assumed the surface activity of the alloy is high, and the hydrogen solubility remains constant, meaning hydrogen diffusion is the main limiting factor for permeation. As hydrogen solubility may be considered constant, permeability (ϕ) can replace diffusion co-efficient (D) without rearranging the equation 4.3 giving equation 4.4.

$$\phi = \phi_0 \exp\left(\frac{-E_A}{RT}\right)$$

Equation 4.4

In order to calculate the activation energy of permeation logarithms are taken of equation 4.4 rearranging it to equation 4.5.

$$\ln \phi = \ln \phi_0 - \frac{E_A}{RT}$$ **Equation 4.5**

A graph of $\ln \phi$ plotted against 1/T should thus be linear with the gradient equal to the activation energy of permeation (E_A) divided by universal gas constant (R). For non-linear sections other variables such as surface activity and solubility influence the permeability temperature dependence. The value of ϕ_0 represents the intercept when the x axis is equal to zero i.e. as temperature tends to 0. Variations in catalytic activity at the surface are unlikely given the high Pd content of the alloy and a high purity hydrogen gas stream (99.9995%) is used. Solubility variations through the material are more likely to be the cause of non-linear curves in this work.

Graphs were plotted to calculate the activation energy in both the fully f.c.c. and b.c.c. phases.

A fully f.c.c. structure was obtained at high temperature between 600 and 700 ºC in sample A (Figure 4.22). When the data for the fully f.c.c. region is plotted on a graph showing $\ln \phi$ against 1/T(K) the activation energy can be calculated as -37.47 $\mathrm{kJmol^{-1}}$ (Figure 4.27). With an R^2 value of 0.9978 the section of the curve approximates very closely to linear. Activation energy values of -25 to -27 $\mathrm{kJmol^{-1}}$ have been found in the literature (Zhang) for fully f.c.c. compositions of $Pd_{\sim 90}$-$Cu_{\sim 10}$ alloys and thus the value calculated in the present work seems to be reasonable.

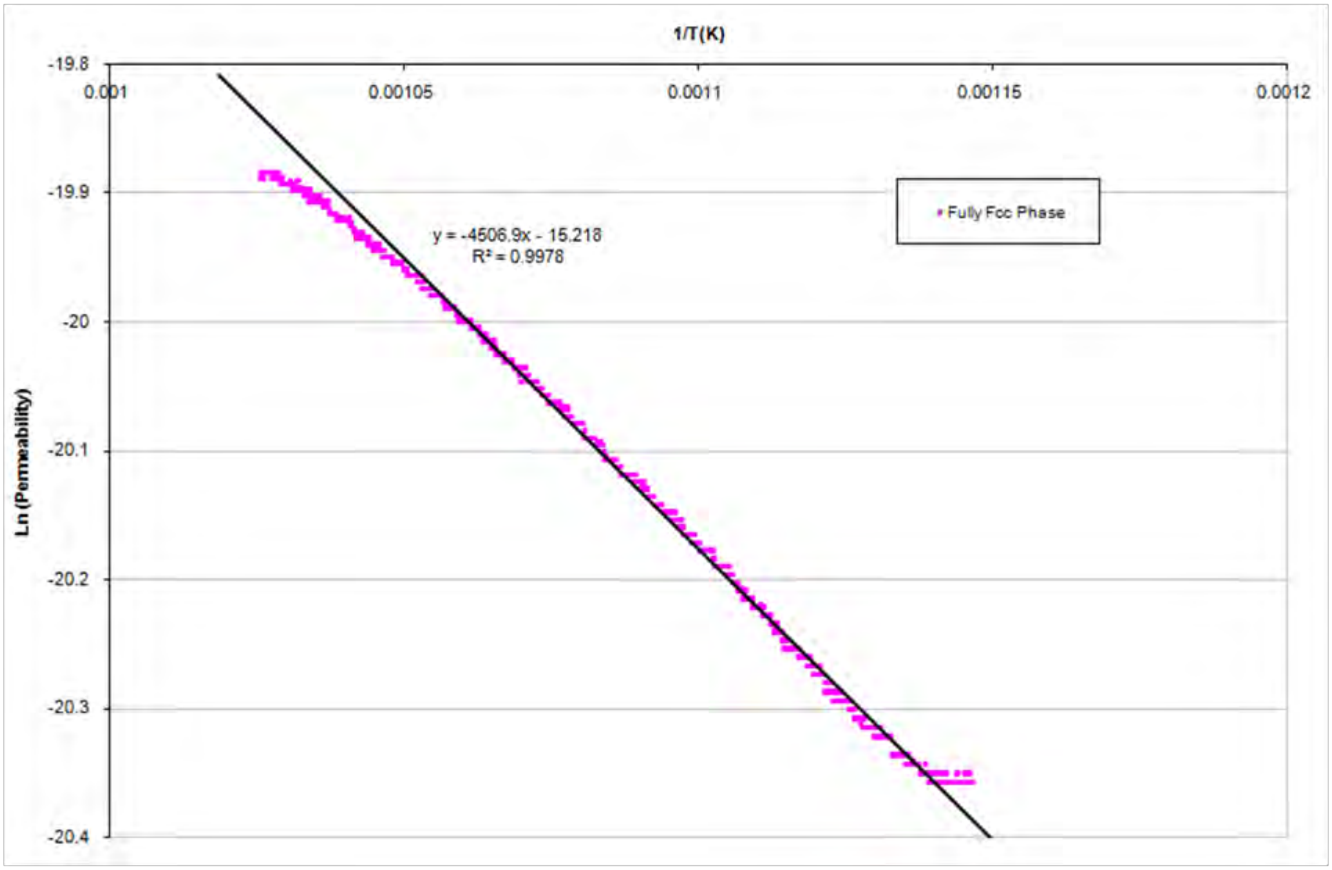

Figure 4.27 – Ln ϕ against 1/T for fully f.c.c. $Pd_{47.76}Cu_{52.24}$.

To calculate the activation energy of the b.c.c. phase, of the Pd $Pd_{47.76}Cu_{52.24}$ alloy, the results from the membrane with the 5 bar downstream pressure configuration cooling was chosen (Figure 4.25). Due to having the highest hydrogen concentration it was thought that this experimental configuration would ensure a fully b.c.c. structure. The second cycle was chosen as less structural changes are expected after prolonged exposure to high temperatures. The 1/T against Ln permeability graph for the 5 bar downstream configuration is given in Figure 4.28.

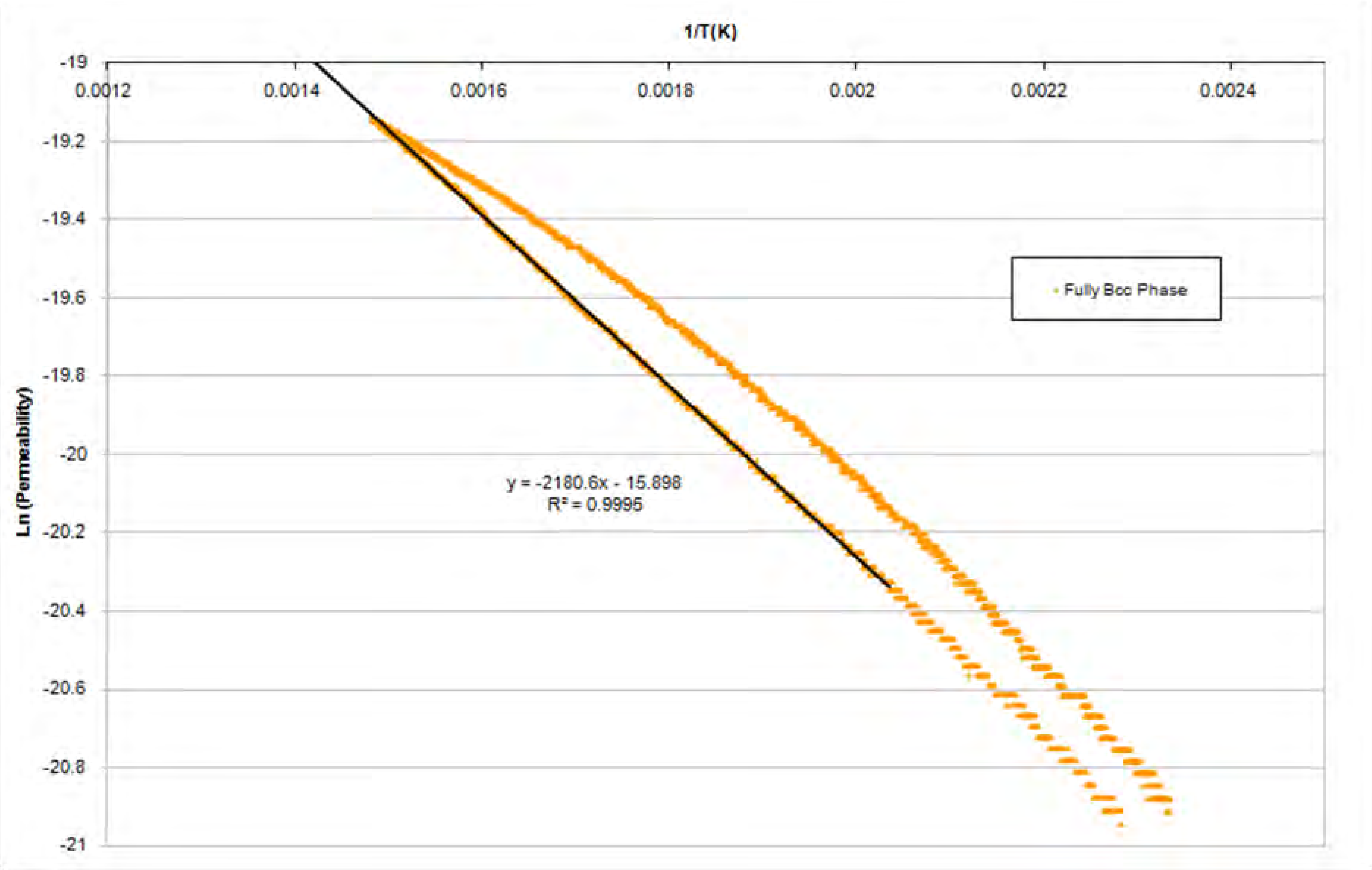

Figure 4.28 – Ln ϕ against 1/T for fully b.c.c. $Pd_{47.76}Cu_{52.24}$.

The activation energy was calculated to be -18.13 kJmol^{-1}; a value far lower than that of the f.c.c. phase, explaining why hydrogen permeability in the b.c.c. phase is significantly greater, at a given temperature. With an R^2 value of 0.9995 the cooling section of the plot is very linear. However in heating and later on in the cooling cycle the graph has a more curved shape indicating that structural changes or ordering may be occurring. Generally, there are very few extended linear regions of these graphs particularly on the first temperature cycle indicating solubility effects or structural changes. Gao, Li and Lin calculated the b.c.c. phase to have an activation energy of -15.4 kJmol^{-1} for an alloy of Pd_{46}-Cu_{54}. These values are closely comparable especially in light of the slightly differing compositions.

Thus the measured activation energy of $Pd_{47.76}Cu_{52.24}$ is lower in the b.c.c. phase but higher in the f.c.c. phase. The Pd-Cu values are similar to that of that of the high permeability Pd_{77}-Ag_{23} (30.8-25.7 kJmol^{-1}) with a f.c.c. crystal structure, used commonly used in commercially available hydrogen purifiers (Tong). As noted earlier activation energies of -25 to -27 $kJmol^{-1}$ have also been measured for $Pd_{\sim 90}$-$Cu_{\sim 10}$ f.c.c. alloys (Zhang), emphasising the clear differentiation between the b.c.c. and f.c.c. Pd alloys.

4.3.4 Permeability Measurements for $Pd_{50.10}Cu_{49.90}$

Permeability measurements with 10bar upstream and varied downstream pressures of hydrogen were carried out (Figure 4.29). Second thermal cycles uniformly showed higher permeability than the first with downstream pressure of 1bar permeability values of ~$3.2x10^{-9}$ $mol.m^{-1}.s^{-1}.Pa^{-0.5}$ were found, approximately 86% of the 3 bar downstream pressure (~$4x10^{-9}$ $mol.m^{-1}.s^{-1}.Pa^{-0.5}$) despite a lower pressure differential. The permeability observed for the experimental configuration with 5bar downstream pressure was lower than measured at 1 and 3bar. Permeability was measured for the initial cycle with 5 bar downstream pressure but was negligibly small. This was attributed to both reduced pressure differential for this configuration and greater membrane thickness, compared to previous $Pd_{47.76}Cu_{52.24.}$

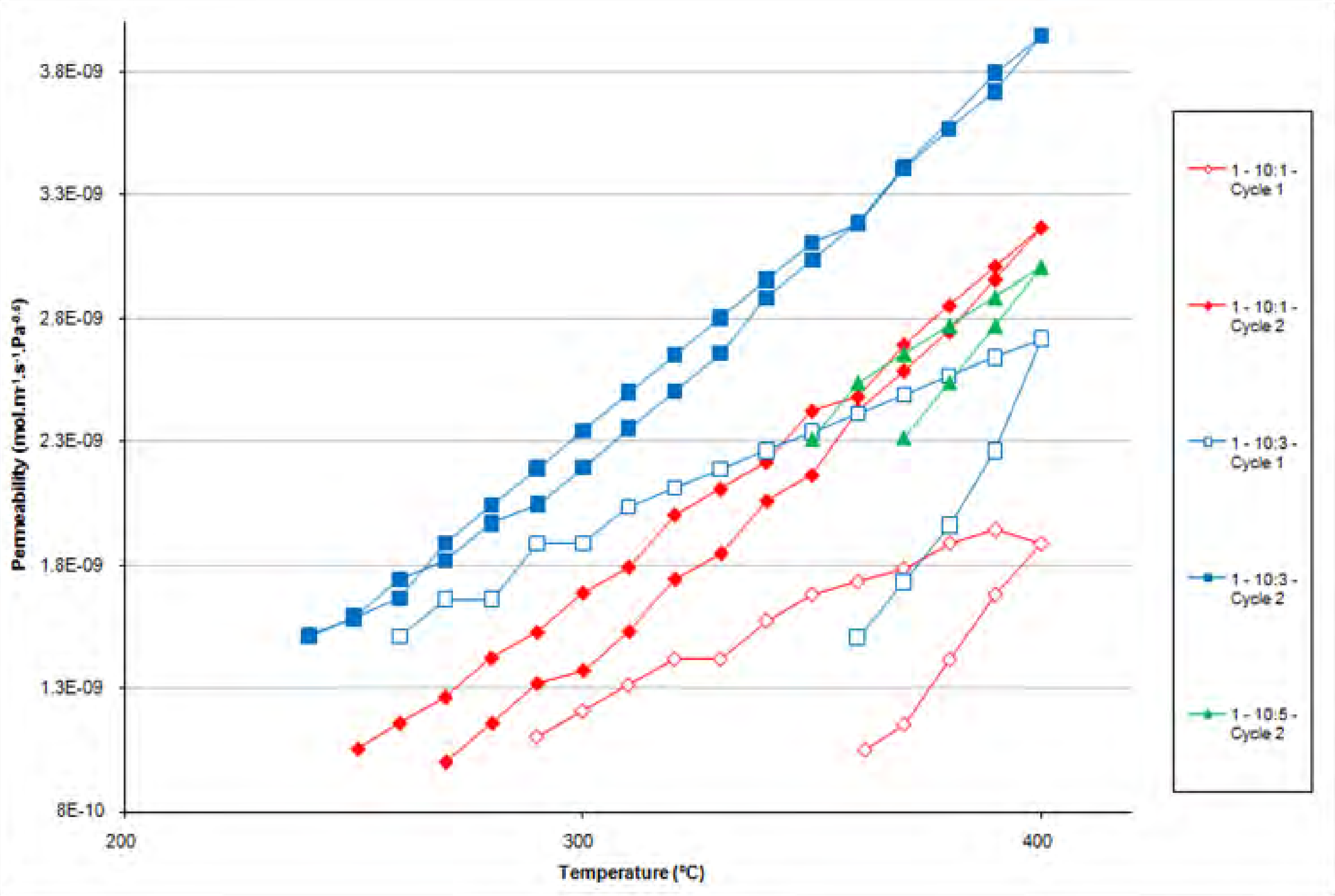

Figure 4.29 – Permeability of $Pd_{50.10}Cu_{49.90}$ (batch 1) under with downstream pressures of 1,3 and 5bar.

From the XRD spectra (Figure 4.19) it is clear that more b.c.c. phase is nucleated in heating up to 400 ºC. Slow cooling may lead to the percentage of b.c.c. increasing further or decreasing depending on the homogeneity of the alloy from previous heat treatments. This factor may be the origin of the higher permeability values which are achieved on the second permeability cycle for all configurations. This increase in permeability may also be as a result of increased homogeneity of the alloy. To investigate the possibility an XRD scan was carried out on opposite sides of membrane with the 1 bar downstream pressure, Figure 4.30.

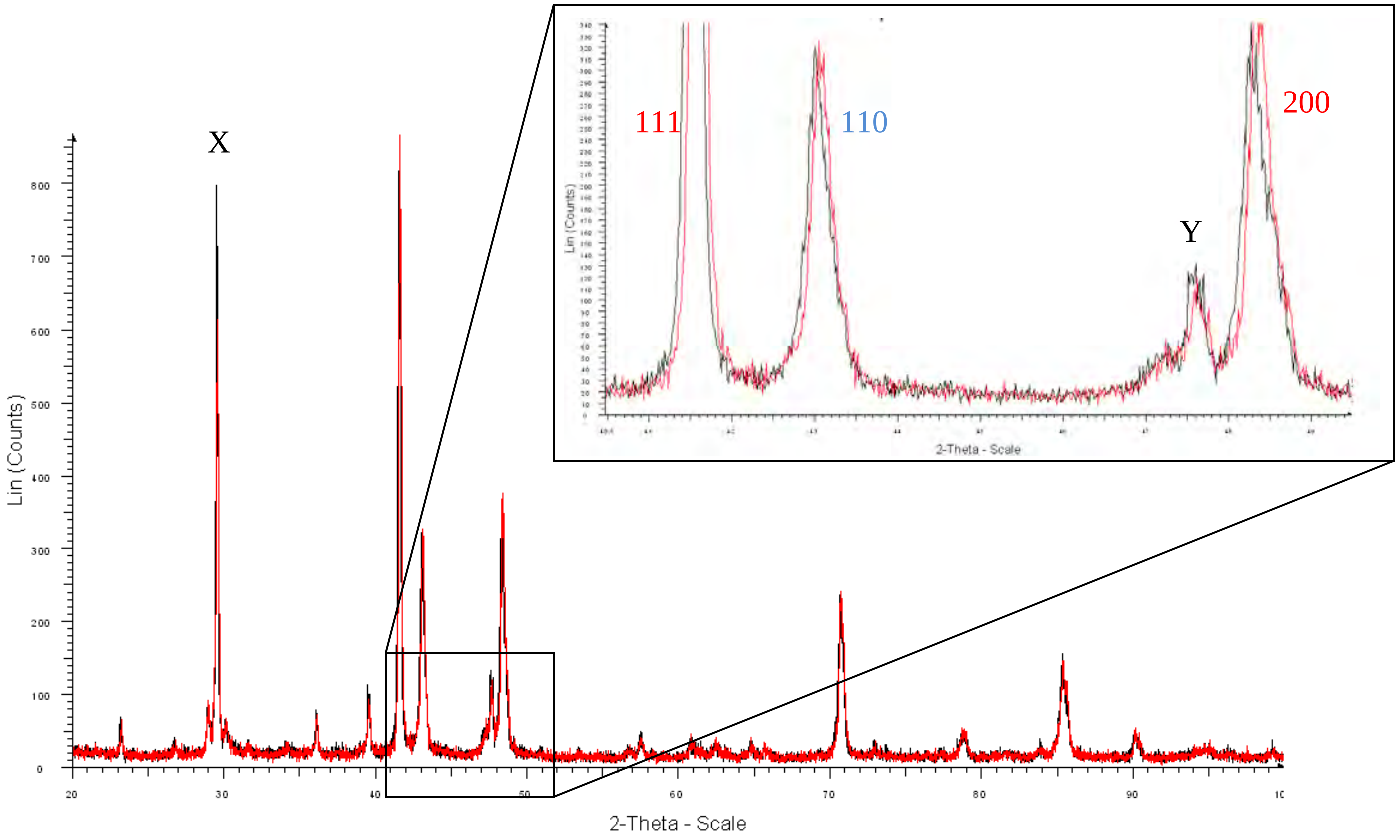

Figure 4.30 – XRD scan of 10 bar side of the $Pd_{50.10}Cu_{49.90}$ (batch 1) membrane with 3 bar downstream configuration. F.c.c. peaks are denoted in red text and b.c.c. in blue.

The results indicated that more b.c.c. phase was nucleated during the hydrogen permeability tests. Topas analysis showed 24% b.c.c. phase was nucleated, compared to an average of ~15% prior to permeability testing. Topas software attributed a small peak at 30° to the [100] reflection of the b.c.c. phase rather than the larger peak at point X (29.4°). The large peak could not be matched to a hydride or oxide of palladium or copper. If this peak were attributed to the [100] reflection of the b.c.c. phase, it would raise the composition beyond 24%. A phase balance increase may indicate that the phase boundary has shifted towards the Pd-rich end of the diagram the lever rule it could be implied that more b.c.c. phase may be grown. Alternatively, it may show that the initial composition of the alloy was not cooled under equilibrium conditions and kinetic effects limit the growth of b.c.c. phase. Several small undefined peaks such as Y are found on this sample this may stem from a warped foil taken from the membrane material.

The onset of significant hydrogen permeability did not occur until 360 ºC for either 1 or 3bar experimental configurations. However upon cooling the alloy continued to permeate hydrogen to temperatures as low as 290ºC and 260 ºC for 1 and 3 bar configurations respectively. This, along with the phase balance change summarised in Figure 4.30 indicates the structure does change during permeation. As the shape of the permeability trace is relatively invariant, this suggests the same mechanism between 1 and 3 bar configurations. Similarly the shape of the permeability versus temperature curve measured for the second cycle at 5bar downstream pressure replicated the second cycle of both 1 and 3 bar.

Between the two sides of the membrane a slight shift was noted in the XRD spectra, with the 10bar side measured to have 24.90% b.c.c. and 1bar side 24.77% b.c.c. This may be due to the XRD measurements being performed using different specimen heights and is within the experimental error. This indicates that the phase balance does not change with increased hydrogen content for this composition of alloy ($Pd_{50.10}Cu_{49.90}$).

Derivations of activation energy values from the permeability versus temperature data have already been discussed (see Section 4.3.2). Generally graphs of the natural logarithm of permeability against 1/T for $Pd_{50.10}Cu_{49.90}$ did not show extended linear regions where R^2 values were above 0.997. An example of this is in Figure 4.31 showing the trace for the configuration with 1bar downstream. This was due in part to limitations of the mass flow controller, resulting in the same permeability being measured over a range of temperatures. The shape of the curve indicates solubility or structural changes in the membrane during permeation.

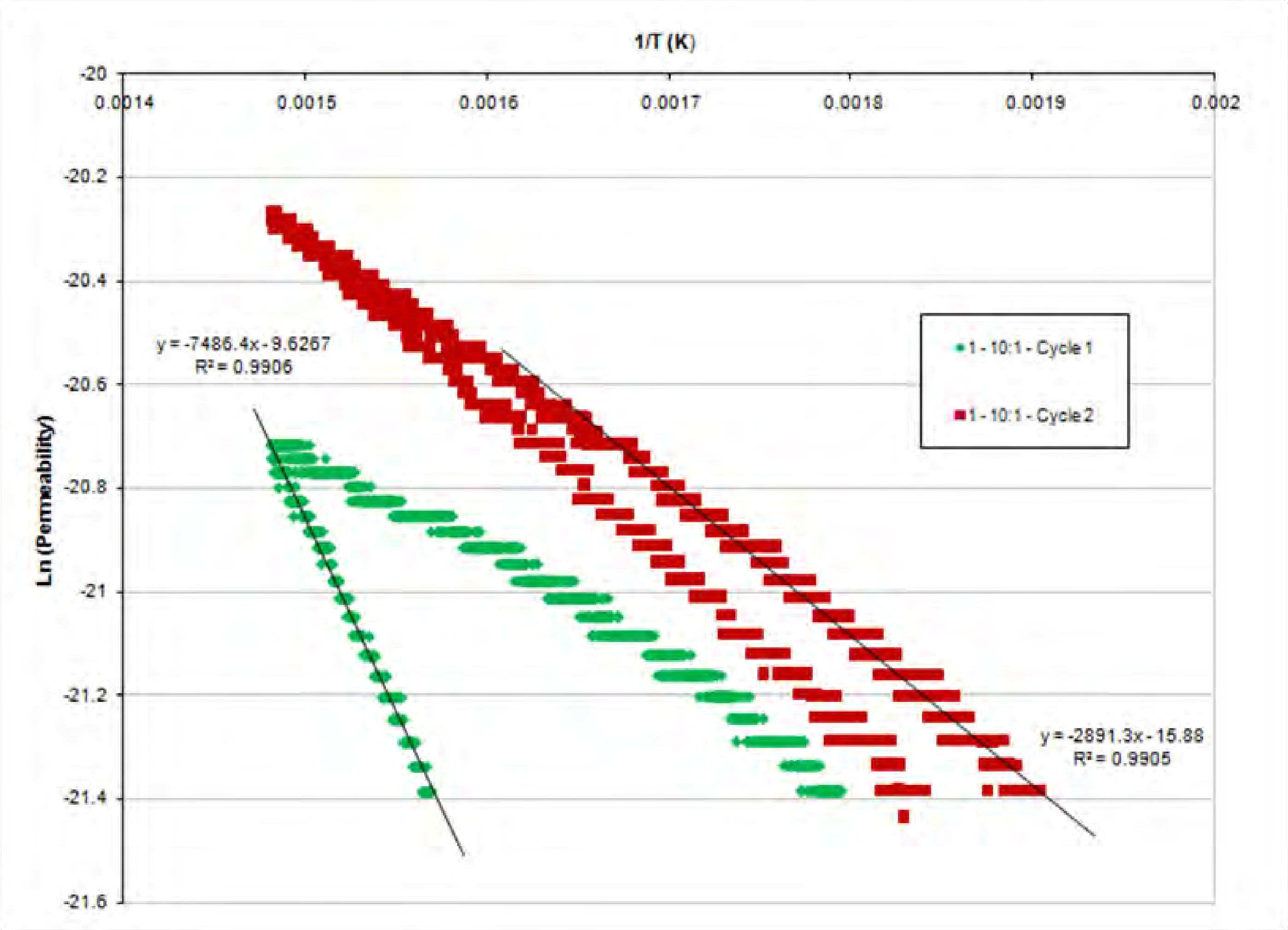

Figure 4.31 – Ln permeability against 1/T for $Pd_{50.10}Cu_{49.90}$ (batch 1) cycles 1 (green) and 2 (red).

An approximate value of the activation energy for hydrogen transport, in the mixed phase $Pd_{50.10}Cu_{49.90}$ alloy, for the initial heating curve, where the percentage b.c.c. is ~15% has been calculated to be -62.38 $kJmol^{-1}$. The R^2 value in this case was 0.9913 meaning the analysis is invalid. The cooling curve at low temperatures of the second cycle is likely to have a composition of ~25% b.c.c. Again, this region was not linear, with an R^2 value of 0.9939, but an approximation of activation energy has been calculated as -22.29 $kJmol^{-1}$, similar to the value of -18.13 $kJmol^{-1}$ for fully b.c.c. phase $Pd_{47.76}Cu_{52.24}$ calculated previously.

4.3.5 Permeability Measurements for $Pd_{\sim 56.5}Cu_{\sim 43.5}$

Permeability measurements for $Pd_{\sim 56.5}Cu_{\sim 43.5}$ membrane will be affected by compositional variations across the membrane material as described in section 4.1.4. XRD spectra were taken prior to permeability tests ensuring the A side was facing the upstream direction. Hydrogen permeability measurements carried out for 1, 3 and 5 bar downstream configurations are shown in Figure 4.32.

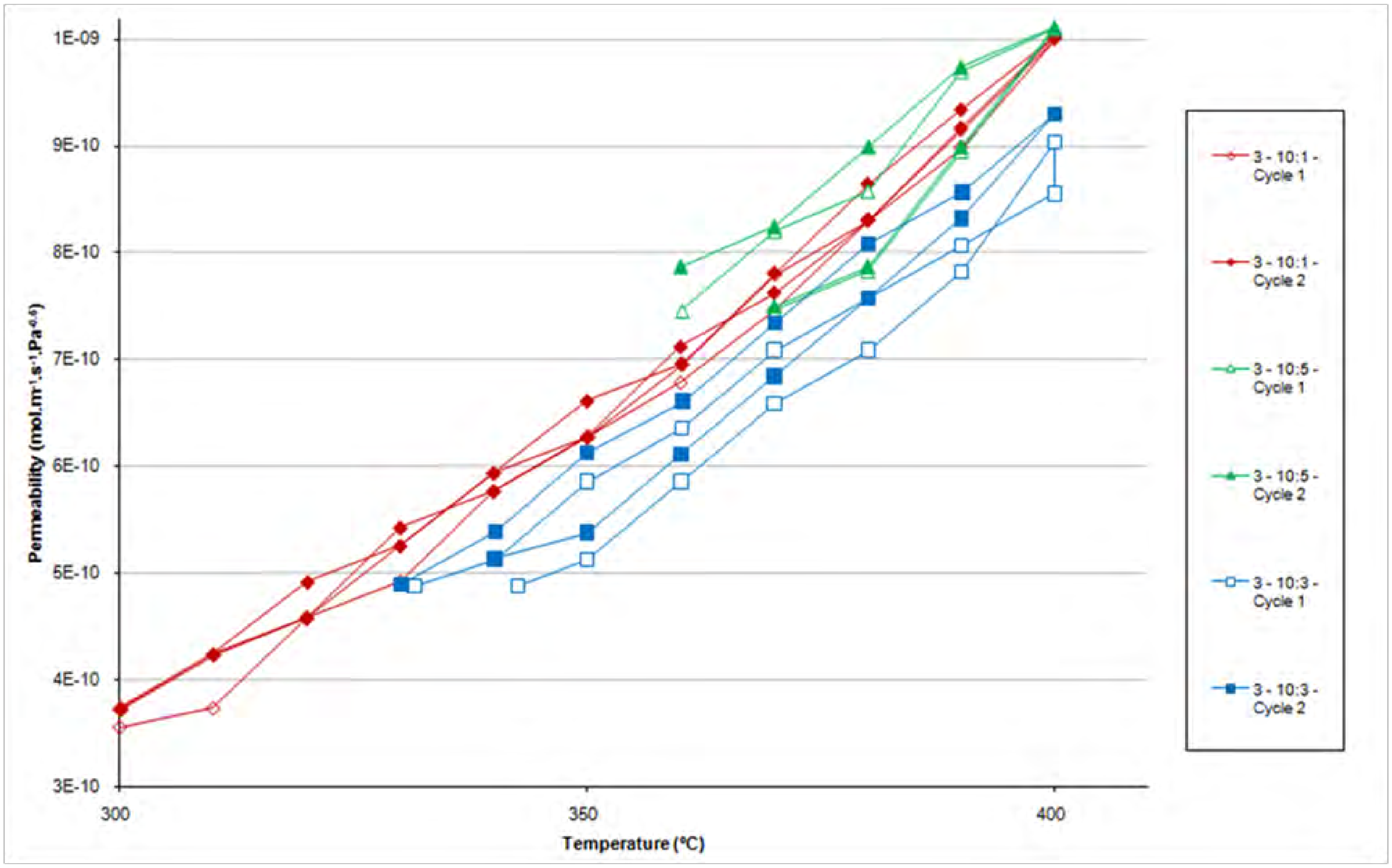

Figure 4.32 – Permeability of $Pd_{\sim56.5}Cu_{\sim43.5}$ (batch 3) with side A (~59 at%Pd) facing the upstream side and downstream pressures of 1,3 and 5bar.

The permeability values measured were considerably lower, by an order of magnitude, than for $Pd_{47.76}Cu_{52.24}$ and $Pd_{50.10}Cu_{49.90}$ under the same atmospheric and thermal conditions; with maximum values of ~6 $x10^{-9}$ $mol.m^{-1}.s^{-1}.Pa^{-0.5}$ and ~4 $x10^{-9}$ $mol.m^{-1}.s^{-1}.Pa^{-0.5}$ respectively. This was attributed to the dominance of a fully f.c.c. structure on at least one side of the material or perhaps due to better activation of H_2 at the more Pd-rich surface. The onset of permeation occurred before that of $Pd_{50.10}Cu_{49.90}$, most likely due to reduced membrane thickness. Between cycles of the same configuration permeability measurements had a similar shape indicating no structural change had taken place. These results are similar to those of McKinley who also noted lower permeability in alloys around this composition range.

In contrast to the b.c.c. phase Pd-Cu alloy variations of hydrogen permeability with downstream pressure do not appear to follow any trend. Downstream pressures of 1 and 5 bar gave the highest maximum permeability, ~$1x10^{-9}$ $mol.m^{-1}.s^{-1}.Pa^{-0.5}$, while 3 bar was slightly lower, ~9.3 $x10^{-9}$ $mol.m^{-1}.s^{-1}.Pa^{-0.5}$. In-situ XRD under 10bar hydrogen pressure showed that on the downstream side of the membrane no b.c.c. phase would be nucleated in the first temperature cycle although permeability was measured. This demonstrates that permeability must be dominated by the f.c.c. phase, explaining the lower measured permeability.

4.4 General Discussion

Two common themes have arisen during the analysis of the present results; the impact which hydrogen has upon the b.c.c. to f.c.c. phase transition process in Pd-Cu alloys and how the data from the present work relates to the Pd-Cu phase diagrams presented by both Subramanian and Laughlin and Huang.

The $Pd_{47.76}Cu_{52.24}$ alloy has provided information about the Pd-rich end of the b.c.c./mixed phase boundary in the Pd-Cu phase diagram; the exact position of which differs between phase diagrams presented by Subramanian and Laughlin and Huang. The CALPHAD calculation from Huang predicts an alloy of this composition to lie purely in the b.c.c. phase, while the diagram by Subramanian and Laughlin, derived from a survey of experimental work, indicates this alloy coincides with the boundary line itself and so is likely to contain small amounts f.c.c. phase. Vacuum annealing of as received $Pd_{47.76}Cu_{52.24}$ at 500 ºC (later shown to be the maximum temperature mixed phase region before b.c.c. to f.c.c. phase transition begins) for 72 hrs failed to give a fully b.c.c. structure. This is in agreement with similar experiments at lower temperatures by Decaux. All the data from the present work indicates that the position of the b.c.c./mixed boundary at ~48 at%Pd in the Pd-Cu system is in keeping with Subramanian and Laughlin rather than Huang.

The in-situ XRD experiments, under hydrogenated conditions, showed that the development of a fully b.c.c. structure is achieved under 10 and 5 bar pressures. Furthermore, had the experiment at 1 bar hydrogen not failed at low temperatures then the same may have been said about this sample. These results support Huang’s proposal that the presence of hydrogen allows for transition to the b.c.c. phase to be energetically favourable. Notably this is supported by the present data from $Pd_{50.10}Cu_{49.90}$ where the XRD results highlight a similar effect; the b.c.c. phase is consistently nucleated in the presence of hydrogen but not under inert conditions, although in this instance equilibrium slow cooling may have not been achieved.

It should also be noted that the location of the mixed/f.c.c. phase boundaries are different in the diagrams proposed by Huang and Subramanian and Laughlin $\sim Pd_{57}Cu_{43}$ and $\sim Pd_{65}Cu_{45}$, respectively. The $Pd_{\sim 56.5}Cu_{\sim 43.5}$ alloy of the present work may be used to analyse data at these temperatures despite the actual composition of this alloy remaining unclear. XRD analysis taken from either side of the vacuum annealed $Pd_{\sim 56.5}Cu_{\sim 43.5}$ foil showed no b.c.c. phase had formed, contrary to the predictions of both phase diagrams. Although this may be due to non-equilibrium cooling may be playing a role.

The composition of side B ($Pd_{\sim 56.5}Cu_{\sim 43.5}$), from which in-situ XRD data was taken, exhibited no b.c.c. phase formation despite the presence of up to 10bar hydrogen. Permeability tests with side B on downstream, and thus exposed to 5, 3 and 1 bar hydrogen pressure, did not show any clear signs that b.c.c. phase content had increased: Permeability was significantly lower than for corresponding b.c.c. alloys. Furthermore, each cycle exhibited similar shape and results had similar maximum values at different pressure gradients. This indicates that no b.c.c. material was developed on at least the downstream side of the membrane. From the XRD spectra under hydrogen data it can be determined that no b.c.c. phase can be formed at this composition.

Between the two phase diagrams the Subramanian and Laughlin rather than the recent CALPHAD study from Huang appears to be more representative of the results accrued in this study. The precise position of phase boundaries remains uncertain but the effect of hydrogen in shifting the phase boundary in the direction of higher Pd concentration has been clearly demonstrated around the mixed/b.c.c. phase boundary.

The variation in alloy phase structure under different hydrogen pressures has been shown to exist in the Pd-Cu system by both in-situ XRD data of the present work and first principle thermodynamics calculations by Huang (Figure 2.10). It was therefore expected that the hydrogen permeability of Pd-Cu alloys should be dependent on the composition and crystal structure of the membrane as well as the hydrogen pressure gradients.

Between compositions $Pd_{47.76}Cu_{52.24}$ and $Pd_{50.10}Cu_{49.90}$ the permeability was observed to be greater when downstream pressure was increased from 1 to 3 bar for both thermal cycles, in spite of reduced pressure gradient. For $Pd_{47.76}Cu_{52.24}$ when downstream pressure was increased from 3 to 5 bar similar permeability was observed. $Pd_{50.10}Cu_{49.90}$ did not exhibit appreciable permeability on the first cycle and on the second, where permeability was observed, the values were less than that of 3 bar downstream pressure. This indicates that although the presence of hydrogen pressures on the downstream side of the membrane does influence the permeability sufficient pressure gradient is still required to ensure a driving force for hydrogen flux is maintained. Indeed, when an upstream pressure of 16bar and downstream pressure of 1 bar was selected for durability testing of the $Pd_{47.76}Cu_{52.24}$ alloy greater permeability values were observed. It is clear that in Pd-Cu b.c.c. alloys to optimise permeability a balance between the concentration of hydrogen present and the pressure differential is required.

Piper noted that the hydrogen diffusion coefficient for b.c.c. Pd-Cu phases was four orders of magnitude greater than f.c.c. Pd-Cu. The diffusion coefficient increases further as the alloy becomes more ordered due to prolonged exposure to higher temperatures. Conversely for Pd-Ag alloys, which have an f.c.c. crystal structure, the solubility of hydrogen is the dominant factor in permeability.

In comparison to the data from McKinley shown previously (Figure 2.9) the permeability values recorded in this study were significantly lower. A graph to show the comparison between the findings of McKinley and those in this study are given in Figure 4.33. The maximum permeability measurements performed on samples with 10bar upstream pressure and downstream pressures of 5, 3, or 1bar are recorded in red. These values are uniformly lower than those of McKinley and do not exhibit the same characteristic peak in permeability. However, the maximum recorded permeability of the durability test, in which $Pd_{47.76}Cu_{52.24}$ was cycled thermally 8 times, did exhibit the highest permeability values observed fir Pd-Cu alloys in the present work.

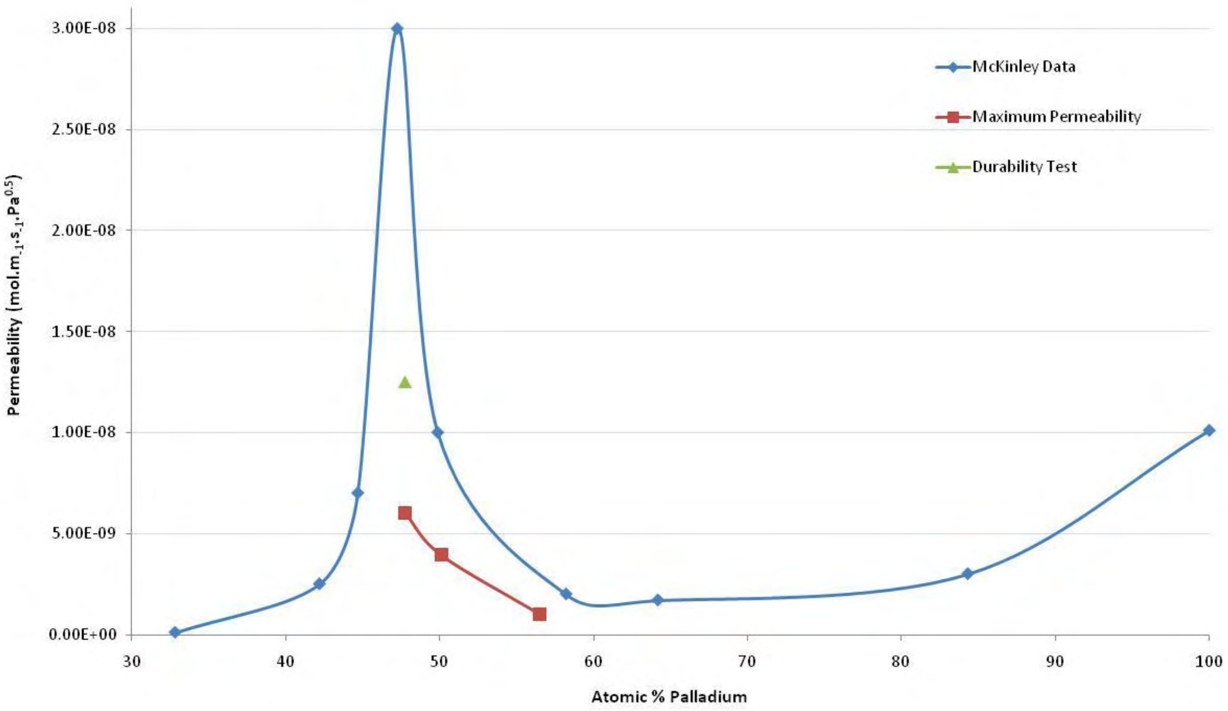

Figure 4.33 – A comparison of permeability data as recorded by McKinley and the values produced experimentally in this study.

The variation in permeability measured experimentally between the two $Pd_{47.76}Cu_{52.24}$ may have occurred due to poor alloy/surface condition induced by the vacuum annealing process which was not performed for the durability test membrane. Even in the first cycle of this experiment the measured permeability was greater than the maximum value of the vacuum anneal membranes. It may also be the case that greater hydrogen pressure on the upstream side and overall pressure gradient give rise to significantly higher permeability values.

Generally permeability was shown to increase in each of the thermal cycles when a fully b.c.c. phase structure has been established. This is particularly evident for the durability testing in which each of the 8 thermal cycles had a greater maximum permeability than the last. This may be as a result of changes to the alloy after to prolonged exposure to elevated temperatures in the presence of hydrogen; such changes may include grain coarsening or more extensive ordering of the phases present in the structure.

5 Conclusions

- The highest recorded hydrogen permeability for Pd-Cu alloys was for the $Pd_{47.76}Cu_{52.24}$ composition consistent with previous findings (Howard, Piper, McKinley, Decaux, Goldbach, Yuan). This alloy lies on the Pd-Cu phase boundary line and is hence initially mixed b.c.c./ f.c.c. phase. It was also shown that after exposure to hydrogen the structure became fully b.c.c. a factor which is necessary for maximising permeability.

- The presence hydrogen was also shown to facilitate the nucleation of the high permeability b.c.c. phase. This was probably associated with the favourable enthalpy of formation of the b.c.c. phase in the Pd-Cu-H ternary system as discussed by Huang.

- The position of the b.c.c/mixed phase boundary of the Pd-Cu system using CALPHAD calculations by Huang was not in agreement with the present work. Results at this composition were more in line with the findings of Subramanian and Laughlin.

- In-situ XRD data indicated that the location of the b.c.c./mixed phase boundary shifted in the presence of hydrogen towards the Pd-rich end. Increasing hydrogen over pressure was deemed to give rise to a more pronounced shift in the phase boundary position.

- Hysteresis of the b.c.c./ mixed phase transformation temperature, as reported (Goldbach, Yuan, Decaux) was exhibited by in-situ XRD. This may, however, have been associated with a dissimilar cooling profile for vacuum annealed samples leading to non-equilibrium phase balance.

- No b.c.c. phase was formed for the most Pd-rich alloy investigated ($Pd_{\sim 56.5}Cu_{\sim 43.5}$) providing further evidence that the previous studies of the Pd-Cu phase diagram in the 40-70 at% Pd region may be incorrect.

- From the experimental studies of membranes with a consistent upstream hydrogen pressure and varied downstream pressure it was shown that a reduced differential pressure across the membrane could lead to greater permeability, despite reducing the effective drive force for hydrogen flux. This effect was probably associated with structural differences on the downstream side of the membrane optimising conditions for hydrogen flux.

- Limited durability testing over 8 thermal cycles proved that the $Pd_{47.76}Cu_{52.24}$ alloy is potentially resistant to frequent thermal cycles in the presence of hydrogen gas.

- The $Pd_{47.76}Cu_{52.24}$ alloy or closely similar compositions gave the best combination of permeability and potential durability from Pd-Cu alloys.

6 Future Work

- Both downstream pressure and pressure gradient have been shown to have an effect on the maximum permeability of the membrane material. For $Pd_{47.76}Cu_{52.24}$, which has the best permeability of the three alloys investigated, further work is justified to establish the optimum conditions for hydrogen permeability. The current apparatus is well suited to these studies.

- Rectify issues with DSC measurements and rerun experiments. This may mean both repair to the machine and preparing the material as a powder to increase contact area in the sample cell. DSC results would compliment in-situ XRD data as well as giving more defined start and end points of phase transitions.

- Find a suitable metallographic etchant for Pd-Cu foils for analysis of both the grain size and phase morphology. Furthermore, etching of membranes exposed to high temperatures for prolonged periods would demonstrate whether grain coarsening had occurred. Grain coarsening has been previously cited as a possible cause for increasing permeability over prolonged periods.

- Should grain coarsening effects be confirmed by etchants, after prolonged exposure to hydrogen, then this may have an effect on leaked flow in mixed gas streams. If contaminant flow decreased as the grains coarsened this would demonstrate grain boundary diffusion of contaminant gases in Pd-Cu membranes.

- Permeability experiments performed on mixed gas streams accompanied by mass spectroscopy of the downstream gas composition to assess if grain boundary diffusion has occurred as noted above.

- Analysis of the shape of the concentration profile of hydrogen through the membrane material which will affect the crystal structure of the material would allow further modelling and optimisation of permeability.

7 Appendix

7.1 In-Situ XRD Spectra

All of the data presented in this section was used to help interpret the Pd-Cu system in the main body of work.

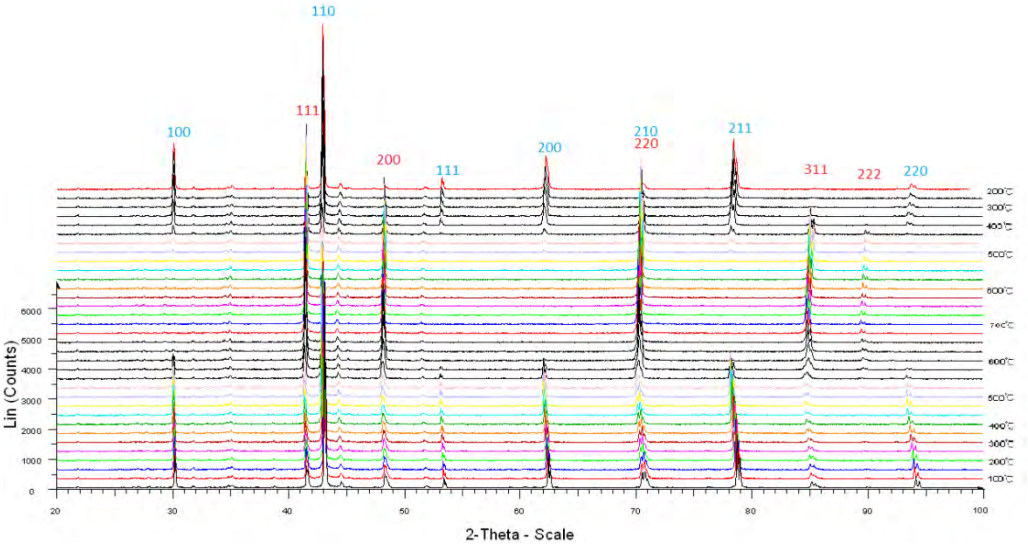

Figure 7.1 – XRD spectra of $Pd_{47.76}Cu_{52.24}$ heated from room temperature to 700°C and back, under an atmosphere of 1bar hydrogen.

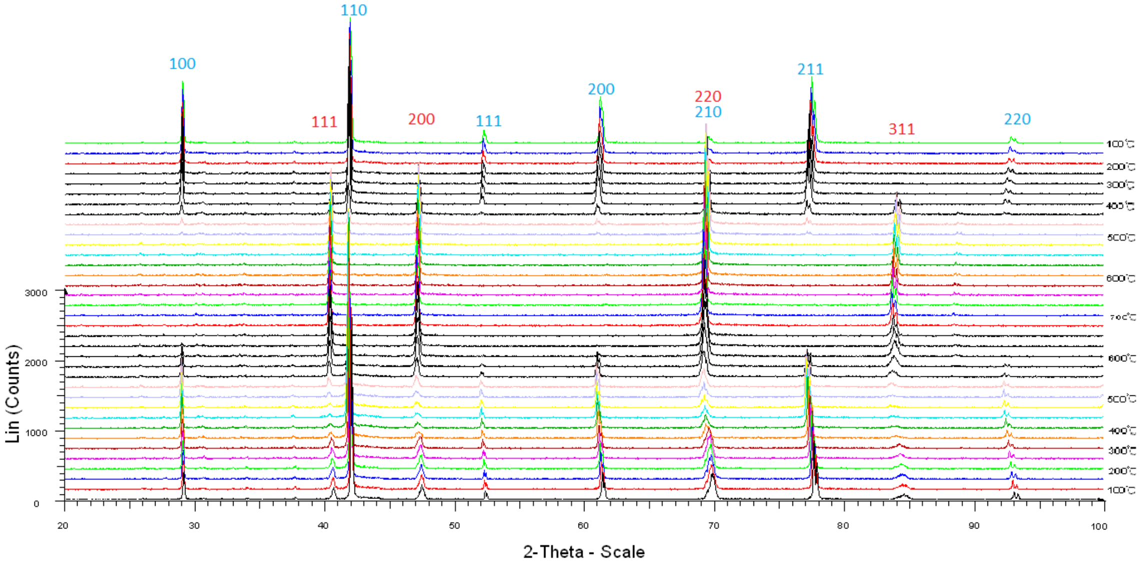

Figure 7.2 – XRD spectra of $Pd_{47.76}Cu_{52.24}$ heated from room temperature to 700°C and back, under an atmosphere of 5bar hydrogen.

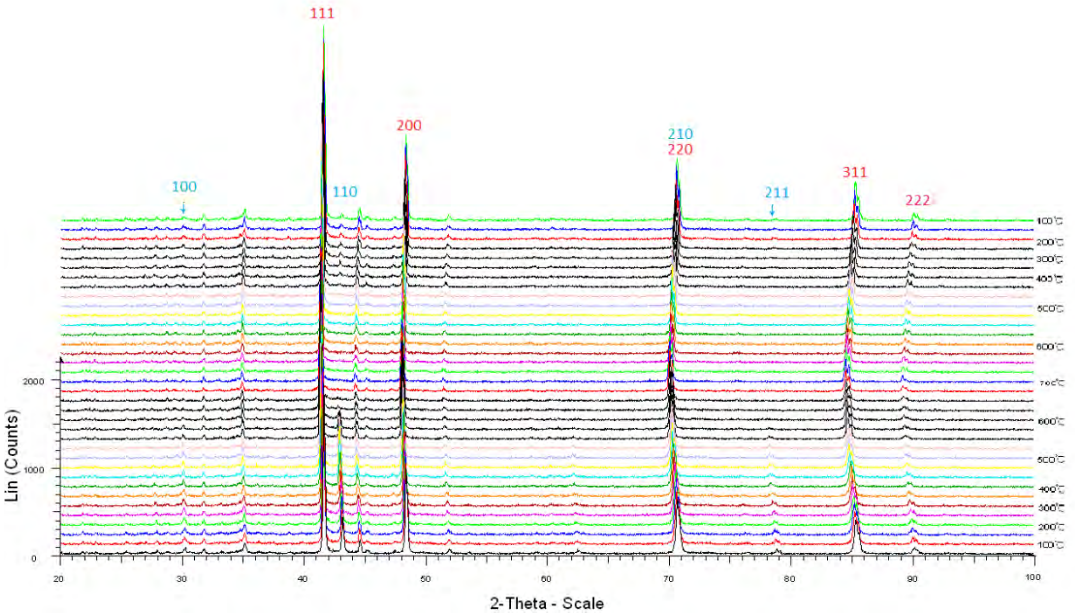

Figure 7.3 – XRD spectra of $Pd_{50.10}Cu_{49.90}$ heated from room temperature to 700°C and back, under an atmosphere of 1bar hydrogen.

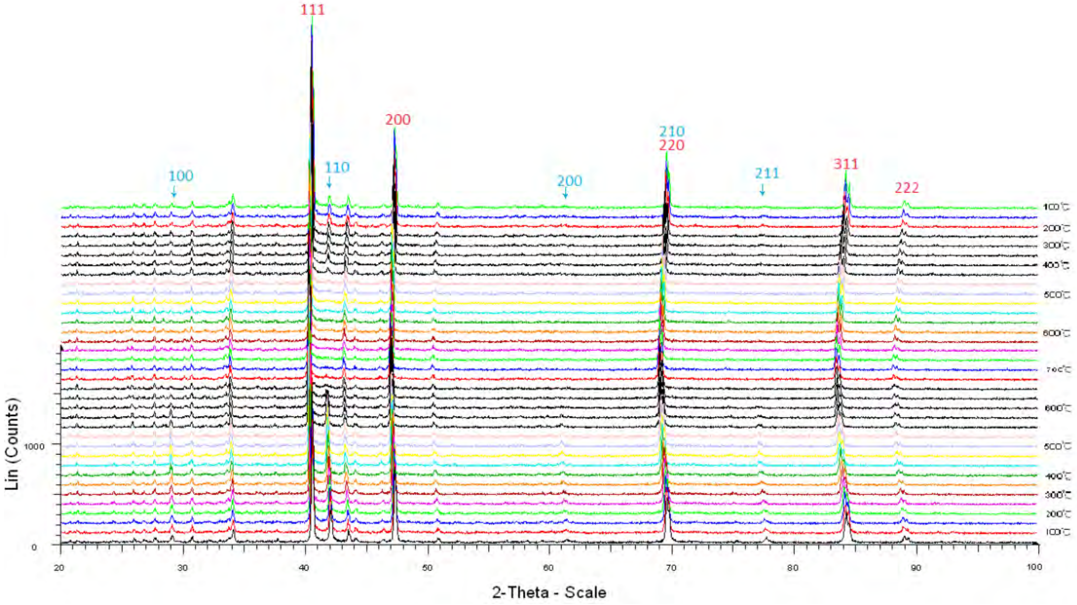

Figure 7.4 – XRD spectra of $Pd_{50.10}Cu_{49.90}$ heated from room temperature to 700°C and back, under an atmosphere of 5bar hydrogen.

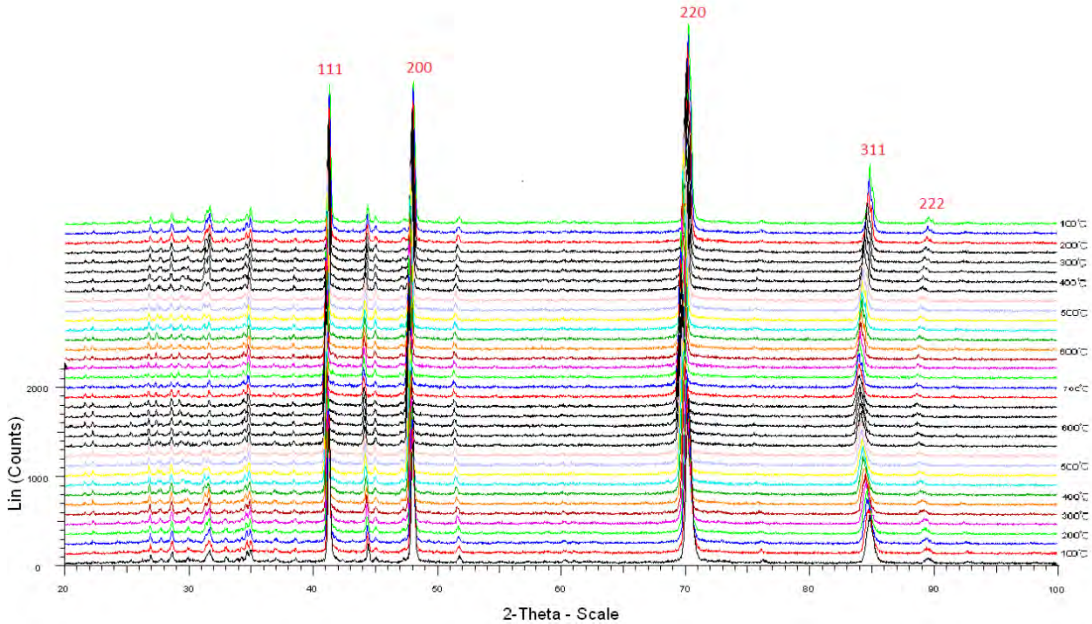

Figure 7.5 – XRD spectra of Pd$_{\sim56.5}$Cu$_{\sim43.5}$ heated from room temperature to 700°C and back, under an atmosphere of 1bar helium.

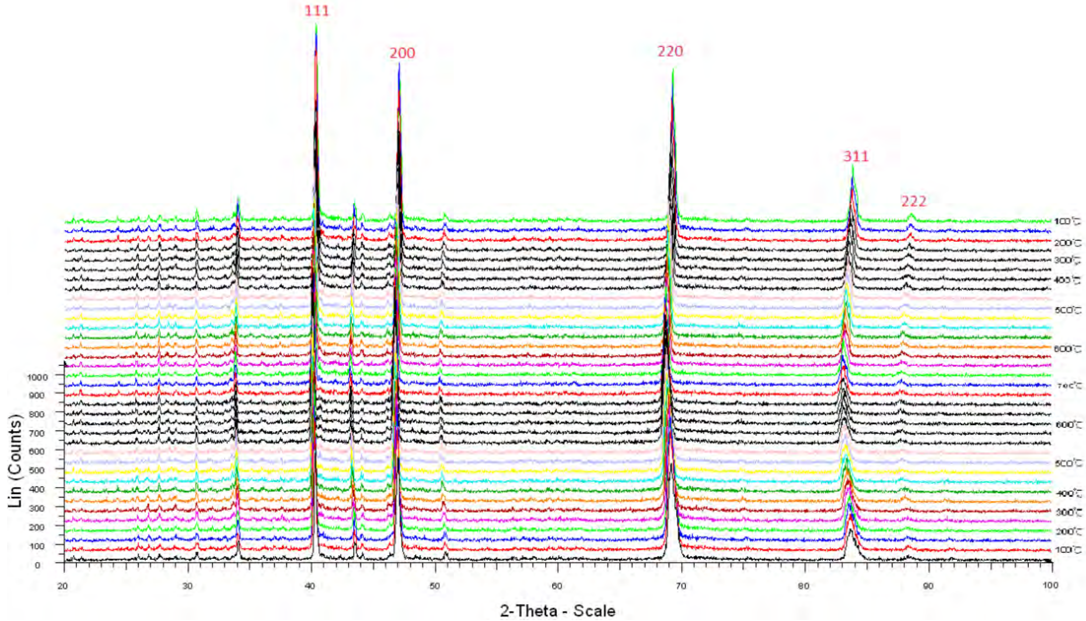

Figure 7.6 – XRD spectra of Pd$_{\sim56.5}$Cu$_{\sim43.5}$ heated from room temperature to 700°C and back, under an atmosphere of 1bar hydrogen.

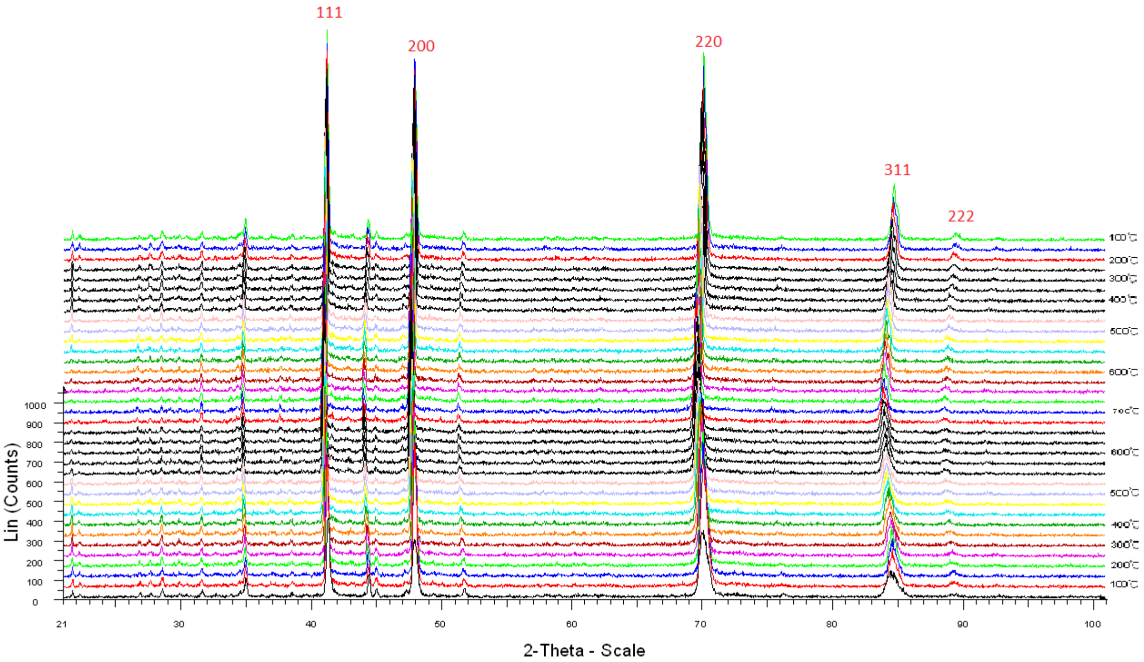

Figure 7.7 – XRD spectra of $Pd_{\sim 56.5}Cu_{\sim 43.5}$ heated from room temperature to 700°C and back, under an atmosphere of 5bar hydrogen.

7.2 DSC Results

DSC results were deemed too unreliable to be used to interpret the Pd-Cu phase diagram. In this section the reasons for not including the DSC data are summarised.

Initially a baseline was taken on an empty aluminium pan at heating to 590 ºC and cooling back to room temperature at 2ºC per minute, under both inert and hydrogenated conditions. Then comparative scans were carried out on Pd-Cu foils, $Pd_{50.10}Cu_{49.90}$ and $Pd_{47.76}Cu_{52.24}$, cut finely to fit in the pan. A graph showing the DSC results for $Pd_{50.10}Cu_{49.90}$, under both inert (Ar) and 3bar hydrogen, are shown, Figure 7.8.

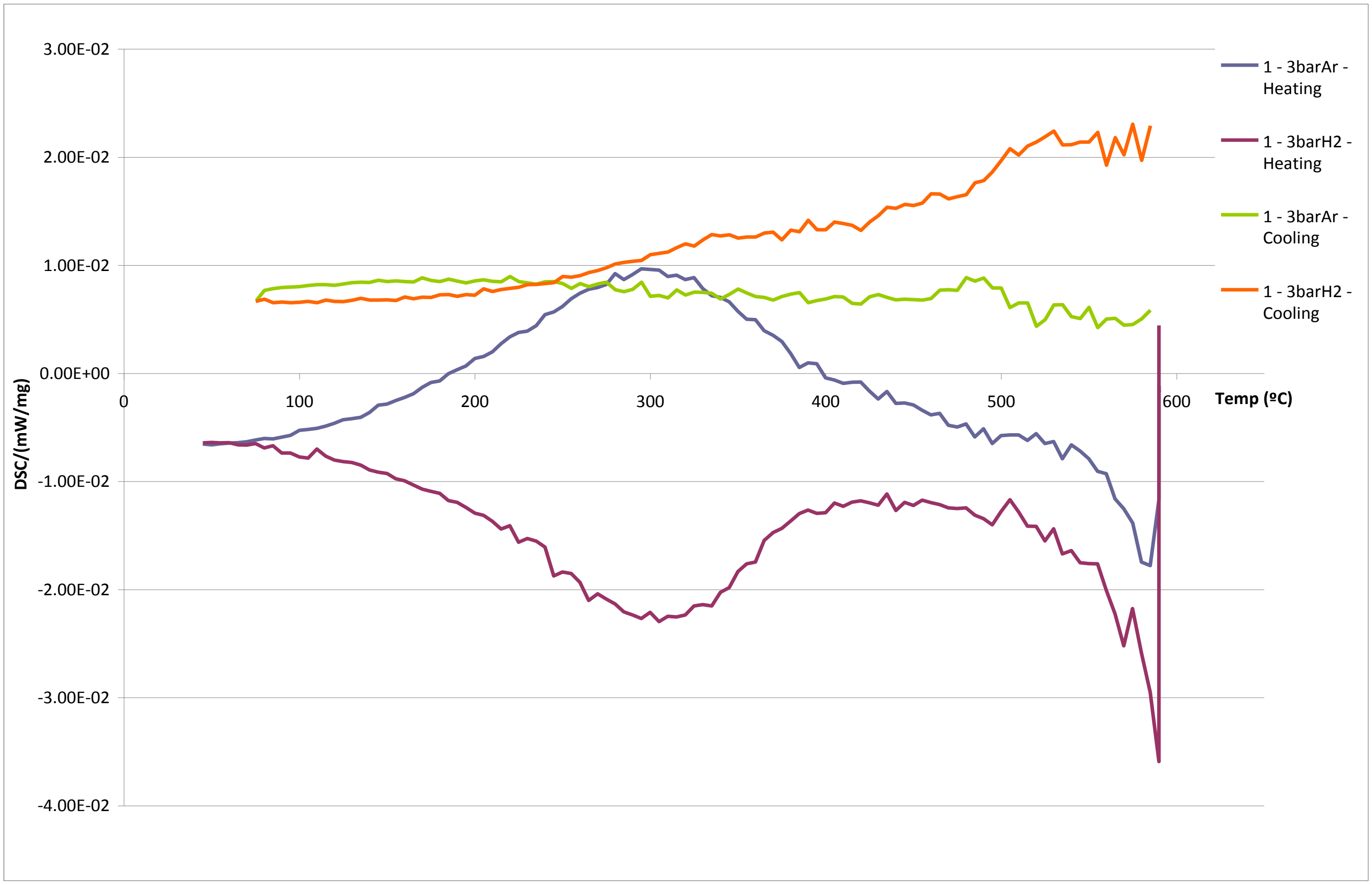

Figure 7.8 – DSC results for heating and cooling of $Pd_{50.10}Cu_{49.90}$ (batch 1) under both hydrogenated and inert atmospheric conditions.

The most interesting aspect of this graph is the different shape of the heating curves between atmospheres from 100 - 400 ºC. These curves appear to be the mirror image of one another moving in the exothermic direction under inert condition and endothermic when hydrogenated. At higher temperatures a different curve above 500 ºC is observed in the same direction for both atmospheric conditions, this may be related to the completion of a phase transformation to fully f.c.c. Cooling curves between atmospheres appear to show a similar shape. The source of this discrepancy in results was thought to be due to variations in the shape of the baseline. Baselines themselves for 3bar Ar and H_2 are plotted in Figure 7.9.

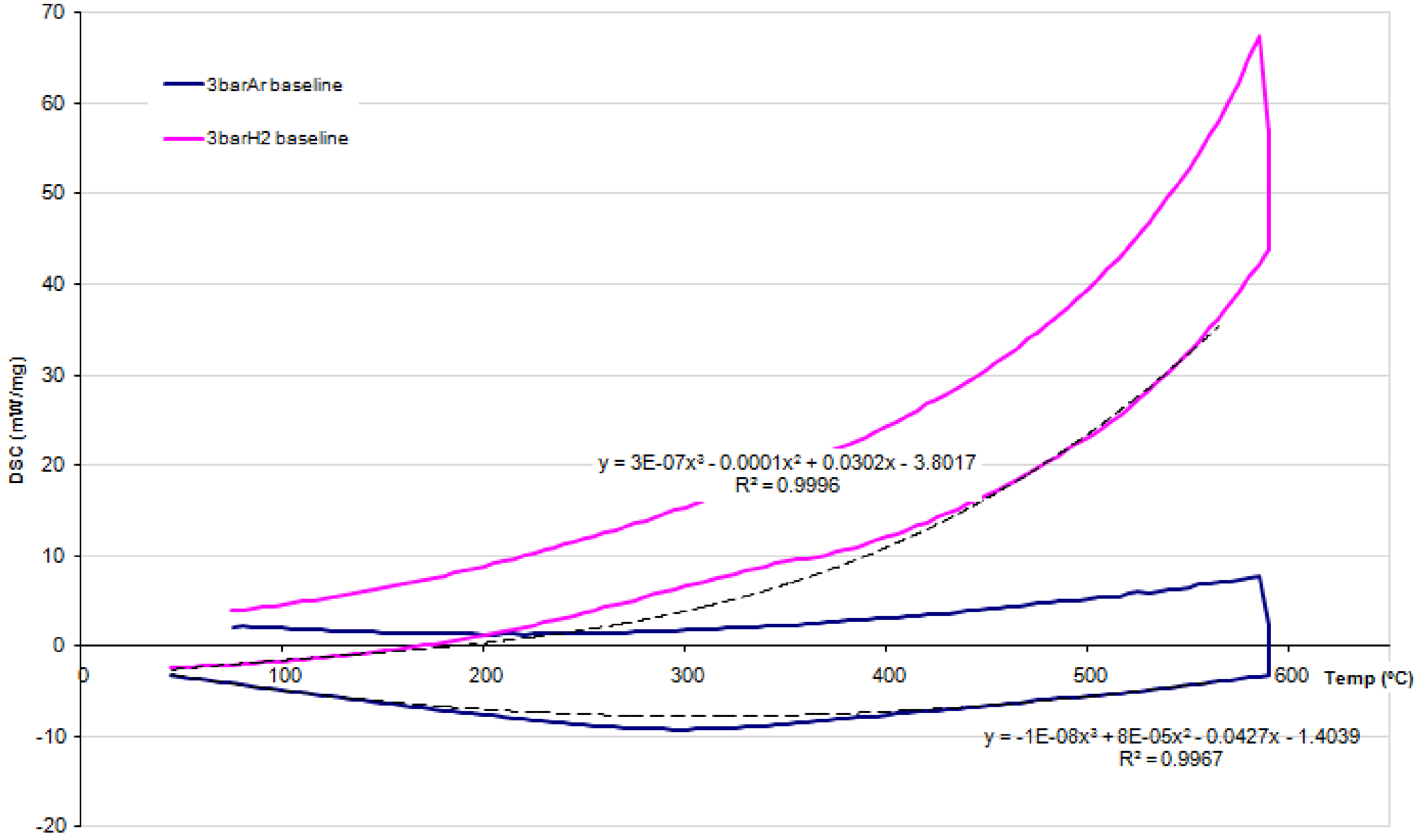

Figure 7.9 – Baselines of DSC scans for 3barH_2 and 3bar Ar atmospheres.

The heating cycle for these baselines curves show slight deviations from the rest of the data between ~150 ºC and ~450 ºC; this is highlighted by a dashed trend line which shows where the curve would be expected to be. As this region corresponds to the peaks shown upon heating in Figure 7.8 and are in the correct direction to be the cause of these erroneous results. New baseline experiments were carried out but showed similar shape.

Another factor which affects the reliability of results is the high values on the y axis for baseline experiments (Figure 7.9) in comparison to measurements on samples (Figure 7.8). This may stem from poor contact area of foils to the aluminium pan.

Although efforts were made to rectify the problems encountered in this technique unfortunately no reliable data could be obtained.

8 References

Ogden J, *Hydrogen Applications: Industrial uses and stationary power*, http://www.its.ucdavis.edu/education/classes/pathwaysclass/7-StationaryH2(Ogden).pdf Oct 2004.

Meyers, R.A., *Handbook of petroleum refining processes. Third edition.* 2004, New York: McGraw-Hill.

U.S. Department of Energy, *Hydrogen Posture Plan: An Integrated Research, Development, and Demonstration Plan*, www.hydrogen.energy.gov, February 2004, p. 8-11

Nenoff TM, Spontak RJ, *Membranes for hydrogen purification: An important step toward a hydrogen-based economy*, MRS Bulletin, Vol 31, Oct 2006, p.735-744

What are some uses of hydrogen? http://www.wisegeek.com/what-are-some-uses-of-hydrogen.htm

McGuiness PJ, Short C, Wilson AF, Harris IR, *The product ion and characterization of bonded, hot -pressed and die-upset HDDR magnets*, Journal of Alloys and Compounds, Vol. 184 , 1992, p.243-255

University of Cambridge, *Hydrogen as a fuel and a coolant*, http://www.msm.cam.ac.uk/ascg/materials/hydrogen.php

Power & Energy, *High Brightness LED Manufacturing Market*, http://www.powerandenergy.com/markets-led.html

Job R, Ulyashin AG, Fahrner RW et al, *Low Temperature Doping of Silicon by Hydrogen Plasma Treatments*, http://www.electrochem.org/dl/ma/202/pdfs/0605.PDF

Spear WE., *Hall effect and impurity conduction in substitutionally doped amorphous silicon*, Philosophical Magazine, Vol. 35, 1977

Peacock PW, Robertson J, *Behavior of hydrogen in high dielectric constant gate insulators*, Applied Physics Letters, Vol 83, Number 10, 2003, p. 2025-2027

Crawley G, *Proton Exchange Membrane (PEM) Fuel Cells*, Fuel Cell Today, http://www.fuelcelltoday.com/media/pdf/archive/Article_1084_PEM%20article.pdf, Mar 2006

SRNL, http://srnl.doe.gov/images/pem_fuel_cell.jpg

US DoE, *PEM fuel cells*, http://www1.eere.energy.gov/hydrogenandfuelcells/fuelcells/fc_types.html?m=1&

BOC, *Hydrogen the most common gas*, US DoE PEM fuel cells, http://www.boc.ebcnet.co.uk/hydrogen/properties/index.html

Design news, http://www.designnews.com/photo/71/71704-CA6572818_Y.jpg

US DoE, *Natural Gas Reforming*, http://www1.eere.energy.gov/hydrogenandfuelcells/production/natural_gas.html

Book D, *Lectures on Hydrogen Production*, Mar 2010

US DoE, *Coal Gasification*, http://www1.eere.energy.gov/hydrogenandfuelcells/production/coal_gasification.html

Fuel Cell Hydrogen Energy Association, *Hydrogen production from coal*, http://www.fchea.org/core/import/PDFs/factsheets/factSheet_productionCoal.pdf

S.S. Gas Labs Asia Pvt. Ltd, *Hydrogen Gas Plant*, http://www.hydrogengasplants.com/hydrogen-gas-plant.html

Züttel A, Remhof A, Borgschulte A and Friedrichs O, *Hydrogen: the future energy carrier*, Phil. Trans. R. Soc. A, July 2010, Vol. 368, no. 1923, p. 3329-3342

Hagg, MB and Quinn R, *Polymeric facilitated transport membranes for hydrogen purification.* MRS Bulletin, 2006. Vol. 31, p. 750.

Fletcher S, *Thick film palladium-yttrium membranes for hydrogen separation*, University of Birmingham, Nov 2009

Grashoff GJ, Pilkington CE, Corti CW, *The purification of hydrogen: A Review of the technology emphasising the current status of palladium membrane diffusion*, Platinum Metals Review, Vol. 27 (4), 1983, p. 157-169

US DoE, NETL, *Capital and operating cost of hydrogen production from coal gasification.* National Energy Technology Laboratory, US DoE, 2005.

Sholl DS, Ma YH, *Dense metal membranes for the production of high purity hydrogen*, MRS Bulletin, Vol. 31, Oct 2006, p. 770-773

Paglieri and Way, *Innovations in Palladium membrane research*, Separation and Purification methods, Vol. 31(1), 2002, p. 1-169

Graham T, *Absorption and separation of gases by colloid septa*, Philos. Trans. R. Soc, 1866, Vol. 156 (399), p. 426.

Jewell LL and Davies BH, *Review of absorption and adsorption in the Pd-H system.* Applied Catalysis A: General, 2006, 310, p 1

Wise MLH, Farr JPG, and Harris, IR, *X-Ray studies of the a/b miscibility gaps of some Pd solid solution hydrogen system*, Journal of Less Common Metals, 1975. Vol. 41, p. 115

Bruning H and Sieverts A, Z. Physik. Chem. (Leipzig), 1933, Vol. A-163, p. 432

Gillespie LJ and Downs WZ, 3. Am. Chem Soc, 1939, Vol. 62 ,p 2501

Gillespie LJ and Sieverts A, *Hydrogen in Metals*, Chicago University Press, 1948

Nanu DE and Bottger AJ, *Towards designing stable Pd-based membranes for hydrogen gas separatio*n: A statistical thermodynamics approach, Advanced functional materials, Vol. 18, 2008, p. 898-906

Hurlbert RC, Konecny JO, *Diffusion of hydrogen through palladium*, Journal of Chemical Physics, Vol. 34, 1961, p. 655

McKinley DL, *U.S. Patent* 3,439,474, 1969

Allard KD, Flanagan TB and Wicke E, J. Phys. Chem, Vol. 74, 1970 (2), p. 298

Topsoe HFA, *Dutch Patent* 7018485, 1971

Musket RG, *Effects of contamination on the interaction of hydrogen gas with palladium*: *A review*, Journal of the Less Common Metals, Vol. 45, 1976, p. 173-183

Gao H, Lin YS, Li Y, Zhang B, *Chemical Stability and Its Improvement of Palladium-Based Metallic Membranes*, Industrial and Engineering Chemistry Research, Vol. 43, 2004, p. 6920-6930

Amandusson H, Ekedahl LG, Daaetun H, *Hydrogen permeation through surface modified Pd and PdAg membranes*, Journal of Membrane Science, Vol. 193, 2001, p. 35-47

Kulprathipanja A, Alptekin GO, Falconer JL, Way JD, *Pd and Pd-Cu membranes: inhibition of* H_2 *permeation by* H_2S, Journal of Membrane Science, Vol. 254, 2005, p. 49-62

Kajiwara M, Uemiya S, Kojima T, *Stability and hydrogen permeation behavior of supported platinum membranes in presence of hydrogen sulphide*, International Journal of Hydrogen Energy, Vol. 24, 1999, p. 839-844

Yoshida H, Konishi S and Naruse Y, *Effects of impurities on hydrogen permeability through palladium alloy membranes at comparatively high pressures and temperatures*, Journal of the Less-Common Metals, Vol. 89, 1983, p. 429 - 436

Thoen PM, Roa F, Way JD, *High flux palladium-copper composite membranes for hydrogen separations*, Desalination, Vol. 193 (1-3). 2006, p.224-229

Rothenberger KS , Howard BH, Killmeyer RP, Ciaocco MV, Morreale BD, Enick RM, *Palladium-Copper Alloy Membrane Performance Under Continuous H_2S Exposure*

Ruer R. *The alloys of palladium with copper*. Anorg Z Chem, 1906, Vol. 51, p. 223–30.

Jones FW, Sykes C. *The transformations of the copperpalladium alloys*, J Inst Met, 1939, Vol. 65, p. 419–33.

Taylor R. *Transformations in the copper-palladium alloys,* J Inst Met, 1934, Vol. 54, p. 255–72.

Jaumot FE, Sawatzky A. *An isothermal anneal study of quenched and cold-worked copper-palladium alloys.* Acta Metallurgica, 1956, Vol. 4, p. 118–26.

Nemilov VA, Rudnitskii AA, Polyakova RS. *Alloys of palladium with copper*. Izv Sektora Platiny, 1949, Vol. 24, p. 26–34.

Subramanian PR and Laughlin DE. *Copper-palladium*, J Phase Equilibrium, 1991,Vol. 12, p. 231–243

Huang W, Opalka SM, Wang D, Flanagan TB, *Thermodynamic Modelling of Cu-Pd-H System*, CALPHAD, 2007, Vol. 31 p. 315–329

Li M, Du Z, Guo C, Li C. *A thermodynamic modelling of the Cu-Pd system*. CALPHAD, 2008, Vol.32(2), p.439–446.

Decaux, C; Ngameni, R; Solas, D, et al. *Time and frequency domain analysis of hydrogen permeation across PdCu metallic membranes for hydrogen purification,* International journal of hydrogen energy, 2010, Vol. 35, (10), p. 4883-4892

Volkl J, Alefeld G. In: Alefeld G, Volkl J, editors. *Hydrogen in metals*, Berlin: Springer Verlag Topics in applied physics, Vol. 28, 1978, p. 321–348.

Piper J. *Diffusion of hydrogen in copper-palladium alloys*. J Applied Phys. 1966, Vol. 37, p. 715–721.

Goldbach A, Yuan L, Xu H, *Impact of fcc/bcc phase transition on the homogeneity and behaviours of PdCu membranes*, Separation and Purification Technology, 2010, Vol 73 (1), p.65-70

Howard BH, Killmeyer RP, Rothenberger KS, Cugini AV, Morreale BD, Enick RM, Bustamante F. *Hydrogen permeance of palladium–copper alloy membranes over a wide range of temperatures and pressures*, J MembraneSci, 2004 Vol. 241, p. 207–18.

Yuan L, Goldbach A, Xu H. *Segregation and H transport rate control in body-centred cubic Pd-Cu membranes*. J Phys Chem B, 2007, Vol. 111 (37), p.10952–10958.

Fletcher S, *Private Communication*, The University of Birmingham, 2009-2010

Denton AR, Ashcroft AW, *Vegard's Law*, Physical Review A (Atomic, Molecular, and Optical Physics), 1991, Vol. 43, (6), Mar 1991, p.3161-3164

Zhang XL, Xiong GX and Yang WS, *Hydrogen separation from the mixtures in a thin Pd-Cu alloy membrane reactor*, Natural Gas Conversion VIIIm Proceedings of the 8th Natural Gas Conversion symposium, 2007, Vol. 167, p.219-224

Tong, JH, Shirai R, Kashima Y, et al, *Preparation of a pinhole-free Pd-Ag membrane on a porous metal support for pure hydrogen separation*, Journal of Membrane Science , 2005, Vol. 260, (1-2), p. 84-89,